QUANTITATIVE ULTRASOUND AND THE EFFECTS OF ACOUSTIC NONLINEARITY

BY

ANDRES LEONEL COILA PACOMPIA

DISSERTATION

Submitted in partial fulfillment of the requirements
for the degree of Doctor of Philosophy in Electrical and Computer Engineering
in the Graduate College of the
University of Illinois Urbana-Champaign, 2022

Urbana, Illinois

Doctoral Committee:

Professor Michael L. Oelze, Chair and Director of Research
Professor Jont B. Allen
Assistant Professor Pengfei Song
Professor Roberto Janniel Lavarello Montero, Pontificia Universidad Católica del Perú

ABSTRACT

Diagnostic ultrasound is the most heavily utilized imaging modality in medicine worldwide second only to digital X-ray. Conventional B-mode imaging relies on small impedance differences (often <5%) between tissues to provide image contrast. This perceived contrast is further reduced because B-mode images are replete with speckle. The development of novel imaging techniques using ultrasound signals that have different sources of image contrast and may not be affected by speckle is medically significant; for example those based on mapping quantitative ultrasound (QUS) parameters. However, different types of tissues or tissues under different disease states are known to have different coefficients of nonlinearity (B/A). For example, fatty tissues have a B/A of 11, liver has a B/A of 6.6, and water has a B/A of 5. At low pressures it can be assumed that QUS parameters are not changed by acoustic nonlinear distortion, whereas at higher pressures the nonlinear distortion transfers energy from the fundamental frequency of the ultrasound wave into higher harmonics. These distortions can affect the bias and variance of spectral-based QUS estimates, such as the backscatter coefficient and attenuation coefficient. In the first part of this dissertation, we aim to determine conditions that can decrease acoustic nonlinear effects. We explored an *in situ* calibration approach which would minimize nonlinear distortion on QUS estimates. In the second part of this dissertation we present two methods to calculate the B/A based on observations related to QUS estimation. The first method was an heuristic approach based on estimating the excess attenuation coefficient and required two well-characterized reference phantoms. The second method for B/A estimation needed only one reference phantom and was performed mainly in the time-domain using the conservation of energy principle. Using the later method we can construct parametric images to map the cumulative average B/A versus depth.

To my parents, Andres and Mercedes, my sisters, Nury, Gladys, Elva, Flor, and my wife, Boom, for their endless love.

Acknowledgments

First of all, I would like to express my respect to Dr. Michael Oelze for inviting me to the Bioacoustics Research Laboratory where I found brilliant researchers and lab mates throughout my graduate student years. Dr. Oelze's continuous support allowed me to conduct this research and I acknowledge him as my role model in academia (and life). My thanks to the contributions of my committee members—Dr. Jont Allen, Dr. Roberto Lavarello, and Dr. Pengfei Song—for their insightful comments and helpful opinions at different stages of my research, and for also being open to discuss any questions I had regarding my future plans.

My gratitude also goes to my lab mates in the "Oelze Group": Trong, Anil, Tony, Gun, Miles, Jenna, Kou, Yuning, Mick, and Ufuk, and Dr. Rita Miller for always being ready to help. In particular, I would like to thank Jenna Cario for proofreading my dissertation, and Dr. Rita Miller, Jenna, and Yuning for her assistance regarding animal handling. I hope our professional and academic paths keep us intertwined in the future.

I would like to thank my family as well—my exemplary parents, Andres and Mercedes, and my dear sisters, Nury, Gladys, Elva and Flor—for being delighted by every step of my career. I specially want to thank my wife, Boom, for her constant support, for making the last few years of my graduate studies as delightful as they can get, and for always helping me to keep sight on the important aspects of life.

Lastly, I want also to acknowledge the Peruvian Government funding sources whose support made it possible to complete the dissertation: the Consejo Nacional de Ciencia, Tecnología e Innovación (Concytec), the Fondo Nacional de Desarrollo Científico, Tecnológico y de Innovación Tecnológica (Fondecyt), and the Programa Nacional de Investigación Científica y Estudios Avanzados (Prociencia) through grant 132-2016.

TABLE OF CONTENTS

LIST OF ABBREVIATIONS

ACS	Attenuation coefficient slope
B/A	Nonlinearity parameter
BSC	Backscatter coefficient
ESD	Effective scatterer diameter
MI	Mechanical index
QUS	Quantitative ultrasound
RF	Radiofrequency
RMSE	Root mean square error
ROI	Region of interest
SLD	Spectral log difference
SNR	Signal-to-noise ratio

CHAPTER 1

INTRODUCTION

1.1 Nonlinearity parameter B/A

In a fluid nonlinear medium, the degree of nonlinearity is typically characterized by its nonlinearity parameter B/A [1, Chapter 2], where A and B are the 1st and 2nd order terms in the isentropic power series expansion of the total pressure P (equilibrium pressure P_0 plus acoustic pressure p) as function of density ρ (understood in the spatio-temporal domain), namely, the adiabatic equation of state

$$P(\rho) = P_0 + \frac{\partial P}{\partial \rho}\bigg|_{\rho=\rho_0} (\rho - \rho_0) + \frac{\partial^2 P}{\partial \rho^2}\bigg|_{\rho=\rho_0} (\rho - \rho_0)^2 + \cdots , \qquad (1.1)$$

where ρ_0 is the equilibrium density, $A \equiv \frac{\partial P}{\partial \rho}\big|_{\rho=\rho_0}$ and $B \equiv \frac{\partial^2 P}{\partial \rho^2}\big|_{\rho=\rho_0}$. Whereas truncation of the Eq. (1.1) up to the 1st order is required to produce the linear acoustic wave equation, truncation up to the 2nd order term can later be combined with the equation of momentum and equation of continuity of fluids (also truncated up to the 2nd order) to obtain nonlinear expressions for the acoustic pressure of a propagating monochromatic plane wave [2, Chapter 11].

An important result of acoustic nonlinearity is that the local sound speed during compression ($c_{\mathrm{C}} = c_0 + \beta u$) is faster than the local sound speed during rarefaction ($c_{\mathrm{R}} = c_0 - \beta u$), where c_0 is the small-signal speed of sound, u is the particle velocity amplitude, and $\beta = 1 + \frac{B}{2A}$ is defined as the nonlinearity coefficient. This asymmetry leads to a cumulative distortion of the acoustic wave until the slope of waveform becomes infinity, theoretically. The distance at which this "shock" occurs is named the shock distance. In the frequency domain, the aforementioned nonlinear distortion of the propagating wave results in generation of the 2nd, 3rd, and higher order harmonics.

These harmonics require that energy be transferred out of the fundamental frequency. Moreover, other effects such as saturation can be observed under certain circumstances.

1.2 Quantitative ultrasound

Current diagnostic ultrasound is limited in its capabilities because imaging is based on the contrast in tissue acoustic impedance, which only varies by about 5% [3, Chapter 4]. Furthermore, speckle in conventional B-mode images results in reduced ability to visualize contrast. Therefore, speckle-free imaging modalities with higher contrast, e.g., MRI, X-ray CT, PET, are preferred for many diagnostic imaging tasks. However, these imaging modalities are expensive (i.e., they have low accessibility to under-resourced communities), not portable, and X-ray and PET introduce ionizing radiation. Quantitative ultrasound (QUS) is a branch in the ultrasound field that attempts to provide a set of quantitative parameters that can be used to complement the characterization of materials given by traditional ultrasound by creating speckle-free images with new sources of image contrast [4]. In the last two decades, several efforts have focused on estimating QUS parameters of soft tissues *in vivo*, such as the backscatter coefficient (BSC), attenuation coefficient (AC), speed of sound, and viscoelasticity, among other QUS parameters. In the first part of this dissertation we focus on the AC and BSC that can be estimated using relatively simple methods in the frequency domain.

1.2.1 AC and BSC for tissue characterization

The attenuation refers to losses such as absorption or scattering as ultrasound propagates in a medium [3, Chapter 4]. The attenuation is an acoustical property of tissues and has been used as a quantitative ultrasonic parameter for tissue characterization, including recent studies in soft tissues such as liver [5], breast [6], placenta [7], and indirectly in muscle [8], among other biological tissues. Empirical results from studies have found that the attenuation coefficient, $\alpha(f)$, for several soft tissues follows a power-law dependence vs frequency f, i.e., $\alpha(f) = \alpha_0 f^{\gamma}$, where α_0 is an attenuation coefficient fac-

tor and γ is the frequency dependent exponent, commonly $\gamma \in (1, 2)$ [9, p. 74]. Hence, current methods for estimating AC are performed mainly in the frequency domain.

The BSC describes internal scattering structures in a medium [10, Chapter 9]. Recently, the BSC has been used to characterize bone [11], liver [12], breast [13], and pancreas [14], among other *in vivo* studies. The BSC is calculated from estimates of the power spectra of the backscattered signals from a medium. However, the BSC must be calibrated to account for diffraction and system effects and compensated for frequency-dependent attenuation. Whereas the attenuation coefficient can be experimentally estimated and the diffraction can be analytically approximated for simple transducer geometries; the effects of system settings cannot be exactly modeled. In order to compensate for the system effects, a couple of methods have been applied, i.e., the planar reflector method [15, 16] and the reference phantom method [17]. In the planar reflector method, additional signals are acquired from the reflection off of a smooth plate with known reflectivity around the transducer focal region. In the reference phantom method, calibration signals are acquired from a well-characterized reference phantom, i.e., a phantom with known BSC and attenuation coefficient.

1.2.2 QUS biases because of acoustic nonlinear effects

In spectral-based methods to estimate the BSC or the AC, acoustic propagation models are typically assumed to be linear despite the very well known nonlinear nature of all media for acoustic propagation. In particular, the nonlinearity parameter, B/A (to be read as "B over A"), is used to characterize the nonlinearity of a medium, including biological tissues [18]. In practical terms, the nonlinear distortion manifests through the generation of harmonics, i.e., the energy in the ultrasonic fundamental frequency band is transferred to higher bands (harmonics). This transferring of energy effectively produces a distortion of the fundamental band from the backscattered echoes used in the estimation of the BSC and AC, thus, theoretically it introduces biases in the QUS estimates.

Particularly, potential bias in QUS estimates involving soft tissues have been noted in early studies. For example, in Carstensen et al. [19] the ab-

sorption coefficient (i.e., an important component of attenuation) measured through heat production showed an increment of 100% in absorption coefficient from bovine liver samples when the power source incremented 10 dB. Similarly, in work from Goss and Fry [20], a 7 dB increment of an SPTP (spatial peak temporal peak) intensity increased the estimated absorption coefficients of various soft tissues of a rat *in vivo* between 70% to 210%.

More recent studies using present spectral-based techniques have also found biases in nonlinear regime. Nonlinear distortion in the through transmission substitution technique (not suitable *in vivo*) was evaluated by Zeqiri et al. [21] and found underestimated values of AC between 30%-40% in liver samples when the propagation between source and receiver went from half the shock distance to double the shock distance. However, experiments in pulse-echo mode by D'hooge et al. [22] showed an overestimation of the liver AC *in vivo* as the transmit ultrasonic power increased. In that study, the log spectral difference found an increment of AC in liver from 0.57 dB/cm/MHz to 0.69 dB/cm/MHz (i.e., about 21%). The basic difference between through transmission and pulse-echo cases, was that the calibration signal in the first case (across the water path) distorted more than the sample signal; whereas the "calibration signal" in the spectral log difference in [22] came from a location within the liver closer to the source, i.e., distorted less, than the the sample signal that came from a deeper region within the liver.

Hence, in the first part of this dissertation, our goal is to understand the effects of nonlinear distortion by the intrinsic nonlinear nature of a medium on the bias and variance of the other spectral-based parameter, the BSC, in pulse-echo estimation methods and to determine under which conditions the nonlinear effects can be decreased or minimized. Regarding the AC, we also expanded findings of the work from D'hooge et al. [22] on AC estimation in pulse-echo by including cases where diffraction effects are non-negligible, i.e., using moderately focused sources calibrated by well-characterized reference phantoms.

1.2.3 B/A for tissue characterization

When using ultrasound for imaging tasks, such as medical diagnostics, it cannot be assumed that these nonlinear phenomena will be absent. Because

backscattering from soft tissues is small compared to the incident field, in order to improve the signal-to-noise (SNR) ratio for specific imaging tasks, larger input pressure levels (energy levels, excitation levels, power levels, etc.) are often used during data acquisition resulting in a higher likelihood of nonlinear distortion of the ultrasonic waves. In the previous section, we stated that biases in the QUS parameters are likely to occur in nonlinear regime and care would be needed to minimize nonlinear effects. Hence, tissue characterization using estimates of B/A itself opens an alternative parameter for characterizing tissue, a new source of image contrast and could potentially be used to account for biases in other QUS estimates.

Recently, QUS parameter estimates based on the BSC and AC have shown better predictive capabilities for grading of hepatic steatosis than conventional ultrasound imaging [23]. Steatosis is an advanced stage of the non-alcoholic fatty liver disease (NAFLD) that affects millions of people worldwide [24]. Because fatty tissues are highly nonlinear compared to parenchymal tissues [25, 26], *in vivo* estimation of the B/A could address the early diagnosis of NAFLD. In a similar approach, the B/A could be used to assess the non-dense tissue in breast, which could be a tool in early diagnosis of breast cancer [27]. Therefore, estimation of B/A has the potential to improve diagnosis of multiple disease states.

1.2.4 B/A estimation in pulse-echo

Several techniques exist for estimation of B/A including: thermodynamic methods, aqueous solutions and finite amplitude methods [28, 29]. However, tissue characterization *in vivo* with clinically-available probes in the common diagnostic ultrasound frequency range (1–10 MHz) would generally require a pulse-echo approach. Currently, there are no widely accepted methods for estimating the nonlinearity parameter of tissues using ultrasound with a pulse-echo system, despite the potential contrast advantages offered. In one group of techniques to map B/A, it is estimated from the received signals in the second harmonic and the fundamental band of the wave [30, 31]. In order to estimate the second harmonic energy, Gong et al. [30] devised a theoretical approach and experimentally required two transducers that operated at different bandwidths (one for recording the 2nd harmonic signals),

e.g., dual piezoelectric. In some applications such as ultrasonic harmonic imaging, the fundamental and 2nd harmonic frequencies might be acquired by a single wide band transducer. For such transducers the bandwidth of the source could be divided into smaller sub-bands in reception to capture the second harmonic (van Sloun et al. [31]) as in harmonic imaging. In this approach, however, the spatial resolution is deteriorated because the bandwidth is partitioned resulting in a longer pulse length of the fundamental.

Another approach is the pulse-echo pump wave method. Cain [32] used a low-frequency continuous pump wave and a high-frequency probe (the center frequency was large by an order of magnitude). The interaction of both produces a change of phase in the pump wave that can be related to the B/A of the propagating media. A modern version of the pump wave approach is presented by Kvam et al. [33], but the requirement of *ad hoc* transducers could limit rapid translation to clinical settings.

A third group of pulse-echo B/A estimation approaches are based on the envelope distortion of a pulse at the fundamental band when several energy levels are utilized. Fatemi and Greenleaf [34] observed that the attenuation of ultrasound increased with the acoustic pressure level in pulse-echo experiments. Their setup used calibrated signal from wire targets embedded in the medium assessed (similar to the pulse-echo method use by Liu and Nikoonahad [35] to estimate B/A of liquids) and a theoretical model to predict the change in the envelope of a broadband pulse. The change was observed by mapping out the pressure magnitude of a beam over the depth of focus versus different excitation levels. In addition, the apparent attenuation increased versus pressure level, i.e., it was the highest near the focus of the beam. The apparent excess attenuation occurs because more energy in the ultrasound wave is transferred from the fundamental to the higher harmonics and this effect increases with increasing pressure. Because the transducer used for imaging is band limited to the fundamental, on receive the energy that was transferred to the higher harmonics is not recorded and this results in an apparent excess attenuation of the fundamental bandwidth signal. Calibration signals from nylon wire targets located within predefined depths were required to provide calibrated backscattered signals. Fatemi and Greenleaf [34] were able to construct qualitative B/A images characterized by shadowing following a strong nonlinear region (similar to the effect of region of strong attenuation). Another limitation of the method is the need for strong

echoes from wire targets embedded in the assessed material. The need for embedded wire targets limits potential implementation *in vivo*.

Another hurdle for developing imaging of nonlinearity *in vivo* is that the accumulation of energy in the second harmonic occurs more rapidly near the focus of the source and is not uniform throughout an image region due to the acoustic beam diffraction. This results in a decreased ability to image outside of the focal region of a source. Because the second harmonic energy accumulates with propagation depth, the change in the second harmonic energy with depth must be accurately mapped.

For the second part of this dissertation, two novel B/A estimation approaches are presented. First, because phenomenon like excess attenuation (increasing of AC in the nonlinear regime) occurs due to nonlinear distortion, we aim to use such distortion on spectral-based AC estimates to reveal important information about the B/A of the interrogated media. This is an heuristic approach that was tested in simulations only.

For a second approach, a time-domain estimation technique utilizing conservation of energy is used to map B/A. A time-based approach is used because a spectral-based approach would have the limited spatial resolution common to parametric images made from spectral-based BSC estimates. In this second B/A estimation approach we will, in a sense, combine methods that use the 2nd harmonic measurements like [30], but instead of using a dual transducer, the energy transferred to the second harmonic is estimated from the energy in the fundamental at two excitation levels. The instantaneous second harmonic energy is estimated versus depth and calculated implicitly using two acquisitions performed at two source power levels (low quasi-linear and high nonlinear). The change in the amplitudes of the envelopes will provide information about the energy transferred to the second harmonic (like the work in [34]). The method will require a reference phantom with known acoustic parameters, including B/A, to generate a numerical B/A map.

The development of a B/A imaging mode will complement diagnostic capabilities of medical ultrasound but also will have notable advantages over conventional ultrasound imaging. Namely, the range of contrast between tissues will be much greater for imaging of the acoustic nonlinearity parameter for tissues compared to acoustic impedance. Second, the acoustic nonlinear coefficient images will not suffer from speckle artifacts, which are inherent in conventional B-mode images.

1.3 Objectives

The goal of the proposed dissertation is twofold. In the first part, we aim to predict the degrees of distortion that can be observed in BSC and AC estimates by using different levels of acoustic pressures while still below FDA (Food and Drug Administration) safety limits set for the Mechanical Index (MI). We aim to assess how acoustic nonlinearity affects two prevalent QUS parameters, i.e., the BSC and the AC. Also, correcting for potential nonlinear distortion on the BSC using a calibration *in situ* will be assessed.

For the second part, we will present novel B/A estimation techniques. The first technique will be based on measurements of the excess attenuation coefficient computed in a quasi-linear scenario vs propagation in the nonlinear regime. The second technique will be a time-domain method that can map the B/A versus depth based on conservation of energy principle and an implicit calculations of the 2nd harmonic. The time-domain B/A estimation methods will be tested in numerical simulations, *ex vivo* and *in vivo*.

This present dissertation follows this structure: in Chapter 2, we quantify the influence of acoustic nonlinearities on the estimation of the BSC. In Chapter 3, we will quantify the effects of acoustic nonlinearities on the estimation of the AC. In Chapter 4, we present an *in situ* calibration approach to minimize nonlinear distortion for BSC estimation. In Chapter 5, we suggest a guide to convert information of the excess attenuation into the nonlinearity parameter for estimating B/A for a homogeneous material. In Chapter 6, we construct two-dimensional B/A maps for different degrees of acoustic pressures. Finally, we present the conclusions in Chapter 7 along with potential future directions of this work.

CHAPTER 2

EFFECTS OF ACOUSTIC NONLINEARITIES ON THE BACKSCATTER COEFFICIENT

2.1 Introduction

When estimating the BSC, it is common to assume linear acoustic propagation. However, all media are nonlinear in terms of acoustic propagation. Therefore, if the excitation signal produces acoustic waves with finite amplitude, i.e., not small acoustic pressures, the waveform might undergo harmonic generation, which is not predicted by linear acoustic theory. This nonlinear distortion is a function of the nonlinearity parameter B/A of the medium, derived from the pressure-density equation of state for fluids [2]. Furthermore, another parameter that contributes indirectly to nonlinear distortion of ultrasonic waves is the attenuation coefficient of the medium. For example, in a high attenuating medium, the acoustic pressures will decrease over a shorter distance than for a low attenuating medium with higher frequencies attenuating at a higher rate than lower frequencies. Hence, for a medium with the same B/A but a higher attenuation, less nonlinear distortion will be observed. On the other hand, in a low attenuating medium, excitation signals with larger amplitudes are more likely to undergo nonlinear distortion. In the particular case of plane waves, the ratio of the nonlinearity coefficient $\beta = 1 + \frac{B}{2A}$ and the attenuation coefficient, are used for the the calculation of the Gol'dberg number, Γ, which predicts the occurrence of significant nonlinear distortion ($\Gamma \gg 1$) or its absence ($\Gamma \ll 1$) [36].

Distilled water has a nonlinearity parameter B/A=5 (at 20 °C) [18], which is lower than most tissues [37]. On the other hand, water has a low attenuation coefficient for frequencies used in clinical sonography scanners (1–10 MHz) compared to soft tissues. For example, at 5 MHz, the attenuation coefficient of water is 0.055 dB/cm [9], whereas in soft tissue, the attenuation at 5 MHz can be higher than 5 dB/cm. Therefore, any estimation

technique, such as the estimation of the BSC, that uses a water path might produce unwanted nonlinear distortion of the estimate. One accepted calibration method for BSC estimation is the planar reflector technique. The system signal is calibrated by reflecting a pulse from a smooth planar reflector of known reflectivity. Therefore, we hypothesize that when using the planar reflector method in water, water might be an undesired source of nonlinear distortions of the reflected signals. This nonlinear distortion in the calibration signal can distort the final BSC estimate. On the other hand, when using the reference phantom method, the attenuation of the phantom can be constructed such that it is closer to the attenuation of tissue. Hence, the potential is for the nonlinear distortion in the calibration signal from the reference phantom to be less than that from a planar reflector in water.

In previous works on BSC estimation, it has been assumed that nonlinear distortion is negligible. Although assuming linear behavior in acoustic wave propagation simplifies the analysis, there are instances where high pressure amplitudes are needed, for example, when internal tissue structures are insonified with high pressures to increase the signal-to-noise ratio (SNR). The goal of the study described in this chapter is to assess the BSC estimation from two calibration methods, i.e., the planar reflector method and reference phantom method, when higher ultrasonic pressures are used in the acquisition of RF data and how nonlinear distortion can affect the estimates of BSC.

2.2 Methods

Two BSC estimation methods are described in this section. The acoustic properties and data acquisition from physical phantoms, and the metrics used for validation of the hypothesis are detailed.

2.2.1 BSC estimation methods

Two widely used BSC estimation strategies were assessed: the planar reflector method and the reference phantom method. The first method exploits the simple geometry of the transducer to analytically compute the diffractive effects. The second method can be used with more complex transducer

geometries but can increase the variance of estimates without sufficient ensemble averaging of the reference spectrum.

Planar reflector method

The planar reflector method has been used with transducers having simple geometry, e.g., spherical focused transducers, because the effects of diffraction can be computed analytically and incorporated into the BSC calculation [15]. In our experiments, a spherically focused single-element transducer was used for BSC estimation. Gated scan lines of RF data from an interrogated medium corresponding to an axial length Δz and centered at the focal distance F, i.e., between $\langle F - 0.5\Delta z, F + 0.5\Delta z \rangle$, were recorded. The BSC, denoted by $\sigma(f)$, was computed from this data using Eq. (5) in [16]

$$\begin{aligned} \sigma(f) &= 2.17 D(G_p) \frac{\gamma^2 F^2}{\pi R^2 \Delta z} \frac{S(f,F)}{S_{\mathrm{w}}(f,F)} A(f,F), \\ D(G_p) &= |\exp(-iGp)[J_o(G_p) + iJ_1(G_p)] - 1|^2, \end{aligned} \tag{2.1}$$

where $S(f,F)$ is the power spectrum averaged over several gated scan lines estimated from a data block, $S_{\mathrm{w}}(f,F)$ is the average power spectrum of reflected echoes from a planar reflector located at depths between $\langle F - 0.5\Delta z, F + 0.5\Delta z \rangle$, $A(f,F)$ compensates for the attenuating effects of unknown medium and water, R is the transducer radius, γ is the reflectivity coefficient of the planar reflector, $G_p = (kR^2)/(2F)$ is the focal gain and J_ν is the Bessel function of the first kind and order ν. In (2.1), the system effects are assumed to be cancelled in the ratio of the spectra $S(f,F)/S_{\mathrm{w}}(f,F)$.

Reference phantom method

The system effects can also be compensated using a reference phantom method. Assuming equivalent sound speed in both sample and reference phantom, the diffractive effects are compensated through measurements as opposed to theory. The reference phantom needs to be previously well characterized, i.e., its acoustic parameters such as sound speed, BSC and atten-

uation coefficient are known. The BSC from the sample is estimated as [17]

$$\sigma(f) = \sigma_{\text{ref}}(f)\frac{S(f,F)}{S_{\text{ref}}(f,F)}\frac{A_{\text{ref}}(f,F)}{A(f,F)}, \tag{2.2}$$

where $S(f,F)$ and $S_{\text{ref}}(f,F)$ are the averaged power spectra from data blocks located at the same depth in the sample and the reference phantom, respectively, $A(f)$ and $A_{\text{ref}}(f,F)$ are the attenuation compensation functions for the sample and reference phantom, respectively, and $\sigma_{\text{ref}}(f)$ is the known BSC of the reference phantom. An advantage of the reference phantom method is that the processed echoes need not arrive from the focal region, although, in our work data were acquired in the focal region of the transducer. In (2.2), the system effects are assumed to be canceled in the ratio of the power spectra $S(f,F)/S_{\text{ref}}(f,F)$.

2.2.2 Physical phantoms

Two physical phantoms were used for validation. Both cylindrically shaped phantoms had a 90 mm diameter and 39 mm height. The phantoms were constructed from agarose, n-propanol, condensed milk, and water with glass bead scatterers uniformly placed in the phantom spatially at random. The size ranges and concentrations of the glass beads in the two phantoms are described in Table 2.1.

Table 2.1: Size ranges and concentrations of glass beads in physical phantoms A and B.

	Phantom A	**Phantom B**
Glass bead diameters (µm)	75–90	9–43
Concentration	$5/\text{mm}^3$	$800/\text{mm}^3$

For each phantom, the attenuation coefficient was estimated using an insertion loss approach. The attenuation from phantoms A and B were found to be $\alpha_A(f)$=$0.41f^{1.15}$ dB/cm and $\alpha_B(f)$=$0.79f^{1.05}$ dB/cm, respectively, over the frequency range from 4.8 to 8 MHz. Furthermore, both phantoms had layers of saran wrap at the top and bottom to protect the agar matrix and act as acoustic windows. The effects of the saran layer were compensated using the physical parameters and the Eq. (3) described in [38]. The phantoms

were constructed according to the recipe in [39]. According to the literature, phantoms of this type have a B/A of 6.6 $\pm$ 0.3 [40].

2.2.3 RF data acquisition

RF data acquisition was performed in a water filled tank using two scenarios. First, a low power pulser/receiver was used in order to minimize the presence of nonlinear distortions. Second, a high power unit was used in order to produce higher ultrasonic pressures and nonlinear distortion of the ultrasound signal. For both scenarios, a spherically focused single-element transducer with a 5 MHz nominal frequency (ISR054, NdtXducer LLC, USA), 12.5 mm diameter and 25.4 mm focal length was used. The planar reflector was Plexiglas with reflectivity γ=0.37. Figure 2.1 depicts the acquisition setup.

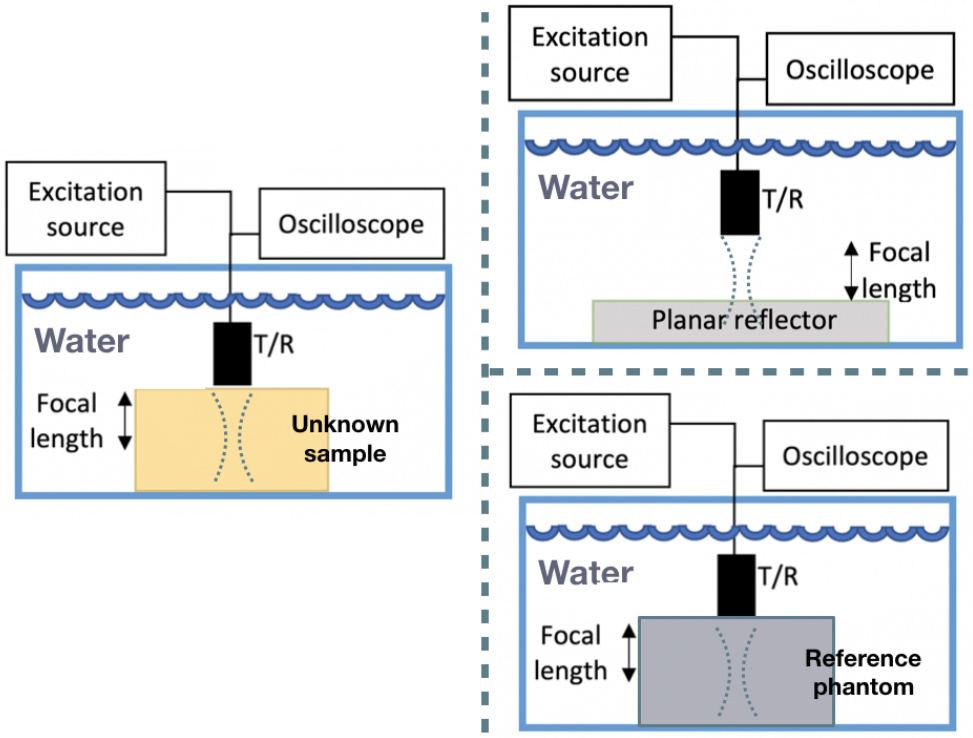

Figure 2.1: RF acquistion setup. Backscattered signals around the focal region were used for BSC estimation.

Low Power and High Power acquisition

In the low power acquisition, the excitation signal for the transducer was generated with a pulser/receiver (5800PR, Panametrics Olympus, USA). Figure 2.2(a) shows a pulse generated by the pulser/receiver when using the low power setting and its corresponding power spectrum. The RF data from a sample phantom were recorded to a PC using a 14-bit UF3-4121 A/D card with 250 MHz sampling frequency (Strategic Test Corporation, Woburn, MA). Successive RF signals from a sample were captured by moving the transducer in the horizontal plane above the sample in a grid of 20 mm $\times$ 20 mm with steps of 2 mm in both directions. In addition, RF signals from a planar reflector were acquired using the same settings. However, the transducer was moved along the transducer axis in a step size of 0.5 mm such that the signals from the reflector were recorded throughout the depth of field of the transducer.

Large ultrasonic pressures were utilized to visualize the nonlinear distortion; therefore, a high power pulser/receiver (RAM-5000, Ritec Inc., USA) was used to generate high ultrasonic pressures. Specifically, six different excitation levels (EL) were used in the experiments corresponding to peak-to-peak voltages between 381 and 1168 V. The excitation signal for the transducer was a 1-cycle tone burst with a center frequency of 5 MHz. RF signals were recorded by an oscilloscope (LeCroy Wavesurfer 44Xs). Figure 2.2(b) shows the excitation signal when using the high power settings and recorded with a broadband needle hydrophone. It should be noted that subsequent band pass filtering by the 5 MHz transducer will occur on both transmit and receive.

The peak positive pressure and peak negative pressure with the low power and high power settings were measured using a needle hydrophone (Precision Acoustics Ltd., UK). The needle hydrophone was located along the transducer axis to obtain the maximum peak positive pressure at the largest high power excitation level. Table 2.2 lists the peak positive pressure and peak negative pressure associated with the settings used in the present experiments.

Using the peak positive pressure in Table 2.2, the Gol'dberg number for the low power settings were $\Gamma_{\text{water}} = 34.9$, $\Gamma_{\text{A}} = 0.9$, and $\Gamma_{\text{B}} = 0.5$. On the other hand, for high power settings, $\Gamma_{\text{water}} \in (403.1, 643.4)$, $\Gamma_{\text{A}} \in (10.4, 16.6)$, and

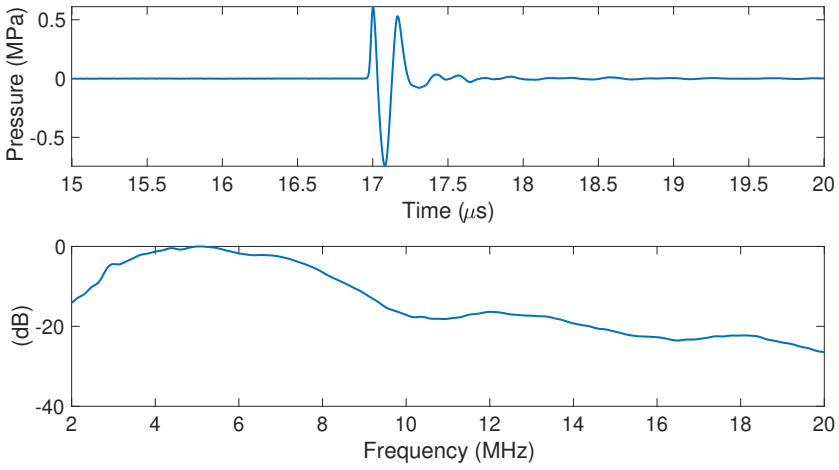

(a) Low power setting

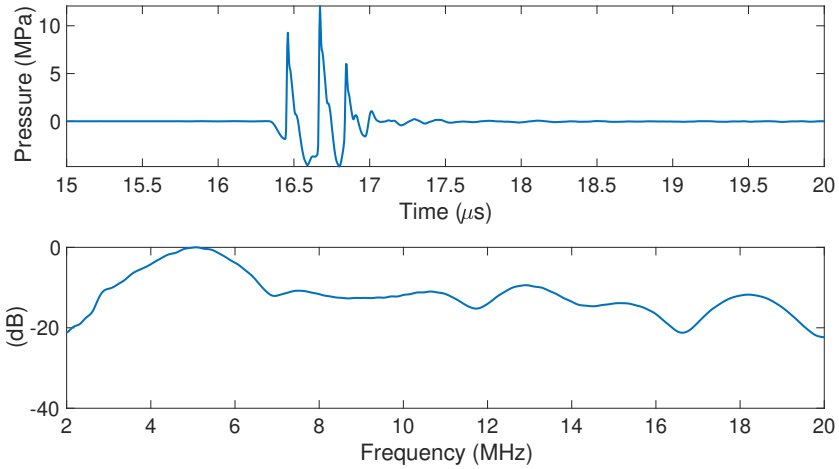

(b) High power setting (EL6)

Figure 2.2: Representative signals and their respective power spectra measured with a needle hydrophone for the low power setting (a) and high power setting with the largest excitation level (b).

$\Gamma_B \in (6.3, 10.1)$. Hence, based on the estimated Gol'dberg numbers, strong nonlinear distortion in the signals are expected using the planar reflector method.

In order to explore the importance of nonlinear distortion and harmonic generation on the accuracy of BSC estimation we used the KZK equation and simulator to attempt to match the experimental conditions and examine the harmonic generation of references and samples [41, 42]. The KZK equation was used to obtain pulse shapes when propagating through media equivalent to phantoms A and B using a 5 MHz transducer and through water. We used the experimentally determined positive peak pressures from Table II to

Table 2.2: Summary of peak positive pressure and peak negative pressure values associated with the settings used, measured using a needle hydrophone at the focus of the transducer.

	Peak positive pressure (MPa)	Peak negative pressure (MPa)
	Low Power	
Excitation level 1	0.66	0.75
	High Power	
Excitation level 1	7.58	2.78
Excitation level 2	9.10	3.38
Excitation level 3	10.22	3.83
Excitation level 4	11.02	4.21
Excitation level 5	11.54	4.52
Excitation level 6	12.10	4.74

find parameters that matched the KZK peak positives pressures in water. Once we found the six source pressures for the KZK simulator, we repeated the simulations modifying the B/A and attenuation parameters that fit the values for phantoms A and B. Figure 2.3 shows the simulated waveforms and their power spectra at the focus of the 5 MHz transducer. The simulation results predict that the nonlinear distortion will be less for phantom B than for phantom A due to the larger attenuation of phantom B (second harmonic is at 20.4 dB below fundamental for phantom B, 12.5 dB for phantom A and 7 dB for water). Therefore, the KZK simulations suggest increased effects on the BSC estimation due to nonlinear distortion when using a water path for the reference technique.

Linearity of transducer

For the high power excitation signals, we verified that the transducer was operating in the linear regime. Figure 2.4, shows the peak-to-peak acoustic pressures measured with a needle hydrophone (Precision Acoustics Ltd., UK) when located a few millimeters from the transducer surface, i.e., where acoustic nonlinearity is expected to be negligible. The acoustic pressures at the output of the transducer were observed to increase linearly with the peak-to-peak voltage of the corresponding excitation level up to 800 V. At excitation voltages higher than 800 V the pressure increase was no longer linear and presumably at high enough voltages the transducer output would

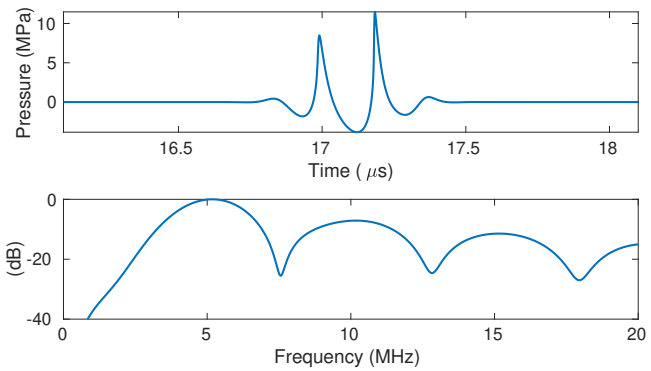

(a) KZK - water

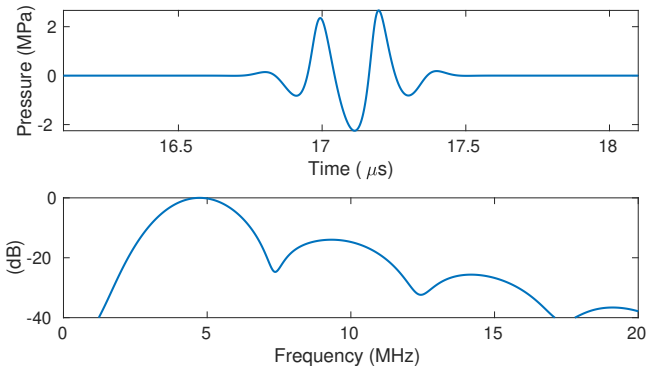

(b) KZK - phantom A

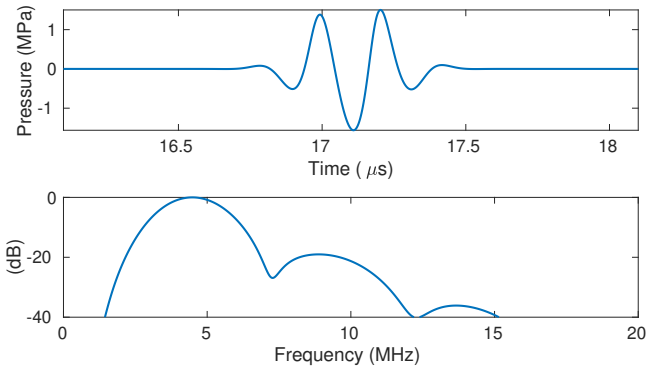

(c) KZK - phantom B

Figure 2.3: Representative signals and their respective power spectra at the focal length simulated with KZK. The signals were simulated to match the peak positive pressure at the focal length in water (a) for the high power setting with the largest excitation level. Waveforms corresponding to propagation through phantoms A (b) and B (c) showed that the second and third harmonics are 14.5 dB and 26.5 dB below the fundamental band for phantom A; and 20.4 dB and 38.4 dB below the fundamental band for phantom B and 26.5; whereas for water path propagation the harmonics were only 7 dB and 11.3 dB below the fundamental band in water, respectively.

saturate. However, any nonlinearity introduced by the transducer could be taken into account through the calibration process.

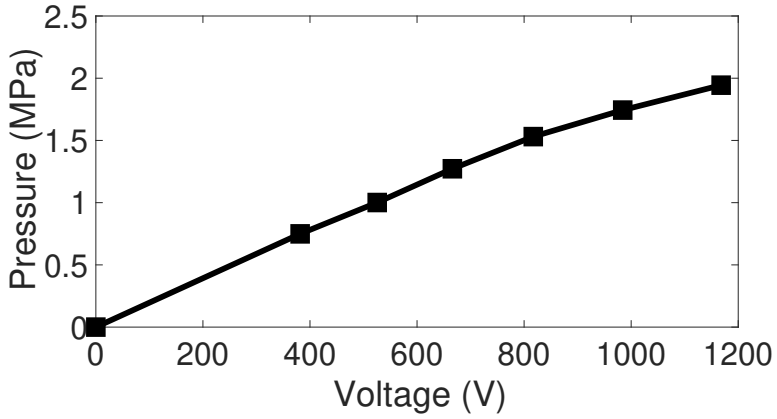

Figure 2.4: Acoustic pressures (close to the transducer surface) vs. high power peak-to-peak voltages used. The pressure was observed to increase linearly with excitation voltage up to 800 V with nonlinear behavior beginning to appear for the last two excitation levels.

BSC estimation procedures

In order to compute the BSCs, 121 independent scan lines were gated—around the focal length 25.4 mm—and a power spectrum was calculated from each scan line. The analysis bandwidth in both low and high pressure scenarios was chosen to correspond to -10 dB bandwidth. Pre-processing was performed on the echo signals by applying a bandpass filter between 1 and 50 MHz to improve SNR of the backscattered signals. For BSC estimation, an averaged power spectrum was calculated from the power spectra of 121 scan lines to reduce the noise in the BSC estimates.

The first BSC values were estimated using the low power acquisition setting and the planar reflector method for phantoms A and B, respectively. The BSCs obtained using the low power setting and the planar reflector method were subsequently utilized as the ground truth BSCs and also as the $\sigma_{\text{ref}}(f)$ when computing the BSC with the reference phantom method.

When using high power settings and the planar reflector method, six BSCs were computed for each phantom A and B, corresponding to the six excitation levels used, i.e., from $\sigma_{\text{HP-1}}(f)$ to $\sigma_{\text{HP-6}}(f)$. When using high power settings and the reference phantom method, six BSCs were computed for

the phantoms A and B, respectively, corresponding to the six excitation levels. For estimating BSCs of A, the reference phantom was phantom B, and vice-versa.

2.2.4 Metrics

Three metrics—the power fit exponent, root mean square error, and effective scatterer diameter—were used for performance comparison of the BSC estimation strategies in the nonlinear acoustic regime.

Power fit exponent

The BSC was fit to a power law function such as $\sigma(f) = bf^n$ in order to obtain the frequency dependence exponent n. The exponent n provides a simple parameter describing the frequency dependence of the BSC. For example, n=4 corresponds to Rayleigh scattering. Moreover, the exponent n is related to other quantitative ultrasound parameters such as the effective scatterer diameter (ESD). Rearranging by taking the logarithm of the Taylor's series expansion of the $\sigma(f)$=bf^n and approximating to the line around the center frequency f_0 gives

$$\log\left(\sigma(f)\right) \approx \log(b) + n\log(f_0) + \boldsymbol{(n/f_0)}f. \tag{2.3}$$

Thus, n can be computed as the slope of the natural logarithm of the BSC vs. frequency, scaled by f_0.

Root mean square error

The normalized root mean square error between BSC estimates from different power settings was computed as

$$\text{RMSEx} = \frac{\|\sigma_{\text{HP-x}}(f) - \sigma_{\text{LP}}(f)\|}{\|\sigma_{\text{LP}}(f)\|} \tag{2.4}$$

where the subscripts HP-x and LP correspond to the BSCs using high power setting x (with x $\in \{1, 2, \cdots, 6\}$) and low power setting, respectively. The low power estimate of the BSC was used as a baseline reference.

Effective scatterer diameter

The ESD was estimated from the BSC by searching values of an effective scatterer radius, a_{eff}, that minimized the average squared deviation [43] between the estimated BSC and the BSC derived from Faran theory [44]. The search of a_{eff} ranged from 0.5 to 100 µm. The theoretical BSC was estimated through the Faran's scattering theory given the properties of the glass bead scatterers (density: 2380 kg/m^3, speed of sound: 5572 m/s, Poisson's ratio: 0.21) and the surrounding medium (density: 1540 m/s, speed of sound: 1020 kg/m^3).

2.2.5 *B/A* offset of the reference phantom

We did not have access to phantom materials with *B/A* values outside of the range of 5.8 to 6.6. Therefore, to assess the effects of nonlinear distortion when the reference *B/A* material had a larger mismatch to the sample, we acquired additional data by adding a layer of corn oil on top of the reference material and having a standoff to the phantom. Corn oil has acoustic properties close to that of soft tissue, i.e., density: 920 kg/m^3, speed of sound: 1466 m/s, and attenuation 1.24 dB/cm at 4.5 MHz [40]. However, corn oil has a *B/A* of 10.6, which is at the high end of what is expected to be encountered in tissue. Therefore, the corn oil standoff simulated having a reference phantom with a higher degree of nonlinear distortion than using the reference phantom alone with no standoff. Figure 2.5 depicts the acquisition setup using a reference phantom with a corn oil standoff of approximately 17 mm. This standoff was selected in order to place the focus just below the reference phantom surface for selection of reference backscattered signals within the depth of focus of the source.

2.3 Results

In this section, the power spectra—utilized calculate BSCs—and the BSCs are shown to note the effects of the nonlinear distortion vs frequency. The three metrics and the special case of a large *B/A* mismatch between sample and reference are presented as well.

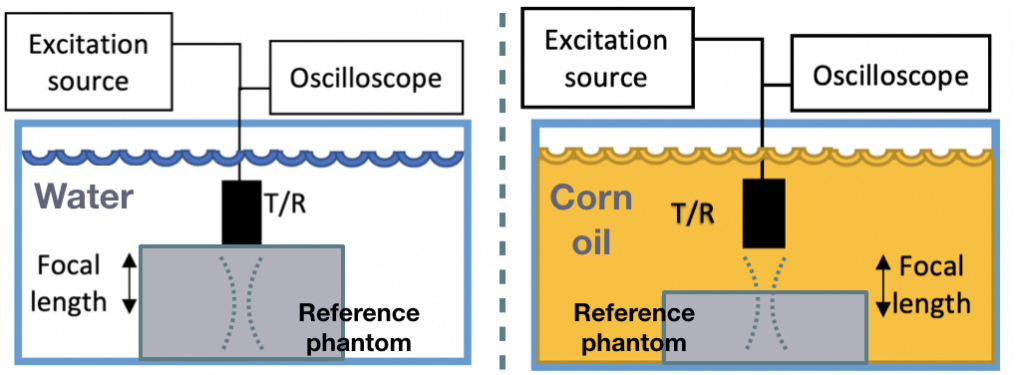

Figure 2.5: RF acquisition in the reference phantom method (left) and when using a a corn oil stand off to increase nonlinear distortion (i.e., standoff of 17 mm thickness, whereas the focal length was 25.4 mm). Backscattered signals were acquired in the focal region for BSC estimation.

2.3.1 Power Spectra

Figure 2.6 shows the power spectra when using the low power setting (one excitation level) and high power settings (six excitation levels). Power spectra were estimated from phantoms A and B, and the Plexiglas planar reflector. The power spectra in high power settings had a narrower bandwidth than the power spectra in low power settings, which is a result of the different systems used to generate the low and high power settings.

2.3.2 BSC results

The first BSC estimation approach that was evaluated was the planar reflector method using the low power setting. Figure 2.7 shows the BSCs from the phantoms A and B, respectively. The analysis bandwidth was 3 to 6.4 MHz, which corresponded to a fractional bandwidth of approximately 70%.

Figures 2.8(a) and 2.8(c) show the BSC estimated using the planar reflector method and high power settings, i.e., excitation levels from 1 to 6, for phantoms A and B, respectively. In both phantoms, BSCs estimated using the planar reflector method and increasing excitation levels followed the ground truth BSC for low frequencies but increasingly deviated at high frequencies.

Figures 2.8(b) and 2.8(d) show the BSC estimated using the reference phantom method and high power acquisition settings. For estimating the

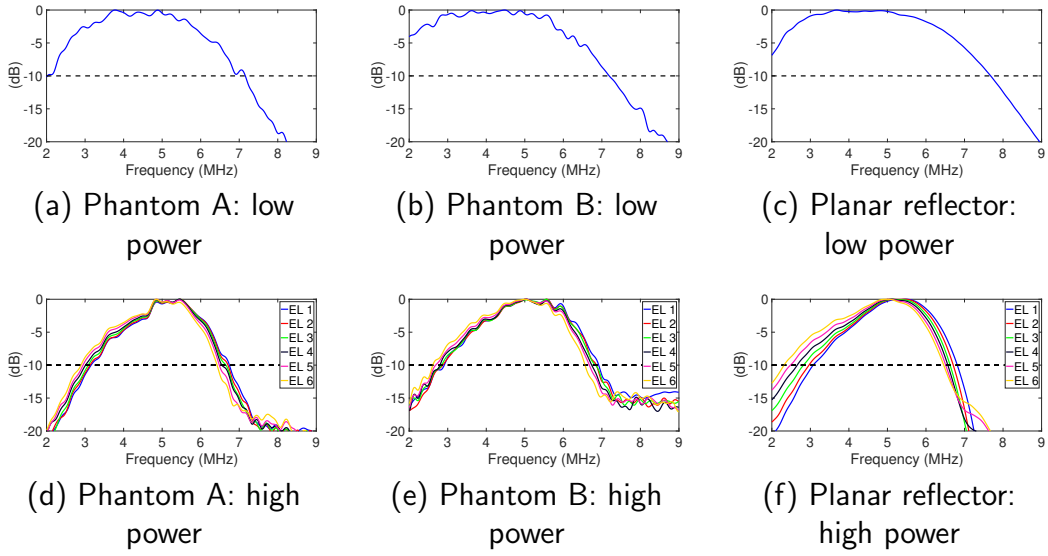

(a) Phantom A: low power (b) Phantom B: low power (c) Planar reflector: low power

(d) Phantom A: high power (e) Phantom B: high power (f) Planar reflector: high power

Figure 2.6: Normalized power spectra (to their corresponding maxima) used for BSC estimation using the low power setting (top) and high power settings (bottom, 6 excitation levels) for phantom A (a)(d), phantom B (b)(e), and the Plexiglas planar reflector (c)(f). The −10 dB below the maximum is depicted in dashed lines.

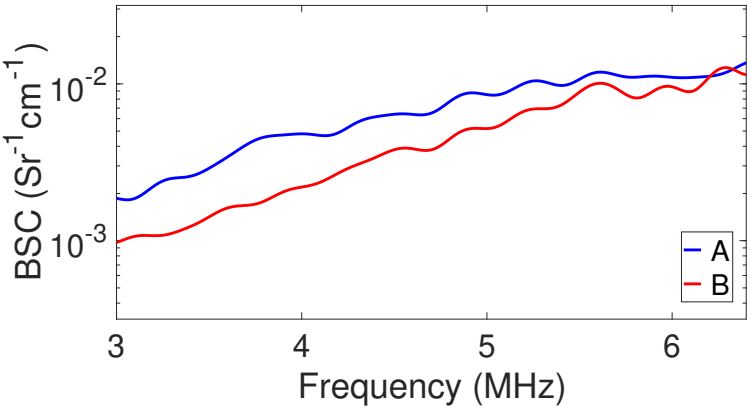

Figure 2.7: BSCs from phantom A (blue) and B (red) when using the planar reflector method and low power settings.

BSCs of the phantom A, the $\sigma_{\text{ref}}(f)$ used was $\sigma_{\text{LP}}(f)$ of B, whereas for estimating the BSCs of the phantom B, the $\sigma_{\text{ref}}(f)$ used was $\sigma_{\text{LP}}(f)$ of A. In both phantoms, BSCs estimated using the reference phantom technique were closer to the ground truth BSC throughout the analysis bandwidth compared to the Plexiglas reference data.

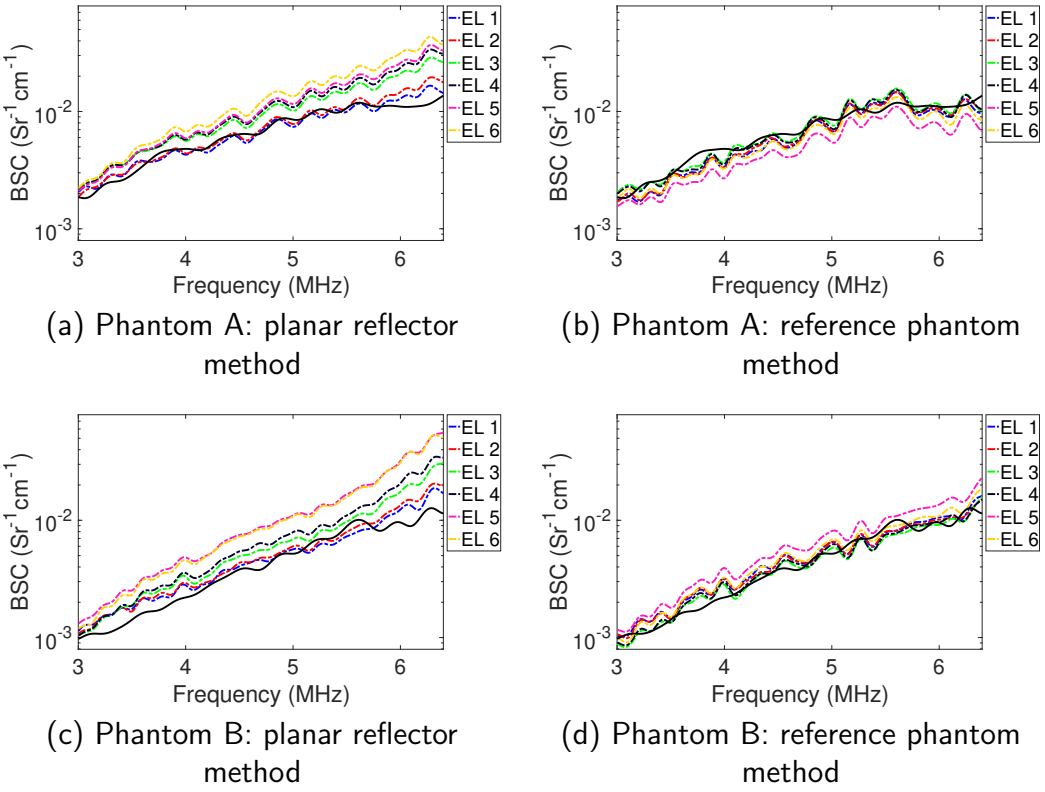

(a) Phantom A: planar reflector method

(b) Phantom A: reference phantom method

(c) Phantom B: planar reflector method

(d) Phantom B: reference phantom method

Figure 2.8: BSC estimates from phantom A (top) and phantom B (bottom) when using the planar reflector method (left) and the reference phantom method (right) with high power settings (6 excitation levels). Solid lines are the baseline BSCs estimated using the low power settings (from Figure 2.7).

2.3.3 Exponent n results

Estimated values of n, when fitting the BSC to a power function $\sigma(f) = bf^n$, for the low power setting were 2.6 and 3.7 for phantoms A and B, respectively. For phantom A, when using the planar reflector method the values of n were 2.5 at the lowest high power setting of 1 and increased monotonically to 3.6 for the largest high power setting of 6. Using the reference phantom technique, no monotonic increase was observed as the settings increased. The estimated value of n averaged across the settings was 2.61 ± 0.12. Similarly for the phantom B, when using the planar reflector technique a monotonic increase in the estimate of n was observed starting with a value of 3.48 at the lowest high power setting of 1 and increasing to 4.77 at the largest high power setting of 6. Using the reference phantom technique resulted in minor changes in estimated values of n versus settings, i.e., the mean value of n

estimated across the settings was 3.7 ± 0.12. From Figure 2.9, the estimated n values were more stable when using the reference phantom method and did not result in increased error in the estimate versus higher power settings. These patterns were observed in both phantoms.

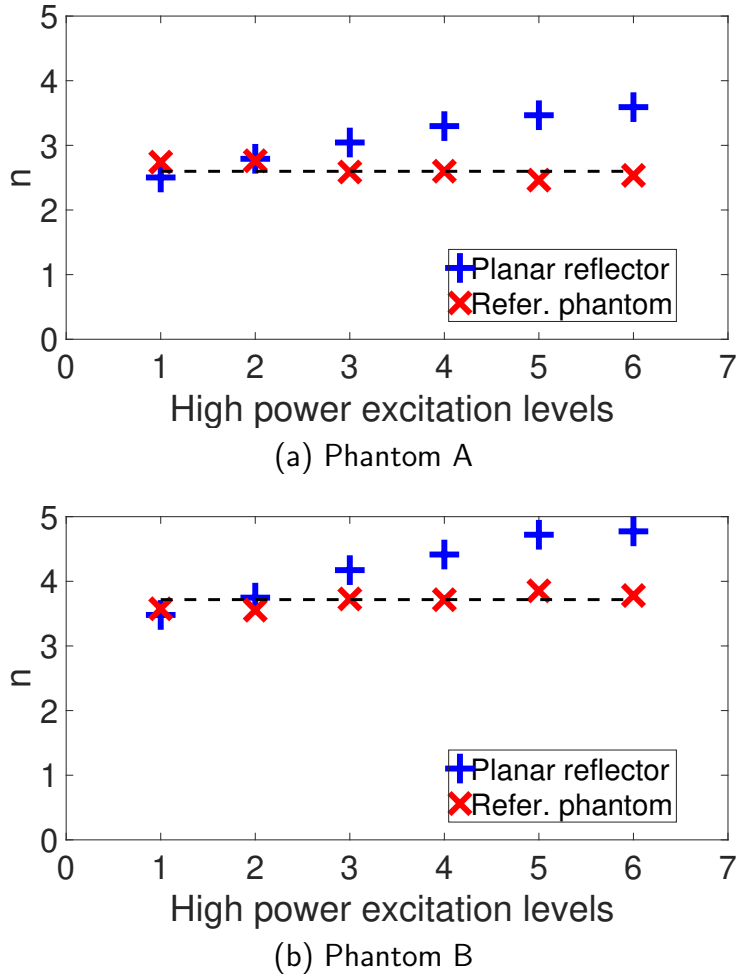

Figure 2.9: Estimates of exponent n versus different excitation levels when fitting $\sigma(f) = bf^n$, using the planar reflector method and the reference phantom method for phantoms A (top) and B (bottom). The dashed lines correspond to the n values obtained using low power settings.

2.3.4 RMSE results

The RMSEs of the high power BSCs were computed with the low power BSC as ground truth to quantify the differences when high power excitation levels were used. The mean and standard deviation of the RMSE for phantom

A were 0.62 ± 0.42 and 0.21 ± 0.06 using the planar reflector method and the reference phantom method, respectively. Similarly, for phantom B, the RMSE values were 0.98 ± 0.77 and 0.25 ± 0.12 using the planar reflector method and the reference phantom method, respectively. Figure 2.10 shows the RMSEs for phantoms A and B at each excitation level. The values of the RMSEs had lower variation for different excitation levels when using the reference phantom method. In contrast, the planar reflector method produced a wide range of RMSE values depending on the excitation level used.

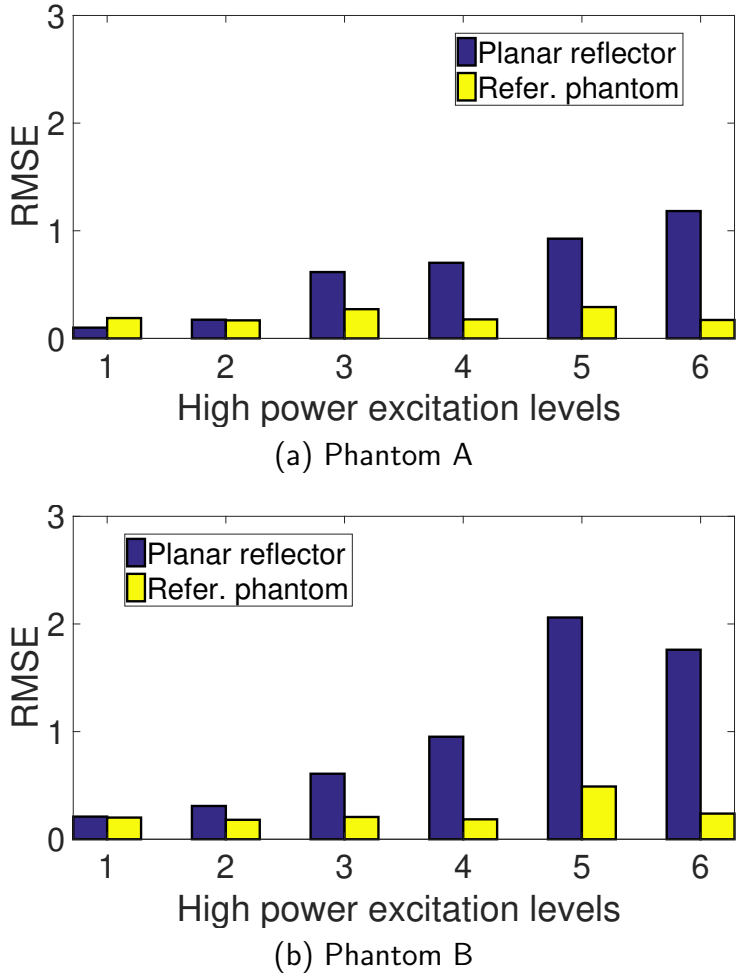

Figure 2.10: Normalized RMSE values of the high power BSCs with respect to the low power BSC for phantoms A (top) and B (bottom) when using the planar reflector method (blue bars) and the reference phantom method (yellow bars).

2.3.5 ESD results

Estimated values of ESD when using the low power settings were 75 µm and 39 µm for phantoms A and B, respectively. When estimating the ESD using the high power settings, the variation of the ESD depended on the method of calibration. Figure 2.11, shows the mean estimates of the ESD at each power setting for both the planar reflector technique and the reference phantom technique. For phantom A, when using the planar reflector method, at the power setting 1, the ESD estimate was 76 µm and decreased monotonically to an ESD estimate of 45 µm with the highest power setting of 6. When using the reference phantom method, no monotonic decrease in ESD was observed and across the settings the mean value of the ESD estimate was 74.7 ± 2.3 µm. Similarly, for phantom B, when using the planar reflector method the ESD estimates at a power setting of 1 was 47 µm and by a power setting of 3 the ESD estimate collapsed to a value of 0.5 µm. When nonlinear distortion occurs, higher frequencies distort more rapidly than lower frequencies resulting in a downshift in the center frequency of the reference spectrum, as evidenced by Figure 2.6(f). When dividing the sample spectrum by the distorted reference spectrum, the slope of the estimated BSC is increased. The slope of the BSC increases as the excitation level increases, resulting in progressively smaller estimates of ESD. On the other hand, the reference phantom method provided consistent estimates of ESD at all power settings with a mean ESD estimate across all settings of 39.2 ± 5.6 µm.

2.3.6 *B/A* mismatch in the reference phantom

The results of BSC estimates when introducing a mismatch between the *B/A* values of the the sample and reference phantom through a corn oil standoff are shown in Figure 2.12. The root mean squared error between BSC estimates acquired at the highest excitation level 6 and BSC estimates at the excitation level 1 was 8.6% and 10.2% for phantoms A and B, respectively, when no corn oil standoff was present. Using the corn oil standoff, the errors were 8.2% and 36% for phantoms A and B, respectively. Therefore, the mismatch of *B/A*can produce substantial error (more than 30%) in the case when phantom A was used as the reference. When the phantom B was used as reference, the error between the BSC estimates from phantom A at the different excitation

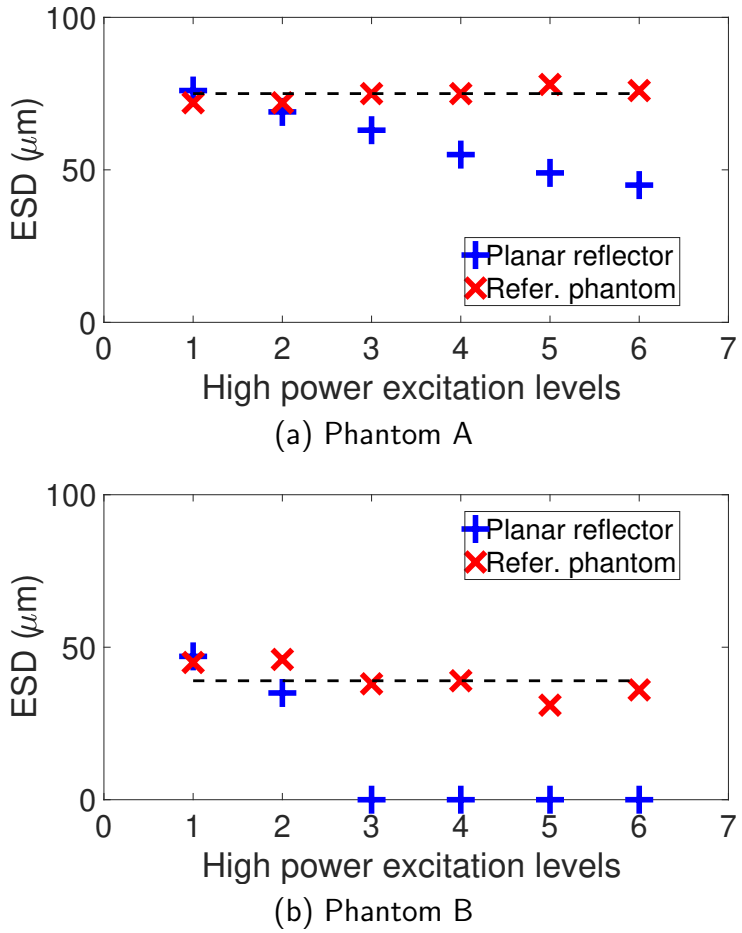

Figure 2.11: ESD estimates of phantoms A (top) and B (bottom) using six high power settings. The dashed lines correspond to the ESD estimate with low power settings.

levels was similar with and without the corn oil standoff on the reference. Therefore, when using the reference phantom technique a mismatch in B/A values from the reference to the sample can result in BSC error. However, the attenuation of ultrasound reduces the nonlinear distortion effects on the BSC estimate, which is evidenced by the higher attenuation in phantom B.

2.4 Discussion

We demonstrated in physical phantoms that the BSC estimated using the reference phantom method had less sensitivity to nonlinear distortion than the planar reflector method. The phantoms used were chosen to have attenuating properties that are similar to those found in soft tissues. For example,

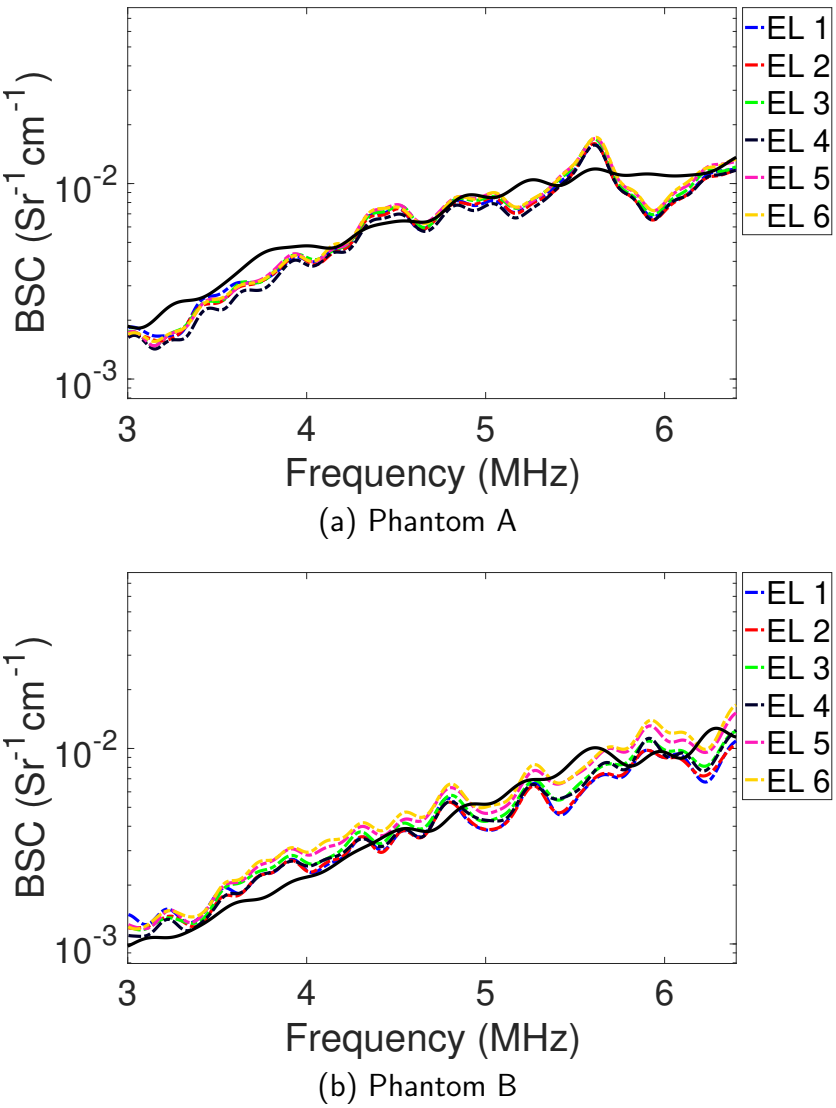

Figure 2.12: BSC estimates from phantom A (top) and phantom B (bottom) when using a calibration reference signal with larger B/A. Solid lines are the baseline BSCs estimated using the low power settings (from Figure 2.7) and the dashed lines represent the BSC estimated at different power levels.

in [37] a large number of soft tissues could be characterized by an attenuation coefficient of 0.54 ± 0.37 dB/cm at 1 MHz and nonlinear parameter of $B/A = 7.5 \pm 1.1$

Power spectra were confirmed to be sensitive to amplitude variations of the excitation signals with distortions in the power spectra shape due to nonlinear wave propagation effects. In Figures 2.6(d)–(f), it can be observed that the normalized power spectra shifted to lower frequencies. The shift to lower frequencies results from the acoustic nonlinearity of the medium.

Higher frequencies more rapidly distort due to acoustic nonlinearity, transferring energy to higher harmonics, as can be ascertained from the Gol'dberg number, which is inversely proportional to wavelength. In addition, the magnitude of the fundamental bandwidth is decreased as energy is transferred from the fundamental to the higher harmonics resulting in an apparent excess attenuation of the fundamental [34]. This phenomena is highlighted in Figure 2.6(f), where the propagation of the ultrasound through water at high pressures resulted in an increasingly larger shift to lower frequencies in the spectrum reflected off of the planar reflector. These results suggest that the nonlinear distortion from the water path propagation using the planar reflection method combined with the low attenuation of water was the source of the distortion to the BSC estimates observed in the data.

Using the planar reflector method with high power acquisition settings, the BSC estimates were increasingly divergent from the BSC obtained using the low power settings. The BSC curves in Figure 2.8 had a larger variation when estimated using the planar reflector method in comparison to the BSC curves obtained using the reference phantom method. The B/A values for the phantoms (B/A assumed 6.6) were larger than that of water (B/A=5). However, the attenuation was larger in the phantoms resulting in smaller Gol'dberg numbers. Therefore, the nonlinear distortion of the reference spectra from the phantoms was smaller than observed for the planar reflector. The result from these subtle differences in calibration techniques suggest that the reference phantom technique would provide more consistent estimates of the BSC. Thus, when using high ultrasonic pressures to increase the SNR for BSC estimation, these results indicate that the reference phantom technique should be used and the planar reflector technique avoided.

In the next set of experiments, we examined the parameterization of the BSC by considering nonlinear distortion introduced through the calibration method. Similar behaviors were observed when fitting the BSC to a power law and when extracting the ESD for the glass beads in the phantoms. Estimates that were obtained using the planar reflector technique demonstrated trends where the estimates at higher excitation energies became increasingly divergent from the low power estimates of the parameters. The exponent n is another parameter that was found less consistent with BSC curves obtained using the planar reflector method. These findings might be crucial for an application such as tissue characterization where either the exponent n or

the ESD are derived directly from the shape of the BSC. In that scenario, malignant cells (typically larger structures with small n) might be misinterpreted as healthy cells (smaller structures with larger n) only based on the exponent n and its similarities with Rayleigh scattering.

The ESD values were in better agreement (scatterer diameters from Table 2.1) when using the reference phantom method. For example, in phantom B, the ESD values obtained for excitation settings larger than 2 using the planar reference were 0.5 µm, which was the minimum value possible. In other words, the ESD estimation lost accuracy as the signal power increased. This again supports the importance of using a reference method that minimizes the effects of nonlinear distortion. Hence, the planar reflector method, under certain high power settings, provided ESD estimates that did not correspond to anything meaningful.

In the reference phantom method, the mismatch of the B/A parameter between the sample and reference phantom, through the use of a corn oil standoff, suggests that mismatches in nonlinear distortion between the reference and the sample can still result in BSC estimation error. However, due to the low attenuation of water, the reference phantom technique still provides better BSC estimates because the nonlinear distortion from the reference can be controlled through choice of B/A properties and attenuation of the fabricated phantom. The reference phantom can have a larger B/A value than water, but results in less nonlinear distortion because the attenuation of the phantom is much larger than that of water, which is the typical propagation medium used in the planer reflector method.

The main reason for using higher excitation settings for estimating the BSC and associated parameters is to increase the SNR. Low SNR results in higher bias and variance of estimates. However, higher pressure values can also lead to higher nonlinear distortion effects, which in turn can lead to increases in estimate bias and variance. Therefore, the results shown suggest that to improve BSC estimate bias and variance, high ultrasonic powers can be used, but should be used with a reference medium that allows a low Gol'dberg number. This is difficult to achieve with water as the propagation pathway, which is why the reference phantom method provided better estimate performance. However, a planar reflector method could potentially provide good estimates without nonlinear distortion if another propagation medium were used instead of water that resulted in a low Gol'dberg number,

i.e., a medium that balanced the B/A value with a higher attenuation. Another alternative to overcome the strong harmonic generation due to a water propagation with the planar reflector method would consist of using a low power setting for the reference acquisition and scaling the setting to higher power for the sample acquisition. Less nonlinear distortion will occur due to the low signal level of the reference. The BSC can then be estimated with the low power reference by correcting with the scaling factor, assuming the scaling factor can be accurately known.

2.5 Conclusion

In this chapter, the bias and variance of two BSC estimation methods were compared when nonlinear distortion was present. The findings suggest that accuracy of the planar reflector method when using a water propagation path is more sensitive to nonlinear distortion effects than the reference phantom method. In general, the reference phantom method provided more consistent BSC estimates when finite amplitude waves (i.e., not small acoustic pressures) were used during the RF data acquisition, thus improving the consistency of the BSC for tissue characterization.

CHAPTER 3

EFFECTS OF ACOUSTIC NONLINEARITY ON PULSE-ECHO ATTENUATION COEFFICIENT ESTIMATION

3.1 Introduction

Spectral-based methods in pulse-echo mode for attenuation estimation *in vivo* using backscattered signals assume that the power spectrum from some block of data is proportional to the product of the system acquisition effects (scanner, transducer, and diffraction) along with effects derived from intrinsic acoustic properties of the medium (cumulative attenuation and BSC) [45]. In the nonlinear regime, however, the power spectra from a block of data in a sample and its calibration power spectra could undergo different nonlinear distortions as shown by D'hooge et al. [22]. For pulse-echo, D'hooge et al. [22] found an overestimation of the attenuation coefficient when the calibrated signal developed less nonlinear distortion with respect to the 'sample' signal. Similarly, in pulse-echo experiments and due to nonlinear distortion, the amplitudes of the envelopes of backscattered signals from a block of data are susceptible to changes of the input pressure levels [34]. Fatemi et al. [34] found that an increment of the peak pressure as low as 9 dB could generate strong distortion of the echo envelope of a transmitted pulse measured from a wire target. Such distortions in the echo envelope manifest as excess attenuation at the larger input pressure levels, i.e., the estimated attenuation of the medium can be dependent on the input pressure level. This phenomenon occurs due to the inherent acoustic nonlinear propagation in the propagation path between the transducer and the targeted region.

A descriptive parameter for nonlinearity, called the Gol'dberg number, provides a rule of thumb to predict the degree of acoustic nonlinearity anticipated during the transmission of a plane wave with frequency f_0 in a lossy media. The Gol'dberg number is computed as $\Gamma = \frac{\beta k M}{\alpha(f_0)}$ [36], where k is the wave number, $\beta = 1 + \frac{B}{2A}$, is the nonlinearity coefficient of the

medium, M is the Mach-number equal to the particle velocity amplitude at the source divided by the equilibrium sound speed of the medium, and $\alpha(f_0)$ is the attenuation coefficient of the medium. $\Gamma \ll 1$ predicts the acoustic nonlinearity to be negligible, whereas $\Gamma \gg 1$ predicts significant nonlineariti can be expected to develop. Moreover, a large Gol'dberg number implies that a non-negligible generation of harmonics ($2f_0$, $3f_0$, etc.) and energy transferred out of the fundamental frequency f_0 occurs at short propagation distances. Similar behavior (generation of harmonics) could be expected for a broadband pulse wave propagation where there is a band of frequencies propagating rather than a mono-frequency wave, in which case 2nd and 3rd harmonic bands are generated out of energy from the fundamental frequency band.

Most pulse-echo based attenuation estimation methods use the power spectra of the fundamental frequency band. In Chapter 2 and [46], we demonstrated that the presence of nonlinear distortion adversely affects estimates of the BSC changing both the slope and magnitude of the backscatter coefficient spectrum. The slope of the BSC is affected by nonlinearity because the strength of the nonlinear distortion is higher with higher frequency. Therefore, we aim to quantify how much the harmonic generation might also lead to inaccuracies in attenuation coefficient estimation when using a spectral-based estimation method, especially when large acoustic pressures are used. In the present chapter, we analyzed a representative method for attenuation coefficient estimation in the frequency domain, namely, the spectral log difference (SLD) method for estimating the attenuation coefficient. It should be noted that the SLD method diverges from the log spectral difference in [22] because we used an external reference phantom to compensate for diffraction effects of moderate focusing without being restricted to plane wave assumptions. In the study presented in this chapter, analysis of attenuation coefficient estimation accuracy in the presence of nonlinear media will first be performed in numerical simulations using the k-Wave toolbox [47] and then corroborated with experiments in physical phantoms. The acoustic pressure amplitudes used in the study were within the FDA (Food and Drug Administration) regulated limits for diagnostic ultrasound determined by the mechanical index ($\mathrm{MI} \equiv \frac{\mathrm{PNP}}{\sqrt{f_0}} < 1.9$), where PNP is the peak negative pressure (after derating by a factor of 0.3 dB/cm/MHz when measured in water). In this chapter, we will expand the work of [22] to non-negligible diffraction effects of focused

sources but also we will relate the excess attenuation with the Gol'dberg number defined for lossy media.

3.2 Methods

The spectral log difference method—technique used to estimate the attenuation coefficient—is described in this section. The validation of the hypothesis was performed after estimating attenuation coefficients using data from computer simulated phantoms, and physical phantoms. The data acquisition procedure is also detailed in this section.

3.2.1 Spectral log difference

Assuming linear acoustic propagation, the power spectra of two gated windows (proximal and distal relative to the transducer surface) in a sample can be written as

$$S(f, z_p) = P(f)D(f, z_p)\sigma(f, z_p)e^{-4\alpha_S(f)(z_p)},$$

$$S(f, z_d) = P(f)D(f, z_d)\sigma(f, z_d)e^{-4\alpha_S(f)(z_d)},$$

where z_p and z_d stand for the depths of proximal window and distal window, respectively. $D(f, z_p)$ and $D(f, z_d)$ correct for the beam diffraction at the locations of the gated windows, *P(f)* includes the frequency-dependent effects of the system acquisition and transducer, $\sigma(f, z_p)$ and $\sigma(f, z_d)$ correspond to the BSCs of the gated windows, and $\alpha_S(f)$ is the attenuation coefficient of the sample. Assuming a region with uniformly distributed scatterers spatially, $\sigma(f, z_p) \propto \sigma(f, z_d)$, then only the diffraction effects need to be compensated for estimation of $\alpha_S(f)$. For this purpose, additional backscattered signals are acquired from a well-characterized reference phantom using the same acquisition settings and transducer. The power spectra from two gated windows in the reference phantom located at the same axial positions as those used in the sample are

$$S_R(f, z_p) = P(f)D_R(f, z_p)\sigma_R(f, z_p)e^{-4\alpha_R(f)(z_p)},$$

$$S_R(f, z_d) = P(f)D_R(f, z_d)\sigma_R(f, z_d)e^{-4\alpha_R(f)(z_d)},$$

where the subscript R stands for the reference phantom. If the speed of sound of the reference phantom matches the speed of sound of the sample then $D(f, z_p) \approx D_R(f, z_p)$ and $D(f, z_d) \approx D_R(f, z_d)$. Therefore, the attenuation coefficient can be computed as

$$\alpha_S(f) = \alpha_R(f) + \frac{1}{4(z_d - z_p)} \log \left[\frac{S(f, z_p)S_R(f, z_d)}{S(f, z_d)S_R(f, z_p)} \right]. \tag{3.1}$$

A parameter derived from $\alpha_S(f)$ that is commonly used is the attenuation coefficient slope, i.e., the slope of the linear fit of $\alpha_S(f)$ with respect to $f \in (f_L, f_H)$, where f_L and f_H correspond to the lower and upper frequencies of an analysis frequency band around the center frequency of the transducer. This analysis band defines the band of frequencies of the power spectra involved in Eq. (3.1). The analysis band ranged from 3.2 to 6.6 MHz in the numerical simulations and from 4.1 to 6.5 MHz in the physical phantom studies. The lower bandwidth was used in the physical phantoms because of low signal-to-noise ratio in the experimentally acquired signals.

3.2.2 Computer simulation

We intended to quantify bias and variance of estimates of the attenuation coefficient due to the distortion caused by nonlinear acoustic propagation. In experiments with physical phantoms, the transducer behaves as a pass-band filter of the backscattered signals. Therefore, observation of nonlinear distortion through 2nd harmonic generation in the backscattered signals is diminished because it is filtered in the passband operation. However, it is illustrative to use computer simulations with settings similar to those of the experiment to observe the 2nd harmonic band generated without the aforementioned filtering effect. Nevertheless, computing the attenuation coefficient by Eq. (3.1) required only the fundamental frequency band around the excitation nominal frequency.

Computer simulated RF data were generated with the k-Wave toolbox [47]. Three numerical phantoms were used in the studies: one sample and two references (high and low attenuating), labelled S′, $\mathrm{R_{HA}}'$, and $\mathrm{R_{LA}}'$ to resemble the names of the physical phantoms (the prime superscript is used

when referring to numerical simulated data) having the same attenuation and nonlinearity parameter as in Table 3.1. Random spatial variations in the density (2% standard deviation) were defined generating media with spatially random impedance values such that backscattered signals mimicking those observed from physical phantoms could be generated. The simulated focused transducer acted as both a source and a receiver with a diameter of 0.5" and a 1" focal length and was configured in a three-dimensional (3D) grid such that a maximum frequency of 12.8 MHz was supported in the three axes using a spatial grid increments of 0.06 mm (this limitation of supported frequencies was set by the available computational resources). Figure 3.1 depicts the source/receiver used to simulate the data. k-Wave allowed the attenuation coefficient to be set with a uniform power law attenuation coefficient across the medium with values from Table 3.1. Likewise, in k-Wave it is possible to set a nonlinearity parameter B/A to include nonlinear distortion and generation of harmonics.

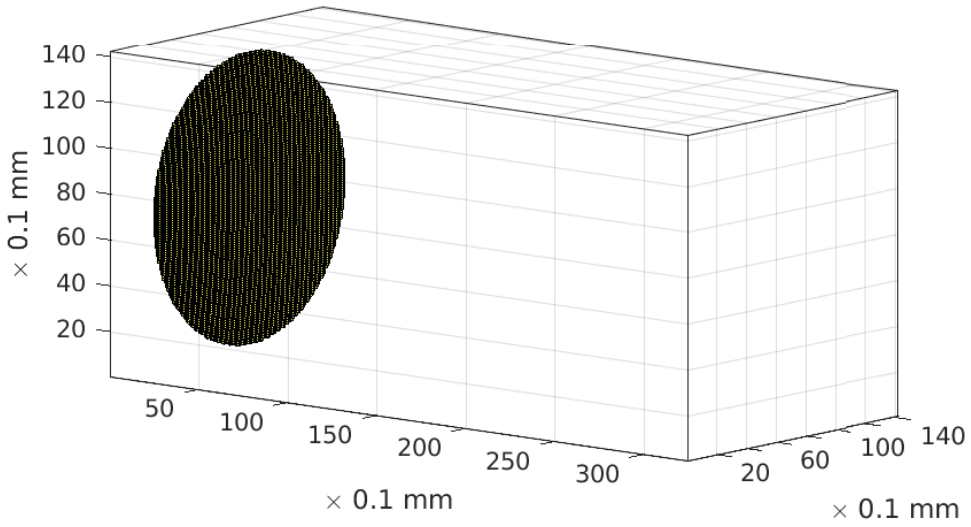

Figure 3.1: Source/sensor in numerical simulations depicted as a spherically focused geometry in 3D discrete media. The focal length 1" is smaller than the largest axial depth.

A limitation of k-Wave is that it cannot set arbitrarily small grid sizes without rapidly exceeding the computational resources, especially when the simulation was in 3D. To validate that our simulations were correctly capturing the nonlinear distortion in the fundamental band we used the Khokhlov-Zabolotskaya-Kuznetzov (KZK) model and its solver by [41] as the gold stan-

Table 3.1: Speed of sound, attenuation coefficient, B/A, glass bead size ranges and concentrations of glass beads in physical phantoms: S (sample), R_{HA} (high attenuating reference), and R_{LA} (low attenuating reference).

	Phantom S	**Phantom R_{HA}**	**Phantom R_{LA}**
Sound speed (m/s)	∼1540	∼1540	∼1540
$\alpha(f)$ (dB/cm)	$0.27f^{1.32}$	$0.7f^{1.1}$	$0.028f^{1.75}$
B/A	6.8	6.9	6.0
Diameters (µm)	75–90	9–43	41 ± 2
Concentration	$5/mm^3$	$800/mm^3$	No info.

dard (because this software can generate several harmonics). We compared KZK waveforms to the waveforms generated in k-Wave. We simulated a forward broadband pulse propagation in a medium with square attenuation dependence on frequency (assumed by KZK model) with lower attenuation than the used phantoms, i.e., more likely to develop nonlinearities. The discrepancy between waveforms at the geometrical focus was less than 3.3% of the peak-to-peak pressure. Therefore, it was assumed that the k-Wave simulations at the chosen grid size correctly predicted the nonlinear behaviors in the phantoms.

A broadband pulse with a 5 MHz center frequency and 60% fractional bandwidth (−6 dB) was used as an input signal. The pulse was intended to mimic the waveform from the physical transducer, which was experimentally measured close to the transducer surface (4 mm from the surface) using a needle hydrophone (Precision Acoustics Ltd., Dorchester, UK). The normalized pressure and frequency components of this input signal are shown in Figure 3.2. At 4 mm from the transducer surface, negligible nonlinear distortion of the pulse had occurred resulting in harmonics that were more than 20 dB below the fundamental frequency. The source was excited using three different source peak pressures: 340, 570, 870 kPa from the values used experimentally; and additionally two source peak pressures used solely in simulations: 1100 and 1330 kPa to assess the effects of nonlinear distortion over a range of pressures that might be encountered in practice. Echoes received at the sensor were recorded for each of the six source pressures. Fifteen independent RF lines for each random media were generated. Power spectra estimated from the independent realizations were ensemble averaged in order to smooth out the power spectra for the SLD method using the full fifteen power spectra for the reference power spectrum and groups of five for the

sample power spectrum in order to obtain three attenuation coefficient slope values per source pressure. Similar to the attenuation estimation used in the physical experiments, the attenuation coefficient of sample S′ was determined using the SLD method in two scenarios: (1) medium R_{HA}' (more attenuating) as the reference phantom and (2) medium R_{LA}' (less attenuating) as the reference phantom. The B/A values for the three simulated media were set to 6.8, 6.9 and 6.0 for numerical phantoms S′, R_{HA}' and R_{LA}', respectively, to match the B/A estimated for the corresponding physical phantoms. For calculation of the power spectra from the backscattered scan lines, the length of the gated windows were set at 20 wavelengths, i.e., roughly 8 pulse lengths axially for both proximal and distal windows.

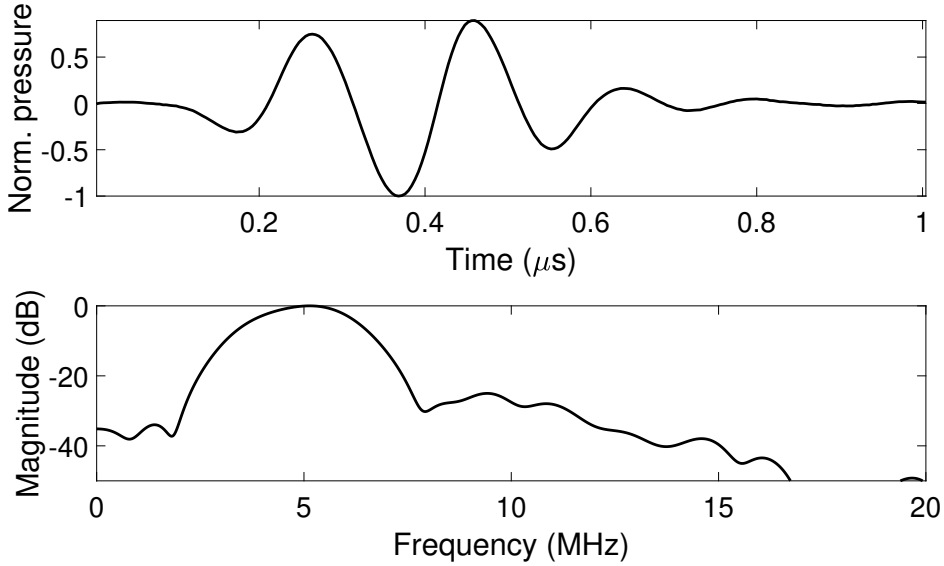

Figure 3.2: Normalized pressure (top) and power spectrum (bottom) of the input excitation source used in the simulations. The time-domain waveform was chosen to mimic the waveform observed in the experiments when measured with a needle hydrophone at 4 mm from the surface of the transducer.

3.2.3 Experimental phantoms

For the physical phantom experiment, three agar-based tissue-mimicking phantoms containing glass bead scatterers were used and labeled S, R_{HA} or R_{LA}. Physical phantoms of these types are often used to assess image quality performance of ultrasonic imaging techniques because the speckle features can be controlled by the glass bead concentration and attenuation

by mixtures of bovine milk, agar, and degassed water. Each phantom had cylindrical shape with 3" diameter and 1.5" height and an agar-based matrix. The physical properties in Table 3.1 of the phantoms S and R_{HA} are described in [38] as phantoms A and B; whereas the properties of phantom R_{LA} is described in the second column of Table 1 in [48].

Sound speeds were calculated using Eq. (4) in [38], i.e., measuring arrival times of received broadband pulses with and without the sample in a water path. Ground truth attenuation coefficients of Table 3.1 were estimated using standard insertion loss methods [49], i.e., immersing the phantoms in a water tank, accounting for mismatches between the speed of sound for water and the phantoms [50] and performing a least-square method to fit the attenuation coefficient to a power law with respect to frequency [51] over the range from 2 MHz to 7 MHz. To reduce the impact of nonlinear effects in determination of the ground truth attenuation coefficients, both sound speed and attenuation were calculated with RF data acquired using a low power level pulser/receiver (5800PR, Panametrics Olympus, USA) in which the second harmonic signals recorded with a needle hydrophone for the water-only path were below 20 dB. The nonlinearity parameter, B/A, was estimated using the through-transmission method by Dong et al. [40]. Using this method, the estimated values of B/A for our phantoms (presented in Table 3.1) were in agreement with results for phantoms of the similar type found in [40]. In order to compare attenuation coefficient slope estimates using the SLD technique against the ground truth estimates, it was necessary to estimate the slope values from the ground truth values of attenuation coefficient in Table 3.1 by fitting a straight line to the function over the analysis frequency band of 4.1 to 6.5 MHz. The ground truth attenuation coefficient slope values for phantoms S, R_{HA}, and R_{LA} were 0.61, 0.91, and 0.17 dB/cm/MHz, respectively. For the simulations, because the analysis frequency range spanned from the 3.2 to 6.6 MHz, the ground truth values were slightly different at 0.59, 0.9, and 0.16 dB/cm/MHz for S′, R_{HA}', and R_{LA}', respectively.

3.2.4 Ultrasonic scanning procedures

The attenuation coefficients were estimated from the phantoms using the SLD method at different source pressure levels to quantify the effects of the nonlinear distortion of the ultrasonic wave propagation on the accuracy of the attenuation coefficient estimates. Each phantom was immersed in a tank filled with degassed water and scanned using a single-element spherically focused transducer (ISR054, NdtXducer LLC, USA) having a 0.5" diameter and 1" focal length (see Figure 3.3). The nominal frequency of the transducer was 5 MHz and was excited with a high-power pulsing apparatus (RAM-5000, Ritec, USA). The input signal applied to the transducer was a 1-cycle sinusoid at 5 MHz. Backscattered RF data were acquired by the same transducer for six excitation levels generated by the pulsing apparatus. The six excitation levels resulted in peak pressures of 340, 450, 570, 690, 780, and 870 kPa measured independently in water by a needle hydrophone at 4 mm from the transducer surface (see Figure 3.2). The pressure levels of the signals from the transducer at each excitation level were also measured at the geometrical focus (see Table 3.2) providing a strong nonlinear distortion as observed in Figure 3.4.

Further power spectral smoothing occurred by averaging power spectra from RF data acquired by moving the transducer in a plane (grid of 14 mm $\times$ 14 mm) parallel to the surface of the transducer with 1 mm steps. This resulted in a backscattered power spectrum estimate from an ensemble average of 225 independent power spectra. The mean and standard deviation were calculated for three estimate values obtained at each excitation level by using a third (75 averaging of the 225 power spectra) of the sample power spectra. Nonlinear distortion of the ultrasound in the phantoms was expected to be less than in water because while the B/A is slightly lower in water than in the phantoms (e.g., B/A of 5 versus 6), the attenuation of water is more than an order of magnitude lower than the phantoms at 5 MHz.

Attenuation coefficient estimates were obtained for the phantom S, which was used as the sample, whereas phantoms R_{HA} and R_{LA} were used independently as references (high attenuating and low attenuating). In the estimation, the distal window was placed just before the focus (centered around 24 mm) and the proximal window 20 wavelengths closer to the transducer, with axial length of data blocks about 20 wavelengths as well. Phantoms

S, R_{HA} and R_{LA} had similar B/A values but different attenuation coefficient values. Reference phantom R_{HA} had higher attenuation than phantom R_{LA} suggesting that nonlinear distortion in the reference was more likely to develop in phantom R_{LA}. Once $\alpha_S(f)$ was obtained following Eq. (3.1), a linear fit was performed to obtain the attenuation coefficient slope (in dB/cm/MHz) and compared with the corresponding ground truth value derived using the $\alpha(f)$ from Table 3.1. Finally the difference in the attenuation slope estimates between the lowest and highest excitation pressure levels was computed as

$$\Delta_{\text{slope}} = \text{slope}_{870\text{kPa}} - \text{slope}_{340\text{kPa}}. \tag{3.2}$$

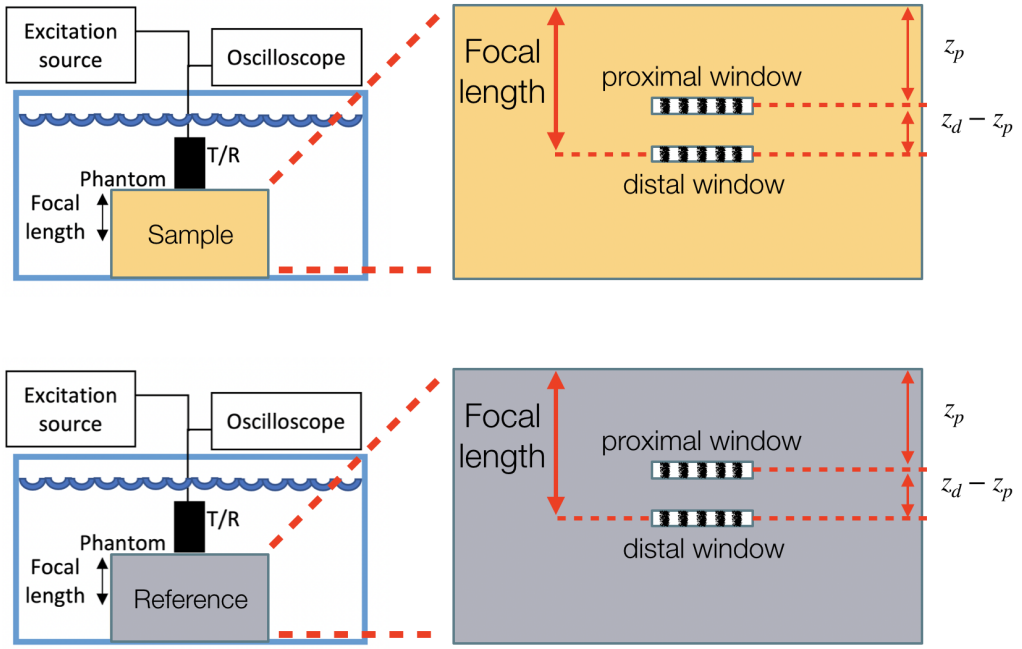

Figure 3.3: (Top) Depiction of the experimental setup when measuring from the sample and (bottom) depiction of the experimental setup when measuring from the reference phantom. Note that the experimental setup was the same between the sample and reference and only the sample was replaced with the reference phantom.

3.3 Results

In this section, we present the power spectra—utilized calculate the attenuation coefficient— and the attenuation coefficient estimates for both data

Table 3.2: Summary of peak positive pressure and peak negative pressure values associated with the settings used in the experiments, measured using a needle hydrophone at the geometrical focus F=1" of the transducer. The MI at the nominal frequency f_0=5 MHz was calculated using $\mathrm{MI} = \mathrm{PNP}\exp\left(-0.0345 f_0 F\right)/\sqrt{f_0}$ and found to be within the FDA regulated limits for diagnostic ultrasound (MI < 1.9).

	Peak positive pressure (MPa)	**Peak negative pressure (MPa)**	**MI**
Excitation level 1	7.57	2.76	0.80
Excitation level 2	8.87	3.33	0.96
Excitation level 3	9.76	3.77	1.09
Excitation level 4	10.53	4.14	1.19
Excitation level 5	11.53	4.42	1.27
Excitation level 6	12.04	4.63	1.34

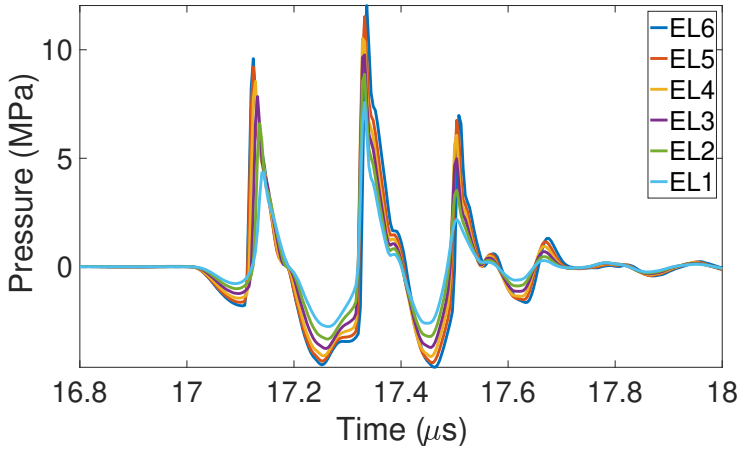

Figure 3.4: Waveforms measured at the geometrical focus of the transducer using a needle hydrophone when exciting the transducer with the six excitation levels (ELs). The nonlinear distortion is observable from the hydrophone measurements that were performed in water.

acquisition cases: computer simulated phantoms, and physical phantoms.

3.3.1 Computer simulation

Figure 3.5 shows the power spectra from the numerical phantoms with proximal and distal windows for each excitation level used. The five different excitation peak pressures set in k-Wave at the source were 340 kPa (blue), 570 kPa (orange), 870 kPa (yellow), 1100 kPa (purple), and 1330 kPa (green). The numerical phantoms were simulated with nonlinearity parameters de-

scribed in the Table 3.1 to mimic the acoustic properties of the physical phantoms.

In Figure 3.5 the 2nd harmonic components, roughly starting at 8 MHz, can be observed because energy is transferred from the fundamental band to higher harmonics. From Figure 3.5, the rate at which energy is transferred from the fundamental to harmonics depends on the source pressure level used and the acoustic properties of the phantoms such as the value of B/A and attenuation coefficient. Figure 3.6 and 3.7 provide estimates of the attenuation coefficient slopes for phantom S$'$ when using phantom $\mathrm{R_{HA}}'$ (Figure 3.6a) as a reference and phantom $\mathrm{R_{LA}}'$ (Figure 3.7a) as a reference. For example, when the more attenuating numerical phantom $\mathrm{R_{HA}}'$ was used as a reference, the attenuation coefficient slope of the sample varied from 0.66 $\pm$ 0.12 dB/cm/MHz for the smaller source pressure to 0.86 $\pm$ 0.13 dB/cm/MHz for the largest source pressure. The increase in the estimate of attenuation slope from the source pressure level 340 kPa to the source pressure level 870 kPa was Δ_{slope}=0.083 dB/cm/MHz. On the other hand, when the less attenuating numerical phantom $\mathrm{R_{LA}}'$ was used as a reference, the attenuation coefficient slope of the sample varied from 0.64 $\pm$ 0.13 dB/cm/MHz for the smaller source pressure to 0.43 $\pm$ 0.13 dB/cm/MHz for the largest source pressure. The decrease in the estimate of the attenuation slope from the source pressure level 340 kPa to the source pressure level 870 kPa was Δ_{slope}=$-$0.118 dB/cm/MHz. Using either the high or low attenuating phantoms, at the lowest source pressure level the ground truth value 0.61 dB/cm/MHz remained within one standard deviation of the estimated mean value but larger bias is observed at the largest source pressure level.

The deviation in the estimates of the attenuation coefficient slope with increasing pressure indicated that nonlinear distortion could introduce changes in attenuation coefficient slope estimates with increasing source pressure. Furthermore, due to the attenuation of the different simulated phantoms, nonlinear distortion of power spectra from reference phantom $\mathrm{R_{HA}}'$ was slightly lower than for phantom S$'$, resulting in monotonically increasing estimates of attenuation coefficient slope and vice versa when using phantom $\mathrm{R_{LA}}'$ as the reference.

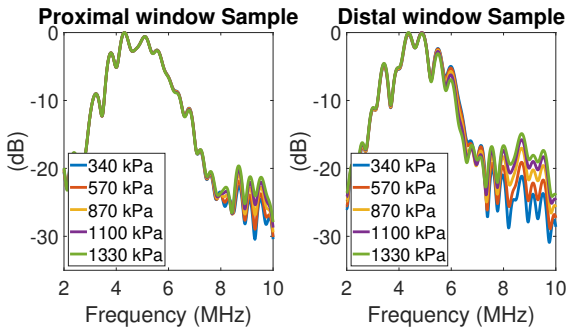

(a) Numerical phantom S′: $B/A = 6.8$ and $\alpha(f) = 0.27 f^{1.32}\,\frac{\text{dB}}{\text{cm}}$

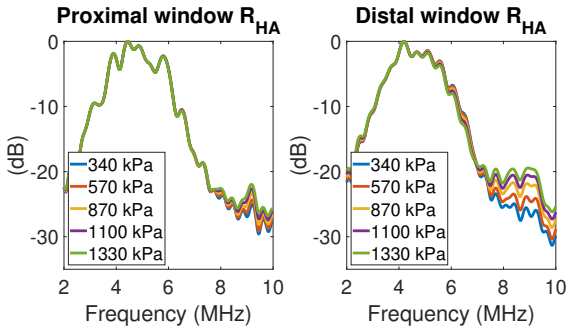

(b) Numerical phantom R_{HA}': $B/A = 6.9$ and $\alpha(f) = 0.7 f^{1.1}\,\frac{\text{dB}}{\text{cm}}$

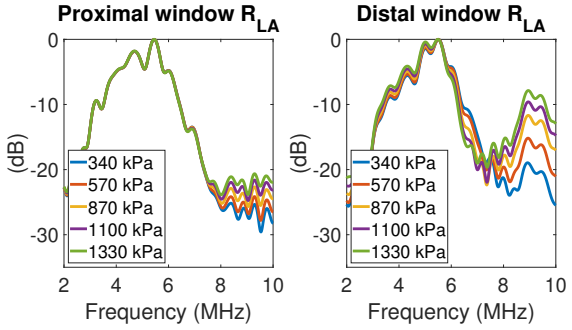

(c) Numerical phantom R_{LA}': $B/A = 6$ and $\alpha(f) = 0.028 f^{1.75}\,\frac{\text{dB}}{\text{cm}}$

Figure 3.5: Power spectra from gated proximal and distal windows using five increasing source pressures in the numerical phantoms S′ (top), R_{HA}' (middle), and R_{LA}' (bottom). The proximal window was located before the geometrical focus and the distal window was located close to the geometrical focus. In computer simulations it is clear that larger levels of 2nd harmonic are generated at the distal windows. Moreover, the low attenuating reference phantom (R_{LA}') power spectra had larger 2nd harmonic generation for the larger acoustic pressures than S′ and R_{HA}'.

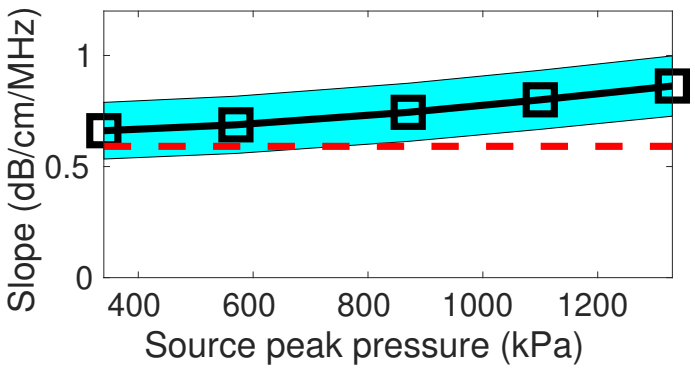

(a) Numerical phantom slope vs. source pressure

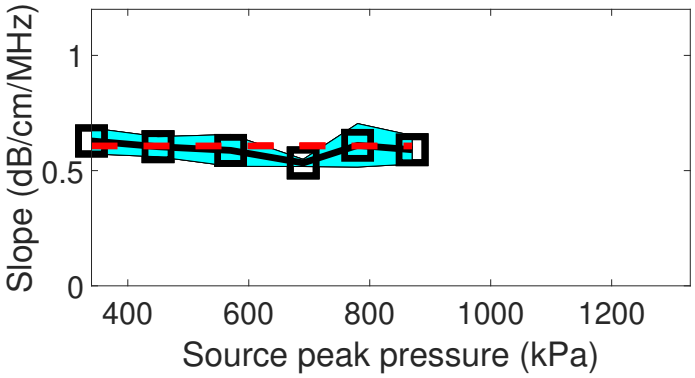

(b) Physical phantom slope vs. source pressure

Figure 3.6: Mean (square markers) of attenuation coefficient slope estimates of medium S for the numerical phantom (top) and physical phantom (bottom) when the reference was the high attenuating reference medium R_{HA}. Shadowed area corresponds to the standard deviation (one above and one below) of slope estimated mean values. The dashed red line was the ground truth slope.

3.3.2 Experimental phantoms

The power spectra from proximal and distal regions used to estimate attenuation coefficient slope in the physical phantoms are presented in Figure 3.8. In experiments, the 2nd harmonic was mostly filtered out by the transducer. Similar to the power spectra in numerical phantoms, the fundamental band shifted to lower frequency especially at the distal window (closer to focus) with this shift more pronounced in the low attenuating phantom R_{LA}, Figure 3.8(c), as pressure levels increased.

The attenuation coefficient slope values were estimated for phantom S and are shown in Figures 3.6(b) and 3.7(b) when using phantoms R_{HA} and R_{LA} as references, respectively. Experimentally, it was observed that more

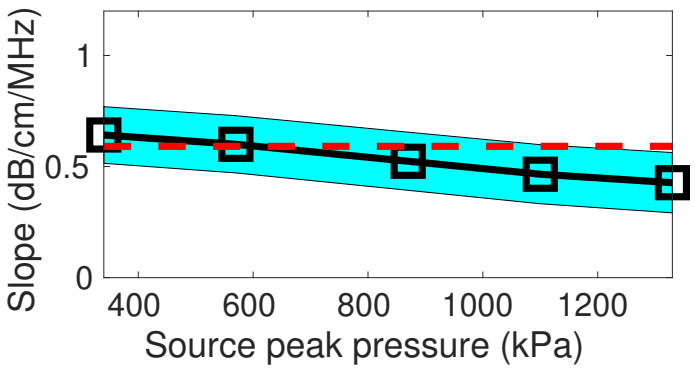

(a) Numerical phantom slope vs. source pressure

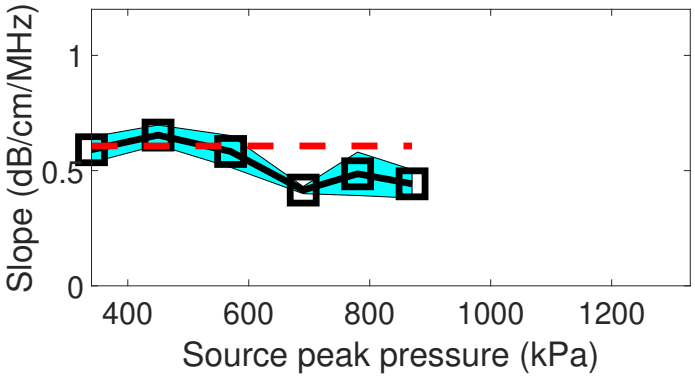

(b) Physical phantom slope vs. source pressure

Figure 3.7: Mean (square markers) of attenuation coefficient slope estimates of medium S for the numerical phantom (top) and physical phantom (bottom) when the reference was the low attenuating reference medium R_{LA}. Shadowed area corresponds to the standard deviation (one above and one below) of slope estimated mean values. The dashed red line was the ground truth slope.

consistent attenuation coefficient estimates were obtained when using references with higher attenuation coefficients, i.e., phantoms S and R_{HA}, in which case $\Delta_{slope} = -0.038$ dB/cm/MHz; whereas more inconsistency was observed when using phantom R_{LA} as the reference, i.e., $\Delta_{slope} = -0.148$ dB/cm/MHz. In the latter case, the ground truth value was outside of one standard deviation of the estimated slopes when using the largest source pressure level. However, unlike in the computer simulated phantoms, the values of the attenuation slopes did not change monotonically versus excitation level and the standard deviation were more variable across the excitation levels, which might be explained by lower signal-to-noise ratio of experimental backscattered data.

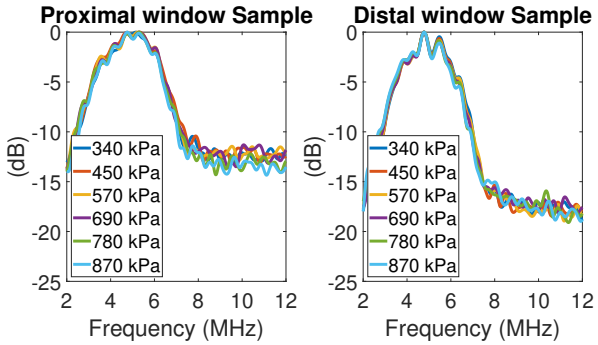

(a) Physical phantom S: $B/A = 6.8$ and $\alpha(f) = 0.27 f^{1.32} \frac{\text{dB}}{\text{cm}}$

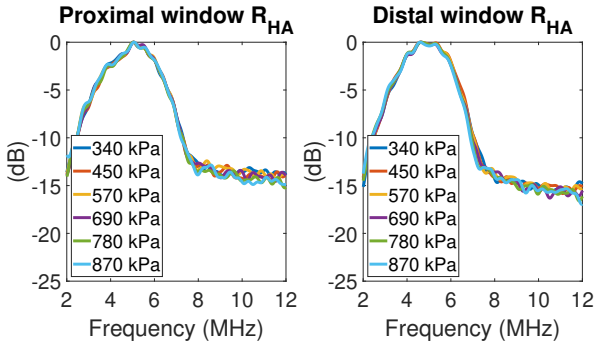

(b) Physical phantom R_{HA}: $B/A = 6.9$ and $\alpha(f) = 0.7 f^{1.1} \frac{\text{dB}}{\text{cm}}$

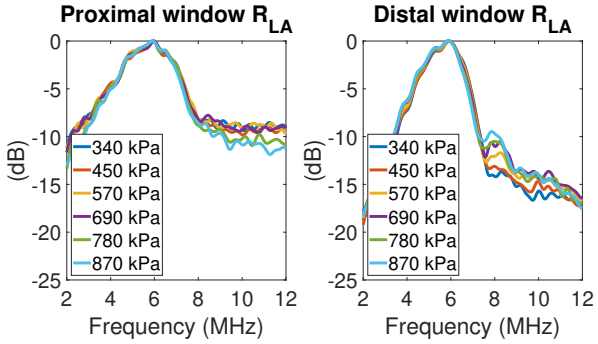

(c) Physical phantom R_{LA}: $B/A = 6.0$ and $\alpha(f) = 0.028 f^{1.75} \frac{\text{dB}}{\text{cm}}$

Figure 3.8: Power spectra from gated proximal and distal windows using six increasing source pressures in the physical phantoms S (top), R_{HA} (middle), and R_{LA} (bottom). The proximal window was located 1 cm before the geometrical focus and the distal window was located just after the geometrical focus. No 2nd harmonic was clearly observable unlike the numerical simulations (Figure 3.5) due to the filtering effect of the transducer.

3.4 Discussion

In the present chapter, we evaluated the SLD method for attenuation coefficient estimation when using increasingly higher acoustic pressures to assess if nonlinear distortion of ultrasound due to the nonlinearity of the medium would introduce biases in the attenuation coefficient estimates. We confirmed in numerical simulations, that 2nd harmonic generation was likely to occur depending on several factors. The cases associated with the highest 2nd harmonic generation included when larger input acoustic pressures at the source were applied, when the location of the gated window was closer to the geometrical focus, i.e., where larger pressures are expected due to focusing, and when less attenuating media were used that led to more rapid develop of nonlinear distortion.

The presence of nonlinear distortion in lossy media can be quantified through the Gol'dberg number, which is proportional to the ratio of the nonlinearity coefficient and attenuation coefficient. In computer simulations we confirmed that both the nonlinearity parameter and the acoustic attenuation of the medium affect the generation of the 2nd harmonic. Moreover, the power spectra generated in the numerical simulations were consistent with the definition of Gol'dberg number. Therefore, acoustic nonlinearities result in energy in the fundamental band being transferred to higher harmonics (2nd harmonic presented in the numerical simulation). Thus, spectral methods for attenuation coefficient slope estimation that use the fundamental band produce biased attenuation coefficient estimates when non-negligible energy is transferred out of the fundamental band.

From the numerical simulations and experiments with physical phantoms we observed that attenuation coefficient estimates varied with different source pressures. These changes are associated with the nonlinear distortion of ultrasound in the sample and reference, which is observed in the power spectra at the fundamental band. Typically, distortions were observed to change more in the higher frequencies of the fundamental band than in the lower frequencies. This can be explained by the shock distance $l = \frac{1}{\beta k M}$ that suggests that generation of harmonics will occur over a shorter distance for higher frequencies components. In other words, higher frequencies are more rapidly transferred to higher harmonics resulting in a change in the slope over distance in the fundamental band of the backscattered power spectra in

all cases. This distortion of the fundamental band is further enhanced in less attenuating media where the energy in the higher harmonics is not attenuated out as quickly resulting in more nonlinear distortion of the propagating pulse.

Although the Gol'dberg number is commonly defined for mono-frequency plane wave rather than a focused transducer, we utilized the Gol'dberg number to predict the presence of nonlinear distortion of the ultrasound. For the transducer geometry used in this chapter, the Focal gain was G=$\frac{\pi a^2}{\lambda F} \approx 16.2$ (a is the radius of the source, F=1" and λ the wavelength corresponding to the nominal frequency 5 MHz); therefore, the maximum Gol'dberg numbers, considering linear gain peak pressures at the focus, were between $\Gamma_S \in [8, 20.5]$, $\Gamma_{R_{\mathrm{HA}}} \in [4.5, 11.4]$, and $\Gamma_{R_{\mathrm{LA}}} \in [35.2, 90]$, over the source pressures range from 340–870 kPa. Therefore, a stronger 2nd harmonic development in the lower attenuating numerical phantom $\mathrm{R_{LA}}$ was expected from the Gol'dberg number calculation and larger nonlinear distortion effects were predicted when using this phantom. It should be noted that because of nonlinear propagation effects, the actual linear focal gains, G, were not attained, i.e., positive peak pressure gains were larger than G whereas negative peak pressure gains were smaller than G, [52].

Similar results were observed when quantifying nonlinear distortion of ultrasound on the estimate of the BSC in Chapter 2 and [46]. The BSC estimation process was analyzed using the reference phantom method and the traditional planar reflector technique in a water medium. The findings were that a spectral-based method that used a nonlinear medium with low attenuation (i.e., water) produced large biases in the BSC estimates. In that paper, the nonlinear distortion of ultrasound resulted in changes in the magnitude and slope of the BSC because the references had different levels of nonlinear distortion. Specifically, using the water path for the reference (in the denominator of Eq. (2.1)) resulted in much larger nonlinear distortion at high pressures when compared to using an attenuating reference phantom. Similar to attenuation coefficient estimation with the SLD, in the BSC estimation, the sample and reference power spectra are used. Similarly, when using only a pair of power spectra (calibration / sample), the calibration signal is in the numerator for AC estimation (see Sec. (2) in D'hooge et al. [22]), hence an overestimation of the attenuation can be predicted.

However, for the attenuation approach used in this chapter, the analysis

was more complex, because up to four power spectra (see Eq. (3.1)) are involved in the estimation of the attenuation coefficient. It can be thought as three calibration signals involved (from the reference phantom proximal and distal windows and one from the sample phantom proximal window). One of the reasons for locating the distal window closer to the geometrical focus was to make the nonlinear distortion much larger than the nonlinear distortion in the proximal window located out of the focal region. Therefore, the attenuation coefficient estimates depend mainly on $S(f, z_d)$ and $S_R(f, z_d)$. If the attenuation values of the sample and reference are known, we can predict whether the fundamental band will be distorted more in the sample or reference and predict a positive or negative biases in the attenuation coefficient estimates. For example, when the reference had lower attenuation than the sample, an apparent decrease in attenuation coefficients was observed. The opposite (increasing attenuation coefficients at higher excitation levels) occurred when the reference phantom had higher attenuation than the sample.

It should be also noted that the separation between proximal and distal windows was 20 wavelengths. Cumulative nonlinear distortion from the proximal window to distal window is further enhanced by the selected location of the distal window much closer to the focal region. An alternative to minimize such nonlinear distortion would be take both windows outside the focal region but typically in practice, the ROI to be diagnosed is where the operator tries to position the focal length of the beam to improve the SNR. Another alternative could be to decrease the axial separation of the the proximal and distal windows. However, to reduce this separation, the data blocks would need to be even smaller as well. The current ROI (joining proximal and distal windows) is 40 wavelengths length which corresponds roughly to 16 pulse lengths. Errors from small axial lengths has been analyzed by Labyed and Bigelow [45] and, for example, halving the ROI to 8 wavelengths would only increase the AC error bias (not due to nonlinear distortion but due the stochastic nature of scattering).

From the results in the numerical phantoms, the attenuation coefficient slope values obtained using the smallest pressure level and the largest pressure level had a mismatch that changed depending on the reference phantom used. This mismatch, Δ_{slope}, computed as in Eq. (3.2) can be correlated to the Gol'dberg number of the phantoms involved in the estimation (sample and reference) by comparing the results to the ratio of Gol'dberg number:

$\frac{\Gamma_{\text{Sample}}}{\Gamma_{\text{Reference}}}$. From the acoustic properties of the phantoms described in Table 3.1, at f_0=5 MHz, Gol'dberg number ratios for the different phantoms were: $\frac{\Gamma_{\text{S}'}}{\Gamma_{\text{R}_{\text{LA}}'}} = 0.23$ and $\frac{\Gamma_{\text{R}_{\text{HA}}'}}{\Gamma_{\text{S}'}} = 0.56$. In addition, we calculated the attenuation coefficient slope of phantom R'$_{\text{HA}}$ using the reference R'$_{\text{LA}}$ resulting in an attenuation slope mismatch of $\Delta_{\text{slope}} = -0.20$ dB/cm/MHz with a Gol'dberg ratio of $\frac{\Gamma_{\text{R'}_{\text{HA}}}}{\Gamma_{\text{R'}_{\text{LA}}}} = 0.127$. Figure 3.9 shows the attenuation coefficient slope values at different pressure levels using the aforementioned pairs of samples/references where the increase or decrease of the Δ_{slope} depended on the ratio of Gol'dberg numbers.

Figure 3.10(a) shows a plot of values of Δ_{slope} versus Gol'dberg number while 3.10(b) shows a plot of the Δ_{slope} values versus the log of the Gol'dberg number ratios. Computing the coefficient of determination between Δ_{slope} vs $\log_{10} \frac{\Gamma_{\text{Sample}}}{\Gamma_{\text{Reference}}}$ results in $R^2 = 0.979$. Similar calculation with the physical phantoms resulted in $R^2 = 0.734$. Empirically, one can observe that the mismatch of attenuation coefficient slope estimates from the different excitation levels due to acoustic nonlinearity is highly correlated to $\log_{10} \frac{\Gamma_{\text{Sample}}}{\Gamma_{\text{Reference}}}$.

3.5 Conclusion

The results suggest that attenuation coefficient estimation in pulse-echo mode using established methods, such as the SLD, can be biased due to the inherent acoustic properties of the sample medium and reference. The mismatch between the estimated attenuation slope values from the true value during the ultrasonic acquisition of backscattered signals will increase when larger pressure levels are used. Moreover, the observed biases of attenuation coefficient slope estimates in both simulation and physical nonlinear media were more likely to occur in low attenuating media. Therefore, tradeoffs between the attenuation of the reference material, B/A and the need for strong SNR should be considered when using methods like the SLD to estimate attenuation coefficients. After observing the pattern of increasing or decreasing attenuation coefficient slope estimates when using larger pressure levels, it was concluded that the attenuation values of the sample and reference should be close in order to reduce the effects of nonlinearity on the estimates and, therefore, the Gol'dberg number ratio between the sample and reference should be close to unity to optimally mitigate nonlinear effects on attenuation slope estimation.

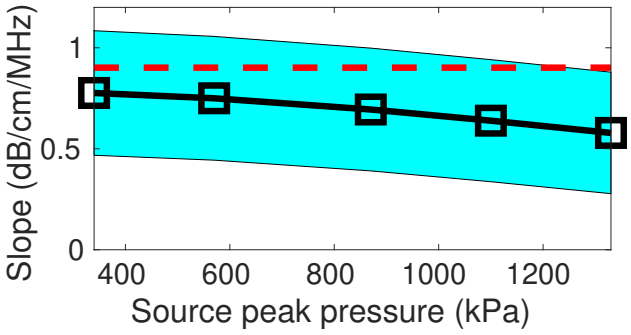

(a) Sample: R_{HA}. Reference: S

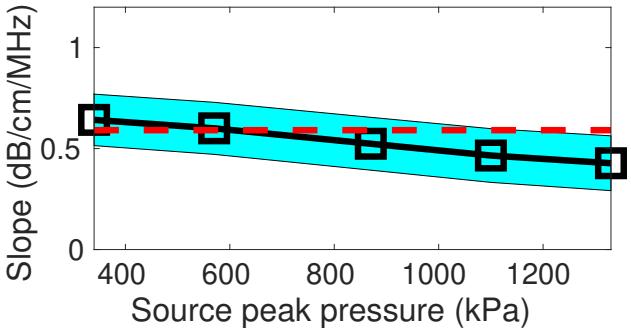

(b) Sample: S. Reference: R_{LA}

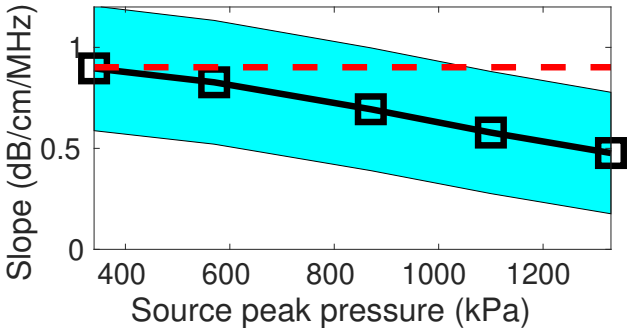

(c) Sample: R_{HA}. Reference: R_{LA}

Figure 3.9: Attenuation coefficient slope values versus source pressure level for three pairs of sample and reference. Large Gol'dberg ratios are correlated with increasing deviation of estimated attenuation slopes from baseline when using larger pressures.

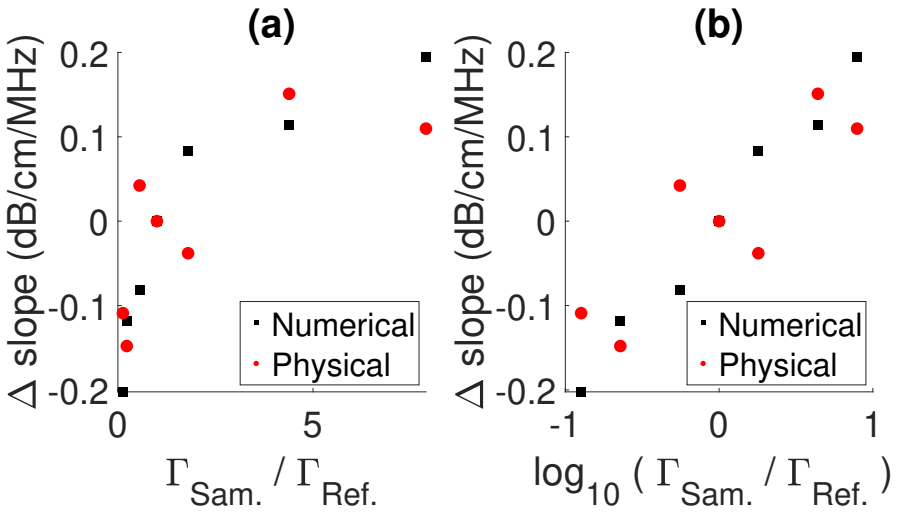

Figure 3.10: Mismatch of attenuation coefficient slope at low (340 kPa) and high (870 kPa) source pressures. Coefficient of determination was 0.754 vs $\frac{\Gamma_{\text{Sample}}}{\Gamma_{\text{Reference}}}$, and 0.979 vs $\log_{10}\left(\frac{\Gamma_{\text{Sample}}}{\Gamma_{\text{Reference}}}\right)$ in numerical results. For the experimental data, the coefficient of determination was 0.564 vs $\frac{\Gamma_{\text{Sample}}}{\Gamma_{\text{Reference}}}$, and 0.734 vs $\log_{10}\left(\frac{\Gamma_{\text{Sample}}}{\Gamma_{\text{Reference}}}\right)$.

CHAPTER 4

IN SITU CALIBRATION OF THE BACKSCATTER COEFFICIENT IN ACOUSTIC NONLINEAR REGIME

4.1 Introduction

The goal of quantitative ultrasound (QUS) is to complement traditional B-mode ultrasonic imaging by providing operator-independent and system-independent quantitative parameters related to tissue state. In particular, spectral-based QUS techniques have been evaluated for tissue characterization, with recent examples including studies in breast [53], calcaneus bone [54], and liver [55], among others [4, 56]. One advantage of QUS over traditional B-mode imaging is the potential to make the assessment independent of the acquisition system. This is possible because an additional calibrated signal from well-characterized media is collected. For example, the BSC can be made system independent by using calibration signals from a planar reflective surface with known coefficient of reflectivity [16] or from a reference phantom [17].

However, spectral-based QUS parameters can be degraded by acoustic nonlinearity. In [46] and Chapter 2, we demonstrated that BSC estimates were observed to degrade more because of acoustic nonlinear distortion using a planar reflector calibration. The reason for this distortion is that the path between the transducer and the planar reflector is water, which has higher Gol'dberg number [36, p. 483] (mainly due to the low attenuation coefficient of water), than a reference phantom. In [57] and Chapter 3, another spectral-based QUS parameter, the attenuation coefficient, had a similar pattern. Accuracy of attenuation coefficient estimates degraded when using higher power levels. Moreover, in Chapter 3, it was observed that biases introduced by acoustic nonlinearity in the attenuation coefficient estimates were correlated with the ratio of the Gol'dberg numbers from sample and reference phantoms. From that finding it could be inferred that QUS esti-

mates would be less affected by acoustic nonlinear distortion when Gol'dberg numbers of the interrogated medium and the reference material were close to each other. Ideally, finding a calibration from within the sample to be interrogated would allow better accounting for acoustic nonlinear distortion because the calibration signal would undergo the same distortion as signals from the sample.

Radiological markers or clips are an essential diagnostic and surgical tool [58]. For example, patients with breast cancer undergoing neoadjuvant chemotherapy have clips placed in the tumors to improve preoperative localization [59]. Radiological clips made of titanium are widely used, are compatible with MRI, and have proven safe for use in human patients [60]. These clips come in many shapes and sizes and are visible with both X-ray and ultrasound. The clips provide large ultrasonic scattering signals because they are made of titanium or gold, which have large impedance mismatch with tissue. Inspired by the use of radiological clips, in [61], another source of BSC distortion, i.e., transmission losses in the propagation path between ultrasonic transducer and the ROI, was compensated using an *in situ* calibration target. In that work, the reference phantom method resulted in less accurate BSC estimates because the reference phantom could not account for the possible transmission losses that occur, e.g, in clinical scenarios when layers of skin, muscle, or fat are in between the transducer and the ROI in an organ.

Therefore, we hypothesize that the *in situ* calibration approach could also be used to compensate acoustic nonlinear distortion effects in the estimation of BSCs. The *in situ* calibration target could provide a reference within the medium being interrogated and the cumulative nonlinear distortion up to the depth of the ROI would already be contained in the *in situ* calibration target signal. For this purpose, we focused our attention on how the power spectra from samples changed versus increasing ultrasonic power levels when the calibration spectra came from an *in situ* calibration target located at the same depth as the sample spectra. We then compared these results to results using a calibration spectra from an external reference phantom from a region located at the same depth. To acquire good BSC estimates requires good SNR, which can be achieved by increasing the output ultrasonic power. The objective was to determine if the *in situ* calibration approach provided a more robust BSC estimation in the presence of nonlinear distortion as the ultrasonic output power increased.

4.2 Methods

In this section, we describe the BSC estimation methods using a calibration signal and the metric used for comparison of the BSC estimation strategies—defined as the mismatch of the BSC frequency dependence. In addition, more detail of the selection of the *in situ* target is presented, and finally, the data acquisition procedure from computer simulated phantoms, *ex vivo*, and *in vivo* is detailed.

4.2.1 BSC estimation methods

The reference phantom method used as the baseline estimation method for BSC and the proposed *in situ* calibration approach are derived in this section.

BSC estimation using a reference phantom

The power spectrum, *S(f,z)*, estimated from ultrasonic backscattered signals from an interrogated ROI located at depth z is a function of frequency (f) and the result of several effects: the BSC of the ROI, $\sigma(f,z)$, the total attenuation up to the ROI, *A(f,z)*, the acoustic-electric and electric-acoustic response of the system acquisition, *V(f)*, and the diffraction effects $D(f,z)$,

$$S(f,z) = V(f)\sigma(f,z)A(f,z)D(f,z). \tag{4.1}$$

In the reference phantom method both *D(f,z)* and *V(f)* can be compensated by collecting the power spectrum of a well-characterized phantom. The BSC is thus

$$\sigma(f) = \sigma_{\text{ref}}(f)\frac{S(f,z)}{S_{\text{ref}}(f,z)}\frac{A_{\text{ref}}(f,z)}{A(f,z)}, \tag{4.2}$$

where the subscript 'ref' stands for reference. Both $\sigma_{\text{ref}}(f)$ and $A_{\text{ref}}(f,z)$ are assumed to be known and $A(f,z)$ can be estimated with attenuation estimation methods like the spectral log difference or the regularized spectral log difference [62]. If a higher power (HP) were used during ultrasonic acquisition the power spectrum from the ROI can be written as

$$S_{\text{HP}}(f,z) = G(f)V(f)\sigma_{\text{HP}}(f,z)A(f,z)D(f,z), \tag{4.3}$$

where *G(f)* is the gain function at the source for the HP settings with respect to the baseline settings. Then, using the reference phantom approach, the BSC at the HP level would be

$$\sigma_{\mathrm{HP}}(f) = \sigma_{\mathrm{ref}}(f)\frac{S_{\mathrm{HP}}(f,z)}{S_{\mathrm{ref,HP}}(f,z)}\frac{A_{\mathrm{ref}}(f,z)}{A(f,z)}. \tag{4.4}$$

However, due to acoustic nonlinear distortion of the power spectra, $\sigma_{\mathrm{HP}}(f)$ might differ from the quasi-linear estimate $\sigma(f)$. Dividing (4.4) by (4.2), we get the error of the BSC estimates, $e_{\mathrm{ref}}(f,z)$, due to nonlinear distortion in the reference phantom approach

$$e_{\mathrm{ref}}(f,z) = \frac{\sigma_{\mathrm{HP}}(f,z)}{\sigma(f,z)} = \left(\frac{S_{\mathrm{HP}}(f,z)}{S(f,z)}\right) \Big/ \left(\frac{S_{\text{ref-HP}}(f)}{S_{\mathrm{ref}}(f)}\right). \tag{4.5}$$

BSC estimation with calibration *in situ*

Using an *in situ* target for calibration, e.g., a well characterized tissue-compatible bead, embedded within the sample in a location as close as possible to the ROI and at the same depth, the power spectrum from the echoes that arrive from the location of the bead can be written as

$$S_{\mathrm{bead}}(f,z) = V(f)\sigma_{\mathrm{bead}}(f,z)A(f,z)D(f,z). \tag{4.6}$$

Following a similar procedure, the sample BSC could be computed as

$$\sigma(f,z) = \sigma_{\mathrm{bead}}(f,z)\frac{S(f,z)}{S_{\mathrm{bead}}(f,z)}, \tag{4.7}$$

and unlike Eq. (4.2), the BSC estimation does not involve an extra computation of total attenuation because both $S(f,z)$ and $S_{\mathrm{bead}}(f,z)$ are expected to undergo similar total attenuation because both the signals from the bead and the signals from the ROI propagated through approximately the same media. At the HP acquisition settings, the BSC is

$$\sigma_{\mathrm{HP}}(f,z) = \sigma_{\mathrm{bead}}(f,z)\frac{S_{\mathrm{HP}}(f,z)}{S_{\text{bead-HP}}(f,z)}. \tag{4.8}$$

Then, the error in BSC, $e_{\mathrm{bead}}(f,z)$, estimated at the HP settings using the

in situ calibration approach can be estimated by

$$e_{\text{bead}}(f,z) = \frac{\sigma_{\text{HP}}(f,z)}{\sigma(f,z)} = \left(\frac{S_{\text{HP}}(f,z)}{S(f,z)}\right) \Big/ \left(\frac{S_{\text{bead-HP}}(f)}{S_{\text{bead}}(f)}\right). \tag{4.9}$$

Discrepancy of BSC frequency dependence

If the increment of power level were small, i.e., only quasi-linear regime

$$\frac{S_{\text{HP}}(f,z)}{S(f,z)} \approx \frac{S_{\text{ref-HP}}(f)}{S_{\text{ref}}(f)} \approx \frac{S_{\text{bead-HP}}(f)}{S_{\text{bead}}(f)}, \tag{4.10}$$

which leads to $e_{\text{ref}}(f,z) \approx e_{\text{bead}}(f,z) \approx 1$, almost no error in the BSC estimates from acoustic nonlinear distortion would occur either using a reference phantom calibration or the *in situ* calibration approach. However, when the increment of power level creates acoustic nonlinear distortion, the BSC estimated at the HP level can vary from the BSC calculated at the baseline power level. Furthermore, other QUS parameters derived from the BSC could be distorted as well. For example, the BSC is often modeled as a power law with respect to frequency. In particular, the exponent n of the power law function of the BSC,

$$\sigma(f,z) = bf^n, \tag{4.11}$$

might be incorrectly estimated at the HP level where

$$\sigma_{\text{HP}}(f,z) = b_{\text{HP}} f^{n_{\text{HP}}}, \tag{4.12}$$

and the error in the estimate can be quantified by $|n_{\text{HP}} - n|$. The discrepancy observed from acoustic nonlinear distortion can be computed as well from the power law function of their respective error functions, $e_{\text{ref}}(f,z)$ or $e_{\text{bead}}(f,z)$, versus frequency, in (4.5) and (4.9), respectively. A first-order approximation of the Taylor series expansion of the error results in

$$\log\left(e(f,z)\right) = \log\left(\frac{b}{b_{\text{HP}}}\right) + (n_{\text{HP}} - n)(f_0) + \frac{n_{\text{HP}} - n}{f_0} f, \tag{4.13}$$

where f_0 is the midpoint frequency of the analysis bandwidth. Therefore, the value of $|n_{\text{HP}} - n|$ can be estimated as the slope of $\log\left(e(f,z)\right)$ vs. f, scaled by f_0.

4.2.2 Bead selection

Marker clips in sonography-guided surgery are produced in many shapes from bio-compatible materials. The median size of radiological clips utilized in guided ultrasonography is about 2 mm [63]. Hence, the experimental part of the current chapter utilized a 2 mm diameter spherical titanium bead. Titanium (Ti) is known to be a bio-compatible element. A spherical shape is chosen because the ultrasonic backscatter is the same no matter the orientation of the bead with the transducer.

4.2.3 Computer simulations

Before experiments, computer simulation of beads embedded in media were generated using the k-Wave package [47]. Pulse-echo acquisition with a linear array was performed in a 3D discrete medium (speed of sound: 1540 m/s, density: 1000 $\pm$ 20 kg/m^3) to generate 128 RF lines. Four simulated 2 mm diameter beads, with density of 6000 kg/m^3, were placed in the medium at different depths. The ultrasonic elements in the medium used for transmit and receive were excited with a 5 MHz Gaussian pulse of 60% bandwidth. In the simulation, the medium was set with attenuation coefficient of 0.5 dB/cm/MHz and nonlinearity parameter, B/A, of 6.6. Beads were located at several depths (as shown in Figure 4.1(a)). Only the first echo of the bead was utilized rather than echoes from multiple reverberations. Changes in the power spectra of the echoes coming from the beads and coming from regions close to the bead depths, produced by four input pressure levels: baseline (100 kPa) and successive increments (200, 500, and 1000 kPa), were calculated. For the reference phantom approach, an additional 128 RF lines were simulated using the same ultrasonic settings from uniform reference phantoms having higher attenuation (0.9 dB/cm/MHz) or lower attenuation (0.1 dB/cm/MHz), shown in Figure 4.1(b) and 4.1(c), respectively. The distinct attenuation coefficient in nonlinear media (despite setting all media with the same B/A=6) causes different degree of acoustic nonlinear distortion in each medium depending on the input pressure. Data blocks were outlined from the B-mode images (see Figure 4.1) and a power spectrum was calculated for each data block by averaging the individual power spectra from scan lines in the data blocks. The power spectrum

from ultrasonic backscatter from the bead was calculated from a gated region covering only the first echo (approximately 6 wavelengths long) and laterally from the scan lines that captured the backscatter from the bead up to amplitudes no smaller than 6 dB below the local maximum. The power spectrum of the sample comes from a gated region at the same depth as the bead, depicted for example by the red box in Figure 4.1(a), which is approximately 6 wavelengths axially and approximately 15 wavelengths laterally. The power spectra from reference phantoms assume the same depth as in the sample but all lateral lines are available for averaging as depicted with the red boxes in Figure 4.1(b) and 4.1(c).

The error in the estimate of BSC frequency dependence due to nonlinear distortion was calculated using (4.13) with the error functions given by (4.5) and (4.9) when using the reference phantom approach and the *in situ* calibration approach. The analysis bandwidth had a frequency range from 4 to 8 MHz. Four bead locations were used so that the exponent estimation error was assessed versus depth of the bead location.

4.2.4 Experimental validation

The errors in the estimates of the BSC frequency dependence due to nonlinear distortion were also assessed experimentally using a physical phantom sample and a tumor *in vivo* from a rabbit model.

Phantom sample

A sample phantom was prepared using a mixture of 400 mL deionized/degassed water, 80 g of gelatin (J.T. Baker, Phillipsburg, NJ), and 12 g of graphite powder (John Deere, Moline, IL). Its speed of sound and attenuation coefficient were estimated to be 1541.5 m/s and $\alpha_{\text{sample}}(f) = 0.33f^{1.17}$ dB/cm, respectively (estimated with insertion loss techniques). A 2 mm diameter titanium spherical bead (BalTec, Los Angeles, CA) was embedded in the sample during phantom preparation and before the gelatin congealed, such that the bead ended up at a depth of around 21 mm. In addition to the *in situ* calibration, the BSC estimation was also performed using two different agar-based reference phantoms having uniformly spatially distributed glass bead scatterers and similar sound speed as the sample (around 1540 m/s).

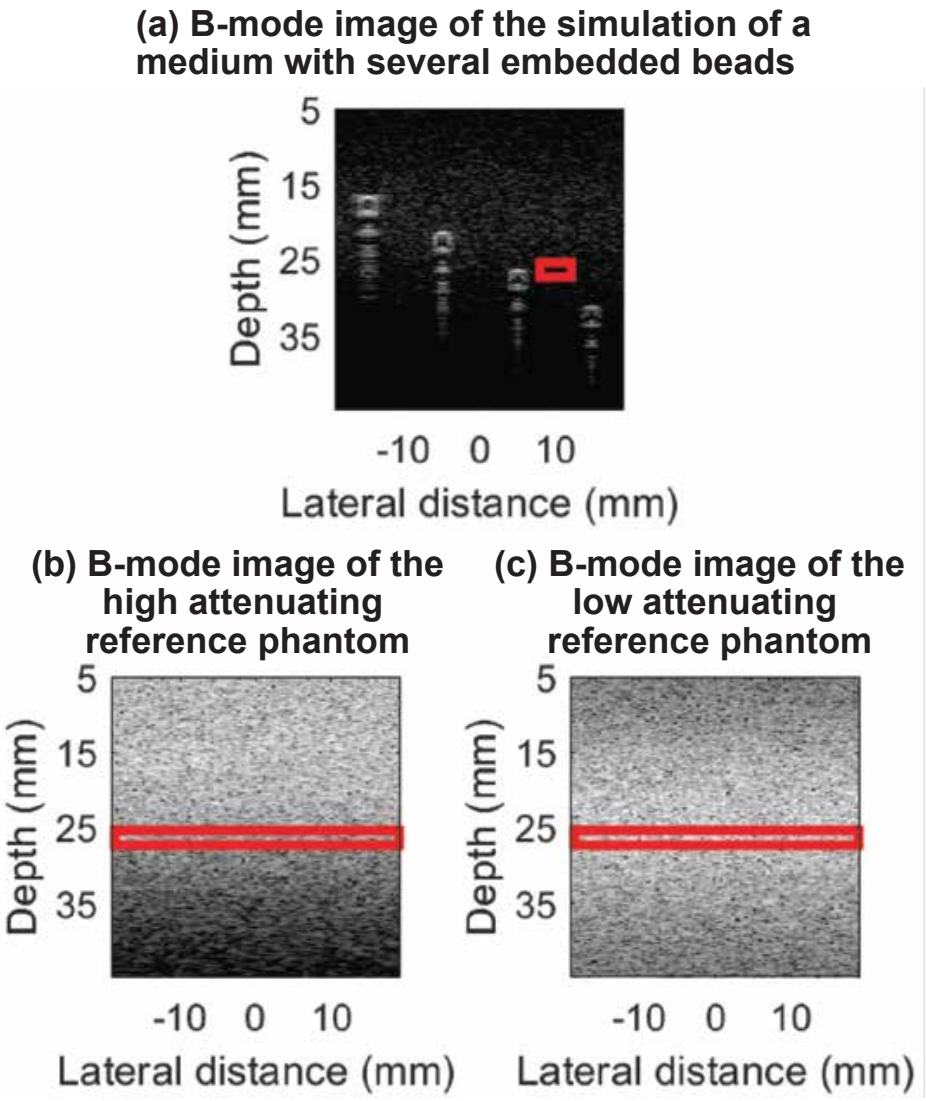

Figure 4.1: (a) B-mode image of the sample phantom simulated with four embedded 2 mm diameter spherical beads located at depths 17.5, 22.5, 27.5, and 32.5 mm. The red rectangles correspond to the regions of interest used for power spectra calculations within the sample and references for the case of the bead located at depth 27.5 mm. (b) B-mode image of the high attenuating reference phantom. (c) B-mode image of the low attenuating reference phantom. Despite the comet tail artifact of the bead, only the first echo of the bead was used for power spectrum corresponding to the *in situ* calibration target. The dynamic range is 50 dB for each image B-mode image.

The attenuation of the reference phantoms were $0.7f^{1.1}$ and $0.028f^{1.75}$ to test two cases where the reference phantom had higher and lower attenuation coefficients than the sample. At HP levels, power spectra might undergo different nonlinear distortion depending on attenuation but also the nonlin-

earity parameter, B/A, of the phantoms. The B/A is relatively high for oil substances but for non-oil substances used in phantom preparation of the phantoms, the B/A is expected to be in the lower range of liquids (between 5 and 7) and different nonlinear distortion in the phantoms was mainly due to the mismatch of their attenuation coefficients.

Figure 4.2 shows the location of the bead and the gated windows used for estimation of the power spectra from the bead, the sample, and the reference phantoms (following the same criterion as in the computer simulations). Similar to the simulations, only the first echo of the bead was utilized rather than echoes from multiple reverberations. The ultrasonic system used for data collection for experiments was a SonixOne (BK Ultrasound, Peabody, MA) with an L9-4/38 transducer. The analysis bandwidth used for the power spectra was from 4.5 to 7.4 MHz. Data were acquired at three power levels increments: 6, 10, and 13 dB with respect to a baseline power level, where the 13 dB increment is the largest power level available in the system.

Rabbit tumor *in vivo*

For the *in vivo* assessment of the *in situ* calibration bead approach, a rabbit breast cancer model was used. The procedure was performed according to a protocol approved by the University of Illinois at Urbana-Champaign Institutional Animal Care and Use Committee (IACUC protocol 20087). A breast tumor was induced in a New Zealand White rabbit (Charles River Laboratories, Wilmington, MA) after implantation of VX2 cells around the mammary pad (while the rabbit was anesthetized with 2% isoflurane). After monitoring the tumor growth for 2–3 weeks and when the tumor reached a diameter of about 3 cm, the hair on top of the tumor location was shaved and a sterilized, 2-mm diameter, spherical titanium bead was embedded within the tumor using a custom metallic syringe. The bleeding in the injection site was minimum at the time of the bead implantation. Three days later, data acquisition was performed with the same ultrasonic system and parameters described in section 4.2.4. A layer of pork belly (thickness $\approx$ 15 mm) bought the same morning in a local supermarket was put on top of the tumor so that the bead was at a depth of roughly 25 mm (similar depth as in the physical phantom experiment or in a potential human organ). The rabbit was euthanized under anesthesia with concentrated CO_2 after ultrasonic data

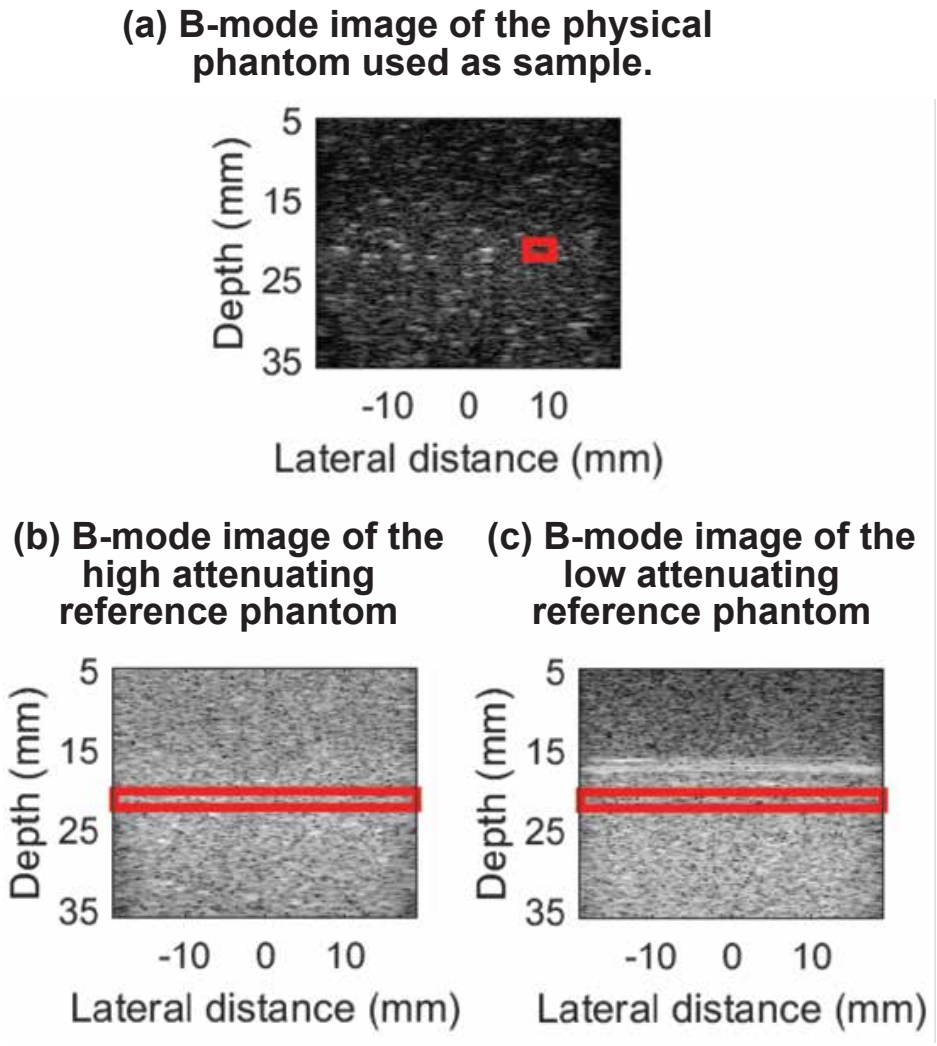

Figure 4.2: (a) B-mode image of the sample phantom with an embedded 2 mm diameter titanium spherical bead pointed by a red arrow. In the red boxes are depicted the gated windows used for power spectra calculation of the ROI located at depth 21 mm within the sample and the high attenuating (b) or low attenuating (c) reference phantoms used for calibration. Notice that the location of the bead (depth 21 mm) determined the location of the selected regions of interest for power spectra calculation.

acquisition was completed. Figure 4.3 shows a B-mode image of the *in vivo* tumor with the bead clearly embedded as well as a data block within the tumor outlined in the red box and at the same depth as the bead. The reference phantom calibration was performed using the same reference phantoms from the previous physical phantom experiments (Section 4.2.4).

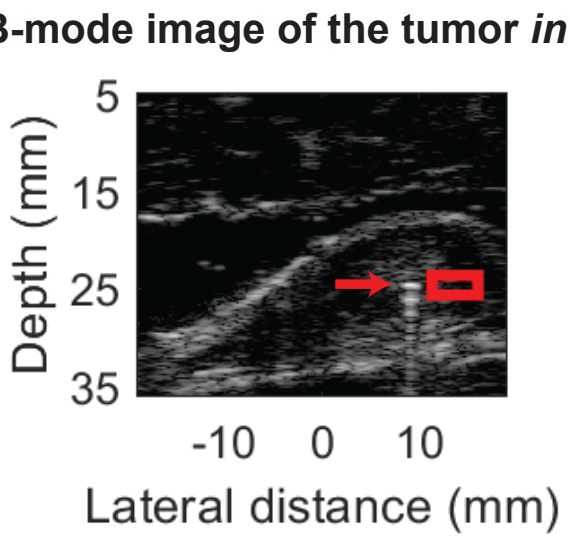

Figure 4.3: B-mode image of the tumor phantom with an embedded 2 mm diameter titanium spherical bead designated by the red arrow. The red rectangle depicts the gated window used for power spectra calculation of the ROI located at a depth of approximately 25 mm.

4.3 Results

In this section, the errors in the estimates of the BSC frequency dependence caused by acoustic nonlinear distortion are reported for the computer simulations, physical phantoms, and rabbit tumor *in vivo* when a power law fit versus frequency is performed.

4.3.1 Computer simulated phantom

Figures 4.4(a) and 4.4(b) show the power spectra corresponding to a ROI in the sample and from a bead within the sample, respectively, at 27.5 mm depth. Figures 4.4(c) and 4.4(d) show the power spectra from the reference phantoms with higher and lower attenuation coefficients (relative to the sample attenuation coefficient), respectively. From the figures, it should be noted that the values of power spectra at different frequencies increased at different rates compared to the nominal selected power increments (6, 14, and 20 dB). For example, for Figure 4.4(a), such increments are listed in Table 4.1 for three frequencies: 4, 6, and 8 MHz. A moderate nominal increment of 6 dB produced similar increments of 6.05, 6.00, and 5.98 dB for 4, 6, and 8 MHz, respectively. At more aggressive power increments, i.e., 20 dB, the actual

increments were 20.05, 19.20, and 18.42 dB for 4, 6, and 8 MHz, respectively. Because the power spectra in the range 4 to 8 MHz were used to calculate the changes in the BSC frequency dependence versus power level, it is reasonable to expect more differences at HP level increments. For regions of interest at 27.5 mm depth, the error in the estimate of the power law exponent is shown in Figure 4.5(c) for the different calibration approaches. An increasing trend of the mismatch versus power level increments was observed regardless of reference phantom calibration or *in situ* calibration. However, the mismatch was larger when the reference phantom method was used. At the 20 dB power level increment, the mismatch was 0.08 with the *in situ* calibration bead, whereas the mismatch was 0.20 when reference phantoms were used. The *in situ* calibration was more accurate than the reference phantom approach because at larger input power levels, the nonlinearity effects from the sample are taken into account better using calibration with the power spectra originating from the bead *in situ*.

Table 4.1: Nominal increment in the power settings and actual increments (in dB) in the power spectra at frequencies 4, 6, and 8 MHz, for the power spectra from the sample at a depth of 27.5 mm as shown in Figure 4.4(a).

Power increment	**at 4 MHz**	**at 6 MHz**	**at 8 MHz**
6 dB	6.055	6.003	5.983
14 dB	14.063	13.798	13.617
20 dB	20.051	19.206	18.426

Figures 4.5(a), 4.5(b), and 4.5(d) show the errors in BSC frequency dependence due to the nonlinearity effects at depths 17.5, 22.5, and 32.5 mm, respectively. Similar to the effects observed at a depth of 27.5 mm, in most cases the *in situ* calibration with the bead produced smaller errors in estimates of the power law exponent than the reference phantom calibrations. In addition, the amount of mismatch also depended on other factors, like the depth. For example, at the shallowest depth of 17.5 mm, the nonlinearity effect was below 0.1, regardless of the 20 dB power level increment or the calibration approach.

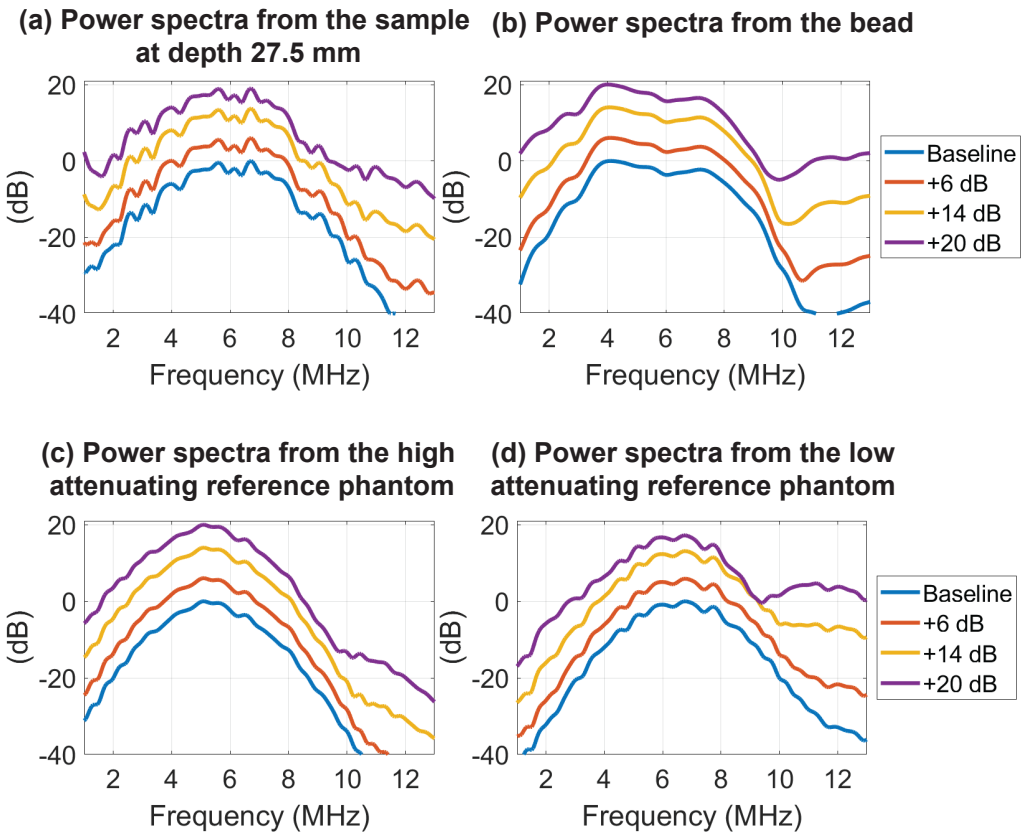

Figure 4.4: Change in power spectra caused by increment of power level settings for regions of interest at a depth of 27.5 mm within the sample (a), from the first echo off of the bead (b), and from two reference phantoms (high attenuating phantom (c), and low attenuating phantom (d)). There are clear excess increments of the power spectra at larger frequencies like 11 MHz, and subtle changes from nominal power level increments at lower frequencies around 6 MHz (shown in Table 4.1 for the power spectra of the sample).

4.3.2 Physical phantom

Figure 4.6 shows the nonlinear distortion of the power spectra corresponding to the ROI depicted in Figure 4.2, for different power level increments: 6, 10, and 13 dB. The average power spectra from the ROI within the sample at the baseline power level and at successive power increments is shown in Figure 4.6(a). Overall, the increments of power spectra appeared to increase by the same factor as the nominal power level increments, however, Table 4.2 indicates that the actual increments at frequencies 5, 6, and 7 MHz were different.

Figure 4.7 shows the error in the power law exponent estimate using the HP settings versus a quasi-linear power level. The mismatch observed using

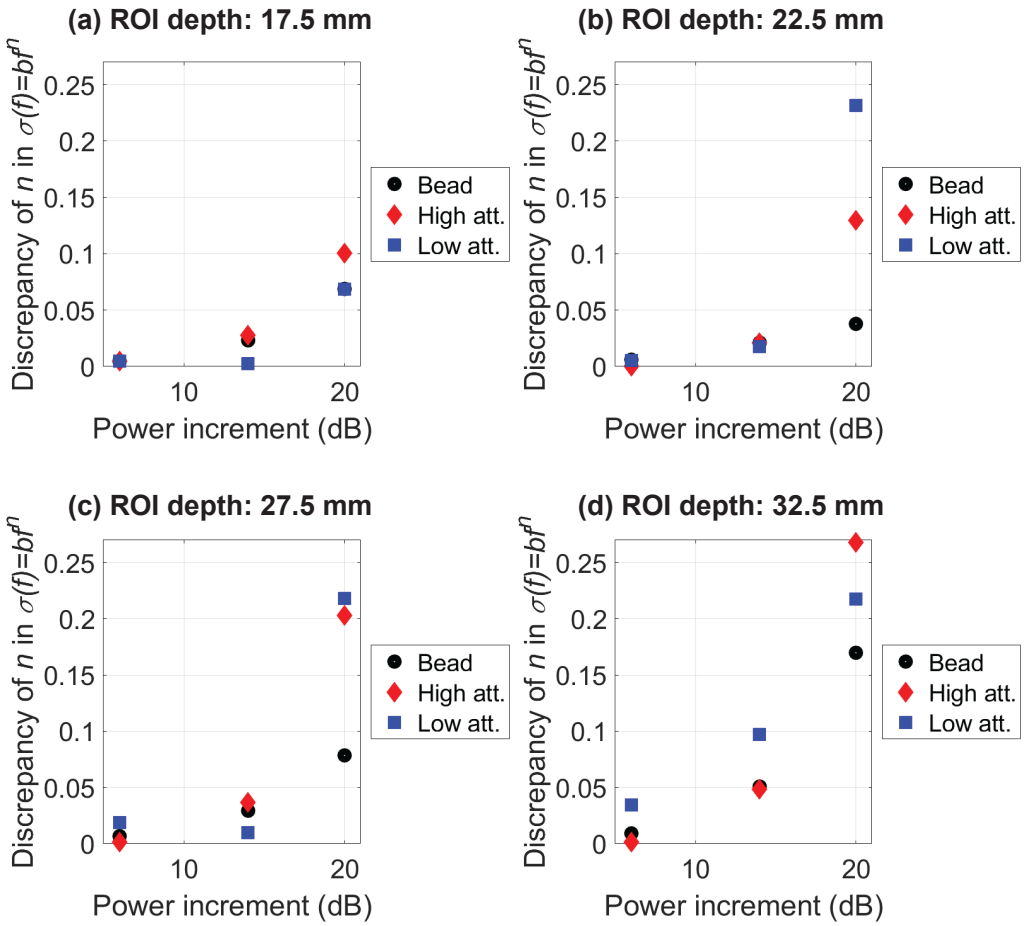

Figure 4.5: Error in the estimate of the exponent in the power law fit of the BSC versus frequency, at several power level increments (6, 14, and 20 dB) calculated from ROIs located at several depths. The *in situ* calibration approach estimated more accurate values compared to the reference phantom approach especially at the largest power level increment, 20 dB.

Table 4.2: Nominal increment in the power settings and actual increments (in dB) in the power spectra at frequencies 5, 6, and 7 MHz as shown in Figure 4.6(a), from the red box ROI depicted in Figure 4.2(a).

Power increment	at 5 MHz	at 6 MHz	at 7 MHz
6 dB	6.722	6.335	6.069
10 dB	11.236	10.578	10.122
13 dB	13.589	12.667	11.918

the *in situ* calibration target was smaller (below 0.4 at 13 dB power level increment) than the mismatch using any of the reference phantoms (above 0.8 at 13 dB power level increment).

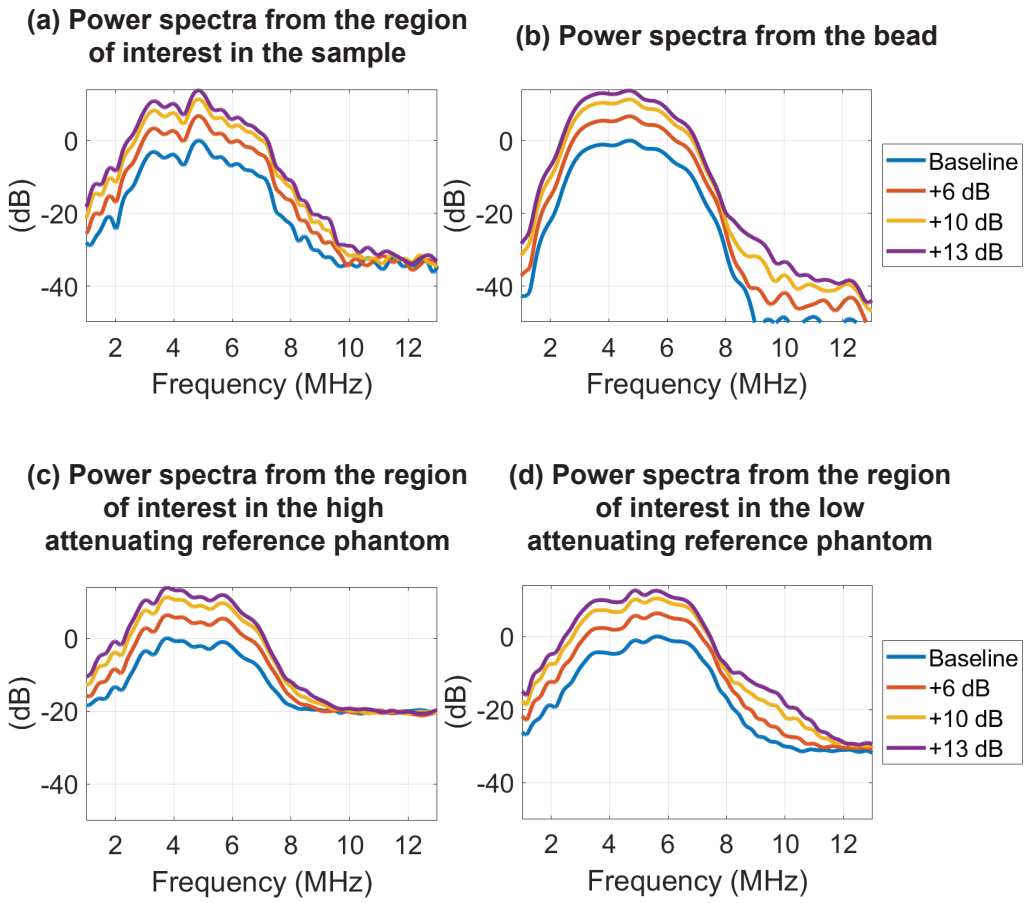

Figure 4.6: Change in power spectra from the ROI caused by nonlinear distortion when acquisition settings are increased in power: the power spectra within the sample (a), the first echo of the bead located at the same depth (b), and the reference power spectra from two reference phantoms (c-d).

4.3.3 *In vivo* sample

Figure 4.8 shows the nonlinear distortion of the power spectra corresponding to the ROI depicted in Figure 4.3, for different power level increments: 6, 10, and 13 dB. Like the phantom experiments, it can be observed that the nominal increments of power level are different from actual increments depending on the frequency. In Table 4.3, the actual increments of the power spectrum at frequencies 5, 6, and 7 MHz show a similar trend as observed previously in Table 4.2, i.e., at the largest increment of power 13 dB, the actual increment at 7 MHz are smaller than the increment observed at a low frequency of 5 MHz.

Figure 4.9 shows the error in the estimate of the power law exponent using HP settings versus a quasi-linear power level. The error was below 0.25

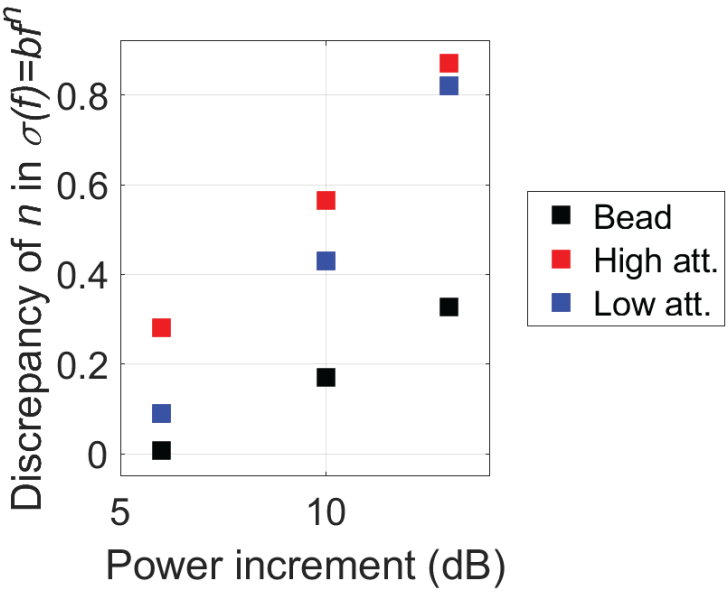

Figure 4.7: Error in the estimate of the exponent for the power law function of the BSC versus frequency at several power level increments (6, 10, and 13 dB) calculated from regions of interest depicted in the Figure 4.2. The *in situ* calibration approach resulted in estimates with small error compared to the reference phantom calibration approach at every power level increment.

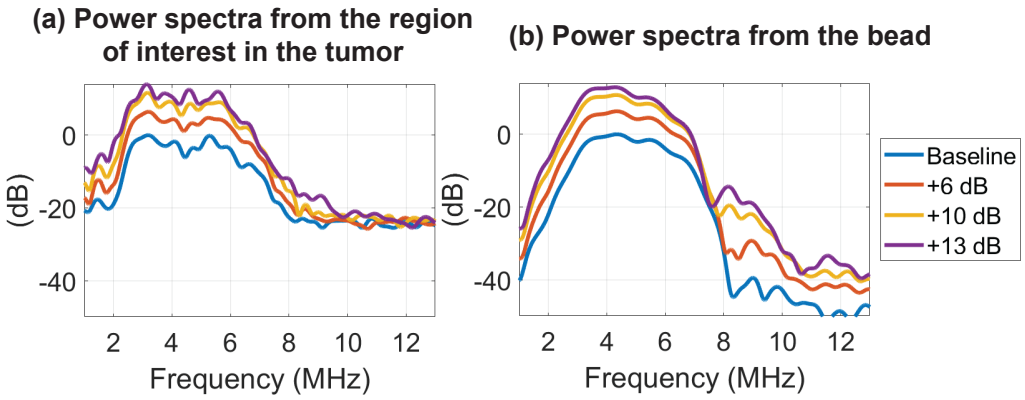

Figure 4.8: Change in power spectra from the ROI in the tumor *in vivo* caused by nonlinear distortion when output settings are increased in power (a), the first echo of the bead located at the same depth (b), and the reference power spectra from two reference phantoms (c-d).

for the *in situ* calibration; however, as increasingly higher power levels were used, the errors using the reference phantoms were larger than 1 at the largest power level increment, 13 dB.

Table 4.3: Nominal increment in the power settings and actual increments (in dB) in the power spectra at frequencies 5, 6, and 7 MHz, for the power spectra from the ROI within the tumor depicted in Figure 4.3.

Power increment	at 5 MHz	at 6 MHz	at 7 MHz
6 dB	6.576	6.149	4.632
10 dB	10.620	9.601	7.411
13 dB	11.943	10.733	7.067

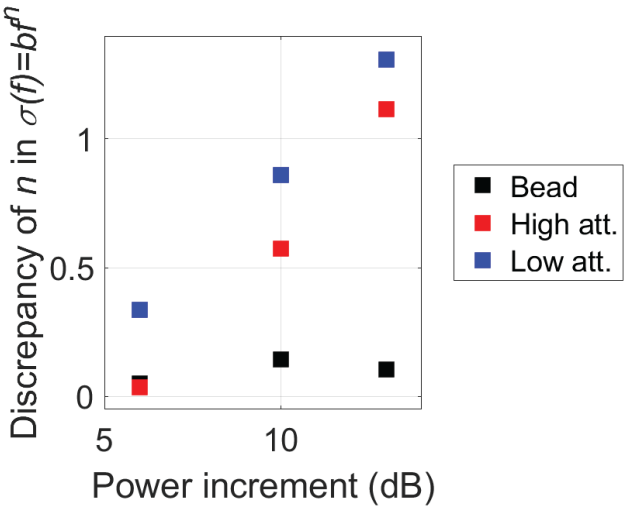

Figure 4.9: Error in the estimate of the exponent of the power law function of the BSC versus frequency at several power level increments (6, 10, and 13 dB) calculated from regions of interest depicted in the tumor *in vivo* in Figure 4.3 and reference phantoms from 4.2(b-c). The *in situ* calibration approach resulted in estimates with small errors compared to the reference phantom calibration approach.

4.4 Discussion

In this chapter, an alternative to the reference phantom method for BSC estimation was evaluated in the presence of non-negligible acoustic nonlinearities, i.e., at power levels leading to acoustic nonlinear distortion. The results of the computer simulations and experiments with physical phantoms resulted in less error in the estimate of the power law exponent function of the BSC versus frequency when using the *in situ* calibration approach. In order to understand why the *in situ* calibration approach is less affected by nonlinear distortion, we can look at the variables in the Gol'dberg number in an attenuating medium: source pressure, frequency range, attenuation coefficient, and B/A. In simulations, all these parameters were the same between

the reference media and sample except the attenuation coefficient. Hence, the mismatch in attenuation coefficients caused a mismatch in Gol'dberg number between sample and reference, and this then caused a mismatch in power spectra resulting in a change in the BSC frequency dependence. In fact, a similar observation was noted in the Chapter 3 (and [57]), where another spectral-based QUS parameter, the attenuation coefficient, was estimated using a reference phantom approach resulting in errors that were correlated with the mismatch between the Gol'dberg numbers from the sample and reference. In other words, the closer the Gol'dberg number between sample and reference the lower the error in the attenuation coefficient estimates. However, when the power spectrum of an unknown sample is calibrated with the power spectra coming from a bead located *in situ*, the nonlinear distortion at high power levels from both regions should be similar. Therefore, the smaller nonlinear distortion of BSC estimates observed for the *in situ* approach is consistent with the observations in [57]. This requires, however, that nonlinearity effects are negligible in the backwards propagation.

Theoretically, signals from the bead or from the gated windows in the sample at the same depth as the bead should undergo exactly the same nonlinear distortion in the forward propagation because the *in situ* bead calibration signal propagated through a medium with the same Gol'dberg number as the interrogated ROI. However, the errors quantified for the BSC were not exactly zero for the *in situ* calibration as shown in Figure 4.5 (although it was smaller than the errors produced using the reference phantom). One explanation for this non-zero error is that the nonlinear distortion generated in the backward propagation might not be completely negligible especially for the larger backscattered pressure from the beads located at depths close to the focal length of the aperture (set at 27.5 mm depth).

Regarding the magnitudes of the error of the BSC exponent that were observed in this chapter, it would be reasonable quantify the magnitude of this error in relative terms. Rayleigh scattering corresponds to an exponent of 4 but in actual phantoms made with graphite used for the scattering and attenuating component, the exponent should be smaller. In a previous study that used similar graphite powder for scattering [64], the BSCs had power law exponents around n=3.3 (obtained from the ground truth curves of Figure 2 of Ref. [64] and the frequency range 4.5–7.4 MHz used in this chapter). Hence, errors found in our results of up to 1 for reference phantoms would

imply a mismatch of about 30%, in comparison with a mismatch below 11% obtained with the *in situ* calibration approach. In addition, other metrics like the ESD could also be degraded by nonlinear distortions, which is related to the BSC exponent (see Figures 2.9 and 2.11 in the Chapter 2). Among the two BSC methods assessed, the reference phantom and the planar reflector, a small error in BSC exponent and ESD was found for the planar reflector approach. However, it is reasonable to believe that the *in situ* calibration approach could lead to further improved QUS tissue characterization compared to the reference phantom.

There are also other limitations of the *in situ* calibration versus the reference phantom method especially for estimations *in vivo*. For example, as of now, the BSC of the sample needed to be estimated from a region near the same depth as the bead to minimize the diffraction effects like focusing. Therefore, if large changes in the bead position occur so that it is outside the target area, errors in the calibration may be introduced.

4.5 Conclusion

In conclusion, results observed in simulations and experiments in phantoms and in tissues *in vivo* suggest that nonlinear distortion can affect the QUS estimates. To mitigate these effects, an *in situ* calibration approach was assessed as an alternative to the reference phantom method, i.e., the *in situ* calibration with a titanium bead could result in more accurate BSC estimates. The results indicate that an *in situ* calibration approach provided some mitigation of nonlinear effects when estimating BSCs compared to the reference phantom approach.

CHAPTER 5

B/A ESTIMATION BASED ON QUANTIFYING EXCESS ULTRASONIC ATTENUATION

5.1 Introduction

The attenuation coefficient is a QUS parameter that has potential in tissue characterization and is required to more accurately estimate other acoustic parameters like the BSC. Particularly, attenuation estimation methods in pulse-echo mode include spectral-based approaches, i.e., in the frequency domain, because of the power law form that attenuation coefficient has versus frequency [9, p. 74]. Moreover, it has been observed in [46] and [57] that estimates of QUS parameters degrade when using spectral-based approaches in nonlinear acoustic regime, i.e., when large excitation pressure levels still within the range of diagnostic imaging are used to insonify a tissue with inherent nonlinear nature (characterized by the nonlinearity parameter B/A). In [57] it was observed that inaccuracies in the attenuation coefficient slopes estimates, either positive or negative errors, called excess attenuation, maintained a strong linear correlation with the logarithm of the Gol'dberg ratio which is the ratio of plane wave Gol'dberg numbers [36, p. 483] of an unknown sample and reference phantom used for calibration. In this chapter, we aim to verify if such correlation still holds for a much larger set of phantoms. We tested 16 numerical phantoms with broader ranges of attenuation coefficient and nonlinearity parameter B/A (while in [57] only excess attenuation was estimated from three phantoms).

Furthermore, an heuristic estimation method for estimation of the nonlinearity parameter of unknown media is presented based on the excess attenuation values. Hence, providing a potential method for estimating B/A in pulse-echo mode that can be used as a complementary metric in tissue characterization *in vivo* or complementing other B/A estimation methods for tissue mimicking phantoms such as the finite amplitude through-transmission

method (measurements of second harmonic) [40] that cannot be performed in a pulse-echo setup.

5.2 Methods

In this section, the spectral log difference method used to estimate the attenuation coefficient is described. The detail of the data from sixteen computer simulated phantoms used to calculate excess attenuation coefficients estimates at a low and high power levels were described. Finally, the derivation of the *B/A* estimation approach—based on the excess attenuation—is provided.

5.2.1 Spectral log difference

The attenuation coefficient vs frequency $\alpha_S(f)$ for a sample can be obtained using power spectra from two windows of an ROI located at different depths z_p and z_d, proximal and distal, respectively, with $z_d > z_p$, as [45]

$$\alpha(f) = \alpha_{\text{ref}}(f) + \frac{1}{4(z_d - z_p)} \log \left[\frac{S(f, z_p) S_{\text{ref}}(f, z_d)}{S(f, z_d) S_{\text{ref}}(f, z_p)} \right], \tag{5.1}$$

where $S(f, z_p)$ and $S(f, z_d)$ are the power spectra from the sample at depths z_p and z_d, respectively. The terms $\alpha_{\text{ref}}(f)$, $S_{\text{ref}}(f, z_p)$ and $S_{\text{ref}}(f, z_d)$ are the attenuation coefficient of a well characterized reference phantom and power spectra from windows located at same depths as in the sample. The reference phantom is used to compensate for beam diffraction effects of the source (e.g., focusing) and the transducer impulse response. The SLD method assumes that acoustic nonlinearities are negligible; therefore, if a pressure level at the source was scaled, no change should be observed in the backscattered RF data received except for the scaling. The attenuation coefficient slope (ACS) is the slope of a linear fit of $\alpha(f)$ estimated in (5.1) over the analysis frequency range typically around the nominal frequency of the transducer.

5.2.2 Numerical simulations of RF data

RF data were obtained using the k-Wave toolbox [47]. Phantom media were simulated with 3D grids of 236×236×412 elements (20.3×20.3×35.5 mm) with uniform B/A and attenuation coefficient values but spatially random distributions of acoustic density (Gaussian distribution with mean 1000 kg/m^3 and 2% standard deviation) to generate scattering. Four $B/A \in \{6, 8, 10, 12\}$ and four ACS$\in\{0.3, 0.7, 1.1, 1.5\}$ dB/cm/MHz were used to generate a total 16 numerical phantoms. A focused transducer (f/2) with 1" focal length was configured in the 3D grid to transmit a 3.5 MHz short Gaussian pulse with 50% fractional bandwidth (−6 dB). The second harmonic distortion was expected to be well described because 2nd harmonic (around 7 MHz) was under the 8.7 MHz limit set by the simulation grid size. 100 RF lines (for spectral averaging) for each phantom were simulated at two different source pressure levels: 100 kPa and 1.3 MPa. Figure 5.1 shows B-mode images after filtering out the 2nd harmonic (which occurs for realistic band-limited transducers). Only minor differences in the images versus pressure level can be observed.

5.2.3 Excess attenuation and B/A estimation

Although, increasing pressure levels apparently will not change B-mode images significantly, distortions in the frequency domain did occur and can be captured through the variations in the ACS estimated with the SLD method.

Excess attenuation

Comparison of attenuation coefficient slope estimates of an unknown sample from acquisitions at pressure levels 100 kPa and 1.3 MPa was computed as

$$\Delta_{\text{sample}} = \text{ACS}_{\text{sample,1.3MPa}} - \text{ACS}_{\text{sample,100kPa}}. \tag{5.2}$$

Given that 16 phantoms were simulated, we chose one as sample and another as reference. Hence, up to 240 distinct pairs can be obtained. For each pair, it will estimated the excess attenuation to verify the linear correlation between excess attenuation and logarithm of Gol'dberg ratio.

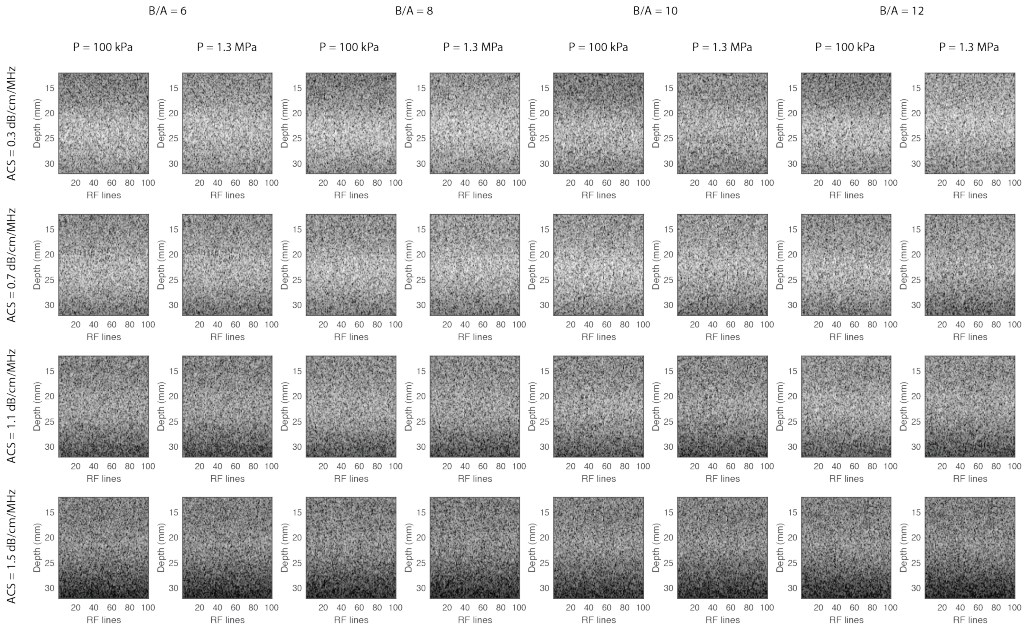

Figure 5.1: B-mode images of the computer simulated RF lines at two different pressure levels: 100 kPa and 1.3 MPa (normalization with respect to the respective maxima is performed). The bottom row shows the case of the highest attenuation phantoms (ACS = 1.5 dB/cm/MHz) with stronger shadowed regions at larger depths. Visual changes between different pressure levels seem to be generally unnoticeable except in the case with smaller attenuation ACS=0.3 dB/cm/MHz and the largest nonlinearity parameter B/A=12 (top right phantom) which is the phantom expected to have the largest Gol'dberg number values.

B/A estimation

The Gol'dberg number for mono-frequency plane waves is by definition [36, p. 483]

$$\Gamma = \frac{k\beta M}{\alpha} = \frac{\omega_0 P_0}{\rho_0 c_0^3}\left(\frac{1+\frac{B}{2A}}{\alpha_0}\right), \tag{5.3}$$

where k is the wave number, $\beta = 1 + \frac{B}{2A}$, M is the Mach number, α_0 is the attenuation coefficient at the fundamental frequency, P_0 is the source pressure, ρ_0 and c_0 are the equilibrium density and sound speed, and ω_0 is the angular frequency. Therefore the Gol'dberg ratio would be

$$\frac{\Gamma_{\text{sample}}}{\Gamma_{\text{reference}}} = \frac{1+\frac{1}{2}\frac{B}{A}_{\text{sample}}}{1+\frac{1}{2}\frac{B}{A}_{\text{reference}}}\frac{\text{ACS}_{\text{reference}}}{\text{ACS}_{\text{sample}}} \tag{5.4}$$

Then, due to the expected quasi-linear relation between the excess atten-

uation and the logarithm of Gol'dberg ratio, we approximated

$$\frac{\Delta_{\text{sample}}}{\Delta_{\text{reference}_2}} \approx \frac{\log_{10}\left(\frac{\Gamma_{\text{sample}}}{\Gamma_{\text{reference}}}\right)}{\log_{10}\left(\frac{\Gamma_{\text{reference}_2}}{\Gamma_{\text{reference}}}\right)}, \tag{5.5}$$

where the "reference$_2$" corresponds to a second reference phantom with known acoustic properties. Then,

$$\Gamma_{\text{sample}} \approx \Gamma_{\text{reference}} \left(\frac{\Gamma_{\text{reference}_2}}{\Gamma_{\text{reference}}}\right)^{\frac{\Delta_{\text{sample}}}{\Delta_{\text{reference}_2}}}, \tag{5.6}$$

which can be rewritten as

$$\begin{aligned} 1 + \frac{1}{2}\frac{B}{A}_{\text{sample}} \approx & \left(1 + \frac{1}{2}\frac{B}{A}_{\text{reference}}\right)\left(\frac{\text{ACS}_{\text{sample}}}{\text{ACS}_{\text{reference}}}\right) \\ & \left(\frac{1 + \frac{1}{2}\frac{B}{A}_{\text{reference}_2}}{1 + \frac{1}{2}\frac{B}{A}_{\text{reference}}}\frac{\text{ACS}_{\text{reference}}}{\text{ACS}_{\text{reference}_2}}\right)^{\frac{\Delta_{\text{sample}}}{\Delta_{\text{reference}_2}}}, \end{aligned} \tag{5.7}$$

from which the B/A of the unknown sample can be computed using true values of the phantoms (set in the k-Wave toolbox or obtained with through-transmission methods in experiments [40]). Using any of the 14 remaining phantoms as "reference$_2$" we can set up to 2260 groups of three distinct phantoms {sample, reference, reference$_2$} whose RF data can be used in (5.7). Finally the fractional error (%error) of the B/A estimated with (5.7) with respect to the B/A true value set in k-Wave was be computed as

$$\%\text{error} = \left|\frac{\frac{B}{A}_{\text{sample, estimated}} - \frac{B}{A}_{\text{sample,true}}}{\frac{B}{A}_{\text{sample,true}}}\right| \times 100\%. \tag{5.8}$$

The fractional errors are presented for two scenarios. Either the group of three phantoms—sample, reference, reference$_2$—have different attenuation coefficient, or the same attenuation coefficient.

5.3 Results

Figure 5.2 shows the excess attenuation estimated by using a source peak pressure 1.3 MPa instead of 100 kPa in nonlinear media. For 240 pairs of

sample and reference, the excess attenuation is highly correlated (r=0.96) with the logarithm of the Gol'dberg ratio between sample and reference, independently of the specific pair of sample/reference used as long as the low and high pressure levels remain the same. The largest deviation was 1.39 dB/cm/MHz for the case when the Gol'dberg ratio was 8.7. Symmetry is observed due to duplication of the phantoms used (when switching a sample and a reference pair) as the minimum deviation was −1.39 dB/cm/MHz for the case when the Gol'dberg ratio was 0.11. The results indicate that a larger mismatch of Gol'dberg numbers between sample and reference resulted in larger excess ACS estimate. Therefore, whenever a large excess attenuation was observed, the Γ mismatch was also large.

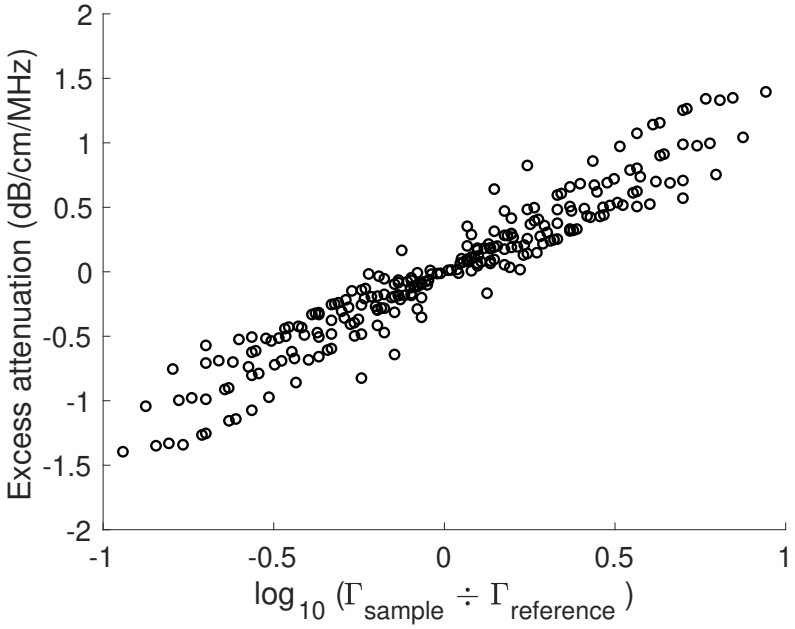

Figure 5.2: Excess attenuation estimated by using a source peak pressure 1.3 MPa instead of 100 kPa in nonlinear media. For 240 pairs of sample and reference the excess attenuation is highly correlated (r=0.92) with the logarithm of Gol'dberg numbers between sample and reference.

The percent error of estimated B/A were small (≤10%) and high (≥50%) for 31% and 22% of 1536 cases when the group {sample, reference, and reference$_2$} had different preset ACS values, as can be observed in the left boxplot of Figure 5.3. However, when the ACS was the same between the phantoms and only had mismatches from B/A, the errors estimated were relatively small (≤10%) and high (≥50%) for 46% and 6% of 96 cases as

shown in the right boxplot of Figure 5.3. Figure 5.4 correspond to excess attenuation measured with pairs sample-reference that share ACS and it was observed that excess attenuation still is linearly correlated with the logarithm of Gol'dberg ratio but the assumption of linearity used in (5.5) holds more strongly when the ACS is shared between the sample and the reference, which might explain why the errors on the right boxplot of Figure 5.3 are lower.

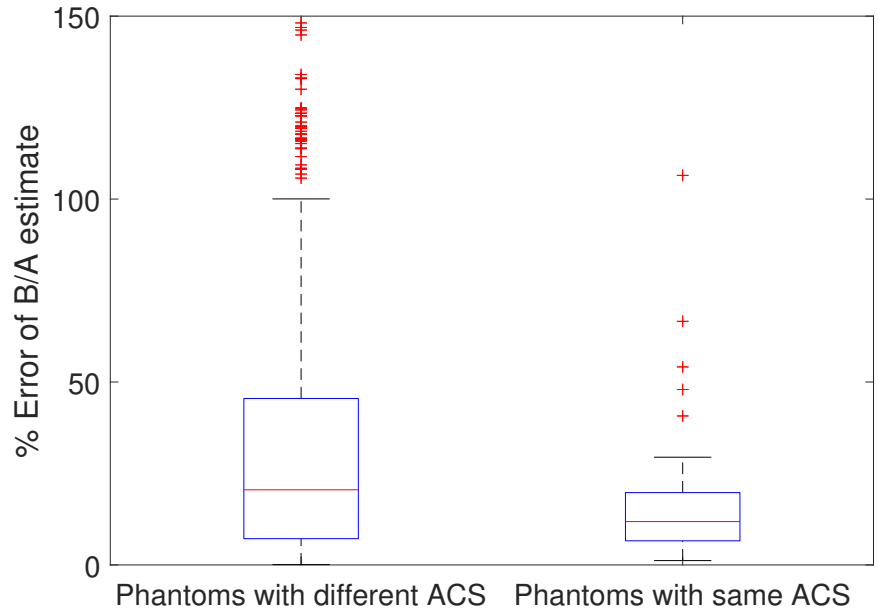

Figure 5.3: Boxplot of the estimated fractional error of the B/A estimates. Left boxplot show the error when phantoms involved in the estimation of Eq. (5.7) are different whereas right boxplot show the case when phantoms only had distinct nonlinearity parameters. Errors were potentially larger when the phantoms do not share the same attenuation coefficient.

5.4 Discussion

This chapter presents a B/A estimation approach that uses the backscattered signals acquired in pulse-echo ultrasound and a common method for attenuation estimation (SLD) in the frequency domain. The method assumed that excess attenuation of ACS values at different pressure levels: low (quasi-linear) and high (nonlinear) was caused by the acoustic nonlinear distortion. This method used available RF data to compute excess attenuation using

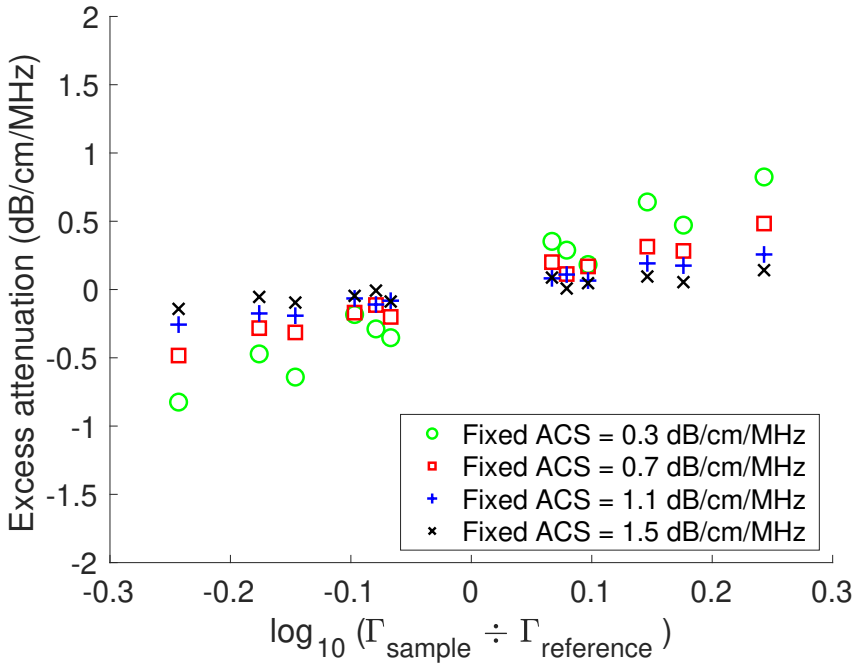

Figure 5.4: Excess attenuation estimated by using a source peak pressure 1.3 MPa instead of 100 kPa in nonlinear media. For pairs sample-reference that share the attenuation coefficient (either one of the four values available) and only has different B/A. For these subset with same ACS, the correlation was larger than 0.98, i.e, better than in Figure 5.2 except for ACS=1.5 dB/cm/MHz with r=0.93 probably because excess values were too small and close to zero.

two excitation pressure levels (one low and another high) with an ultrasonic scanning system.

However, it was observed that to improve the accuracy of this method the phantoms involved in the estimation should have the same attenuation coefficients as the sample. Although for an *in vivo* application, the phantoms could have sound speed very close to that of soft tissues, the attenuation coefficient can be much different than the target tissue. Hence, this method requires the construction of up to two *ad hoc* phantoms with similar attenuating properties as the sample tissue and with B/A characterized by a through-transmission method. Furthermore, even if the attenuation coefficient was exactly the same, only for about half of these cases the error of B/A estimated was below 10%. Future work could be to conduct an analysis to compensate for the non-perfect linear trend evidenced in Figure 5.4 and for the largest ACS where excess attenuation tend to zero and might be more sensitive to errors. Also, it should be mentioned that a limitation of this

approach would be the use of up to two reference phantoms instead of only one used in other spectral-based QUS methods.

In summary, in this chapter, the findings suggest that excess attenuation could be used for estimation of B/A in pulse-echo ultrasound providing that attenuation of media involved have similar attenuation coefficients. Further research is required to analyze fractional errors when mismatches of attenuation coefficient are not zero but still very small and to compensate for non-perfect linear correlation between excess attenuation and Gol'dberg ratio.

CHAPTER 6

NONLINEARITY PARAMETER MAPPING IN PULSE-ECHO USING A REFERENCE PHANTOM

6.1 Introduction

Estimation of the nonlinearity parameter (B/A) of fluid-like media can be useful to assess the state of a medium, e.g., for identifying tissue state. Current methods to estimate B/A include the thermodynamic approach, the pump wave method, or the finite amplitude method [29]. In the later, non-negligible acoustic pressures are applied to a medium and the B/A is estimated by measuring the 2nd harmonic generated at a receiver on the opposite side of the unknown sample. This separation of transducers makes the approach not feasible for most clinical applications using ultrasound. Recent studies have attempted to map B/A in pulse-echo, with efforts focused on the acquisition of the generated 2nd harmonic signal using dual transducers [30] or variations of the pump wave method with setups that used two well-separated frequencies [31]. Unfortunately, none of these methods use only the fundamental band signal making the translation towards clinical setups more complicated. The requirement of *ad hoc* transducers might be a limiting factor to the expansion of B/A estimation methods in pulse-echo.

An alternative to the measuring of the 2nd harmonic is related to the depletion in the fundamental band signal when comparing backscattered signals from two different excitation pressure levels: low (quasi-linear propagation) and high (nonlinear regime). For example, Fatemi and Greenleaf [34] developed a connection between B/A and the ratio of the backscattered signal envelopes reflected off wire targets embedded in an assessed medium. The reflected signals at two excitation pressure levels allowed them to localize regions of high nonlinearity relative to distortion in a known baseline material (such as water).

In this chapter, similar to Fatemi and Greenleaf [34], we used envelopes

of RF signals. Examination of the envelopes means that we are looking mainly at the energy in the fundamental band of the pulse-echo transducer. However, instead of echoes from wire targets, we used the envelope of full backscattered RF data from our samples. We developed a method, based on considering the conservation of energy principle, that related the generation of the 2nd harmonic to the loss of power at the fundamental band when using two excitation levels. The energy in the 2nd harmonic in the instantaneous signal is related to the fundamental through theoretical expressions derived in Gong et al. [30] for dual transducers. The method presented in this chapter was performed in time-domain, in contrast to the frequency domain method developed in Chapter 5. Unlike Chapter 5, in this chapter we were able also to test the estimation technique in numerical phantoms that have non-uniform B/A distribution with the aim to reconstruct parametric images of B/A. An additional set of *ex vivo* and *in vivo* samples were also evaluated.

6.2 Time-domain B/A estimation

In this section, a detailed derivation of the time-domain B/A estimation strategy is presented. We also explain few assumptions regarding the ultrasonic backscattered signals—that were followed during validation with data from computer simulations phantoms, *ex vivo*, and *in vivo*—to derive the proposed technique.

6.2.1 Assumptions of nonlinear propagation in attenuating tissues

In the presented approach, a number of assumptions on the propagation are made:

1. The operation of transducer is in the linear regime, e.g., doubling the voltage input (V_0) of the transducer means the output pressure (P_0) of the transducer will double as well: $2 \times V_0 \rightarrow 2 \times P_0$. We tested this assumption in physical experiments by measuring the ultrasonic output of a transducer at different power levels near the surface of the transducer before nonlinear distortion would occur.

2. Most of the energy would be in the fundamental band and 2nd harmonic due to tissue attenuation of harmonics 3rd, 4th, etc. This assumption was tested by quantifying the energy in the higher harmonics in media having realistic values of attenuation and B/A via simulation.

3. The lowest excitation results mainly in generation of fundamental linear response. This assumption was tested in multiple works throughout this thesis. Our low signal values did not result in significant nonlinear distortion.

4. Transducers filter out the second harmonic to have a backscattered envelope primarily at the fundamental. This assumption was validated by examining the impulse response of the transducers used in the work.

5. Scattering is weak so the path back to the transducer does not result in additional nonlinear distortion but only attenuation of the signal. Backscatter from speckle is usually more than 40 dB down from the main forward propagating wave making the backscattered signal less than the low power signal used as a reference.

6. Plane wave on transmit can be conducted using the fundamental bandwidth. As will be observed later, the wave propagation from the transducers is only approximately planar. Variations from the plane wave is a source of error in the estimates of B/A using the proposed technique.

6.2.2 Derivation of the B/A with a reference phantom

An ultrasonic transducer operating in pulse-echo mode receives RF backscattered signals. These signals, according to (4), are measured at the fundamental band for an excitation level i, P'_{1i}. If we measure at a low excitation level 1,

$$P'_{11}(z) = \frac{\gamma_1(z)}{z} P_{11}(z) \exp\left(-\int \alpha_1(z)dz\right), \tag{6.1}$$

where P_{11} is the incident pressure at depth z. Then the pressure measured at the transducer can be related to the pressure associated with the fundamental at the depth z, with estimated attenuation $\alpha_1(f_0, z)$ and with reflection coefficient of γ_1 associated with the fundamental band. Likewise, at higher

excitation level 2,

$$P_{12}^{'}(z) = \frac{\gamma_1(z)}{z} P_{12}(z) \exp\left(-\int \alpha_1(z) dz\right). \tag{6.2}$$

At depth z, the total energy is related to P^2, and using the assumption (2),

$$P_{Tot,i}^2 = \sum_{n=1}^{\infty} P_{ni}^2 \approx P_{1i}^2 + P_{2i}^2 \tag{6.3}$$

where P_{ni}^2 represents the pressure squared of the n-th band. In this equation, only the fundamental and second harmonic are assumed to contribute to the total energy in the backscattered signal. In subsequent derivations, we 'remove' the depth dependence of some variables to keep the descriptions tidy.

For a low excitation level, i=1, the total pressure at some depth z is

$$P_{Tot,1}^2 \approx P_{11}^2 + P_{21}^2 \approx P_{11}^2. \tag{6.4}$$

For a higher excitation level, i=2, which has a higher voltage excitation by a dimensionless factor υ,

$$P_{Tot,2}^2 \approx P_{12}^2 + P_{22}^2 \approx \upsilon^2 P_{Tot,1}^2. \tag{6.5}$$

This approximation is not exact due to attenuation of the second harmonic leading up to this depth but is approximately true. This yields the equality,

$$P_{12}^2 + P_{22}^2 \approx \upsilon^2 P_{11}^2. \tag{6.6}$$

Rearranging,

$$P_{22}^2 \approx \upsilon^2 P_{11}^2 - P_{12}^2. \tag{6.7}$$

Plugging in (6.1) and (6.2),

$$P_{22}^2 \approx \left(\upsilon^2 P_{11}^{'2} - P_{12}^{'2}\right) \left(\frac{z}{\gamma_1}\right)^2 \exp\left(2\int \alpha_1 dz\right). \tag{6.8}$$

At a distance z from the source, the reflected echo signal for the second harmonic for excitation level 2 satisfies (according to Eq. (11) from Gong *et*

al. [30]),

$$\frac{dP_{22}}{dz} = K(z)P_{12}^2 - \alpha_2(f_2, z)P_{22} \tag{6.9}$$

or in terms of the pressure measured at the transducer,

$$\frac{dP_{22}}{dz} = K(z)P_{12}'^2 \left(\frac{z}{\gamma_1}\exp\left(\int \alpha_1 dz\right)\right)^2 - \alpha_2(f_2, z)P_{22}, \tag{6.10}$$

where $K(z) = \frac{\pi f_0}{\rho_0 c_0^3}\beta$ and $\alpha_m(f_m, z)$ is the attenuation coefficient at the fundamental or second harmonic at depth z with $m \in \{1, 2\}$, respectively. The modified nonlinearity parameter β, i.e., the Beyer parameter, is related to the nonlinearity parameter B/A as $\beta = 1 + \frac{B}{2A}$. Plugging (6.8) into (6.10) yields

$$\begin{aligned}\frac{d}{dz}\left(\left(\upsilon^2 P_{11}'^2 - P_{12}'^2\right)^{\frac{1}{2}} \frac{z}{\gamma_1}\exp\left(\int \alpha_1 z\right)\right) = \\ \frac{\omega}{4\rho_0 c_0^3}\beta P_{12}'^2 \left(\frac{z}{\gamma_1}\right)^2 \exp\left(2\int \alpha_1 z\right) - \\ \alpha_2(f_2, z)\left(\left(\upsilon^2 P_{11}'^2 - P_{12}'^2\right)^{\frac{1}{2}} \frac{z}{\gamma_1}\exp\left(\int \alpha_1 z\right)\right).\end{aligned}$$

And solving for β

$$\beta = \frac{4\rho_0 c_0^3 \left(\frac{d}{dz} + \alpha_2\right)\left(\left(\upsilon^2 P_{11}'^2 - P_{12}'^2\right)^{\frac{1}{2}} \frac{z}{\gamma_1}\exp\left(\int \alpha_1 dz\right)\right)}{\omega P_{12}'^2 \left(\frac{z}{\gamma_1}\right)^2 \exp\left(2\int \alpha_1 dz\right)}.$$

To compensate for the γ_1 terms, a similar expression can be obtained using a reference phantom with approximate similar density and sound speed.

$$\begin{aligned}\frac{\beta}{\beta_{\text{ref}}} = \frac{\left(\frac{d}{dz} + \alpha_2\right)\left(\left(\upsilon^2 P_{11}'^2 - P_{12}'^2\right)^{\frac{1}{2}} \frac{z}{\gamma_1}\exp\left(\int \alpha_1 z\right)\right)}{\left(\frac{d}{dz} + \alpha_{2,\text{ref}}\right)\left(\left(\upsilon^2 P'^2_{11,\text{ref}} - P'^2_{12,\text{ref}}\right)^{\frac{1}{2}} \frac{z}{\gamma_{1,\text{ref}}}\exp\left(\int \alpha_{1,\text{ref}} dz\right)\right)} \\ \cdot \frac{P'^2_{12,\text{ref}}\left(\frac{z}{\gamma_{1,\text{ref}}}\right)^2 \exp\left(2\int \alpha_{1,\text{ref}} dz\right)}{P_{12}'^2 \left(\frac{z}{\gamma_1}\right)^2 \exp\left(2\int \alpha_1 dz\right)}.\end{aligned}$$

Furthermore, assuming $\gamma_{1,\text{ref}}$, i.e., for the reference phantom is independent of the depth, then

$$\frac{\beta}{\beta_{\text{ref}}} = \frac{\left(\frac{d}{dz}+\alpha_2\right)\left(\left(v^2P_{11}'^2 - P_{12}'^2\right)^{\frac{1}{2}}\frac{\gamma_{1,\text{ref}}}{\gamma_1} z\exp\left(\int \alpha_1 z\right)\right)}{\left(\frac{d}{dz}+\alpha_{2,\text{ref}}\right)\left(\left(v^2P'^2_{11,\text{ref}} - P'^2_{12,\text{ref}}\right)^{\frac{1}{2}} z\exp\left(\int \alpha_{1,\text{ref}}dz\right)\right)} \cdot \frac{P'^2_{12,\text{ref}}}{P_{12}'^2}\cdot\left(\frac{\gamma_1}{\gamma_{1,\text{ref}}}\right)^2 \cdot \frac{\exp\left(2\int \alpha_{1,\text{ref}}dz\right)}{\exp\left(2\int \alpha_1 dz\right)}, \tag{6.11}$$

i.e., β from an interrogated medium can be estimated from echo signals in the time-domain. The only remaining term is $\gamma_1/\gamma_{1,\text{ref}}$. For the reference, at excitation level 1,

$$P'_{11,\text{ref}} = \frac{\gamma_{1,\text{ref}}}{z}P_{11,\text{ref}}\exp\left(-\int \alpha_{1,\text{ref}}dz\right). \tag{6.12}$$

Noting that $P_{11,\text{ref}} \approx P_{11}\exp\left(\int(\alpha_1-\alpha_{1,\text{ref}})dz\right)$ gives

$$P'_{11,\text{ref}} = \frac{\gamma_{1,\text{ref}}}{z}P_{11}\exp\left(\int(\alpha_1-2\alpha_{1,\text{ref}})dz\right). \tag{6.13}$$

Dividing (6.13) by (6.1), and rearranging to solve for $\gamma_1/\gamma_{1,\text{ref}}$ gives,

$$\frac{\gamma_1}{\gamma_{1,\text{ref}}} = \frac{P'_{11}}{P'_{11,\text{ref}}}\exp\left(2\int(\alpha_1-\alpha_{1,\text{ref}})dz\right). \tag{6.14}$$

Replacing (6.14) in (6.11) will finally provide an estimate of β, from which we can derive the B/A of the unknown sample.

6.3 Analysis in computer simulations

The B/A estimation method was tested using the nonlinear acoustics simulation MATLAB package k-Wave [47]. RF data from numerical phantoms were computed using a linear array source/receiver of 128 elements with dimensions of 6 mm by 38.4 mm. In transmission, all elements simultaneously send a broadband pulse to mimic the plane wave acquisition approach [65]. The dimensions chosen for the linear array were based on a L9-4/38 transducer (BK Ultrasound, Peabody, MA) which also has a geometric focus at

19 mm (elevation focusing). In general, the elevation focusing was included in our simulations (unless otherwise stated). A 3D random scattering media (random density values with mean 1000 kg/m^3 and 2% standard deviation) was excited with a broadband, 50% bandwidth Gaussian pulse centered at 5 MHz. Two peak pressures of the pulse were tested: low pressure (100 kPa) and high pressure (1 MPa). Hence, the scaling factor was $\upsilon = 10$. The values of B/A and attenuation were selected for the simulations for either sample or reference and these were varied to test the algorithm.

6.3.1 Third harmonic vs second harmonic

To verify that most of acoustic energy is in the fundamental band and 2nd harmonic, assumption (2), we located receivers in the simulated nonlinear and attenuating medium with B/A=6 and attenuation 0.5 dB/cm/MHz. Figure 6.1 shows waveforms valid up to the third harmonic at the high pressure level 1 MPa at several depths. There is a clear distortion of the waveform at 20 and deeper even in an fairly attenuating medium.

The power spectra of these waveforms, normalized to their fundamental maxima, is shown in Fig. 6.2. There are non-negligible 2nd and 3rd harmonics at depths 20, 30, and 40 mm. At these depths, the 2nd and 3rd harmonic are roughly -13 dB and -22 dB, respectively, below the fundamental maximum. Hence the 3rd harmonic is roughly -9 dB below the 2nd harmonic. In the propagation back to the source, the 3rd harmonic will be further attenuated by about 2.5 dB/cm more than the 2nd harmonic. Therefore, the signals received by transducer were mainly in the fundamental band and the 2nd harmonic (>14 dB above the 3rd harmonic). At the low pressure level, 100 kPa, the 2nd and 3rd harmonics were negligible in the same media (>40 dB below the fundamental band), hence, the assumption (3) can be considered appropriate.

6.3.2 Elevation focusing vs non-elevation focusing

The geometrical properties of the elements of a linear array transducer determine the elevation focusing. This implies a deviation from the plane wave assumption (6). We assessed the impact of the 19 mm elevation focusing

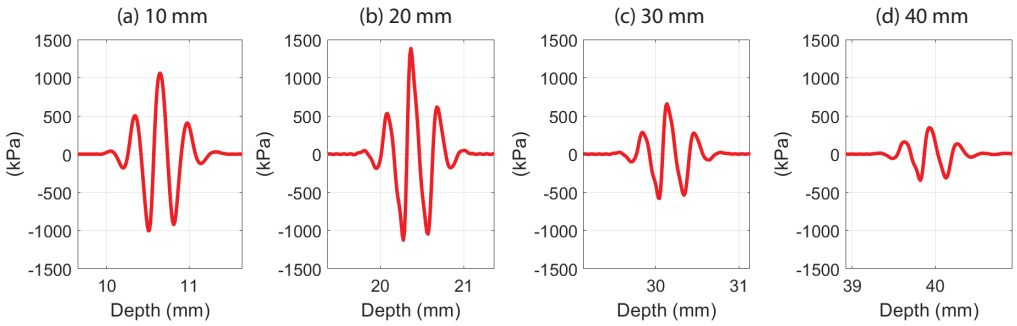

Figure 6.1: Waveform of the simulated pulse at different depths for a nonlinear (B/A=6) and attenuating medium (0.5 dB/cm/MHz). Notice that the maximum distortion occurs around the elevation focusing 19 mm.

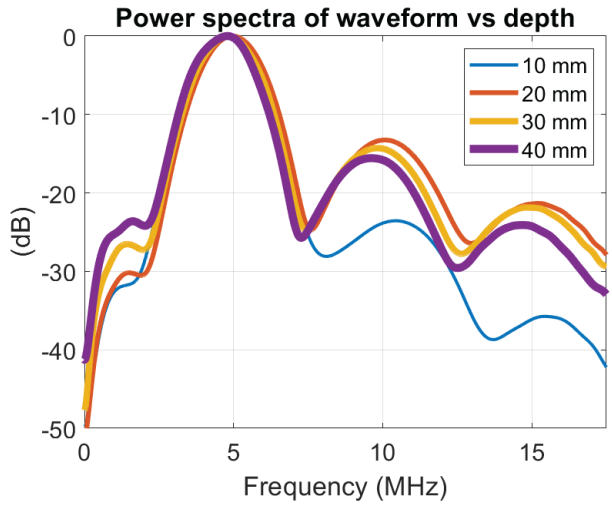

Figure 6.2: Power spectra of the incident waveforms from Fig. 6.1 normalized at their maxima of the fundamental band. At 10 mm, the 2nd harmonic is about −25 dB from the fundamental. At further depths, there is non-negligible 2nd and 3rd harmonic. However, it is expected the 3rd harmonic received by backscattering will be −14 dB or even smaller than the 2nd harmonic.

versus non-elevation focusing case. The sample media was a heterogeneous phantom with a background B/A=6 and an 18 mm diameter circle inclusion (B/A=9) to simulate an abnormal fatty region. In the reference, the B/A=6, which is a typical value for most reference phantom materials. Both sample and reference were set to be attenuating media with the same attenuation coefficient 0.5 dB/cm/MHz. The excitation levels were set at pressures 100 kPa and 1 MPa, hence, a scaling factor $v = 10$. In reception, beamforming was performed with a dynamic aperture given by a constant f-number that, in our case, was chosen to be 3 [65]. Preprocessing by filtering-out the second harmonic signal was also performed for each RF line with a passband filter in

the range 4–6 MHz to mimic the filtering effect of the harmonics of backscattered signals that occur in reception by real transducer. Figure 6.3 shows the B-mode images of the numerical phantom and their inclusion location is depicted in a yellow circle (centered at depth 22.5 mm). The conventional B-mode imaging does not capture the fact that the circular inclusion (B/A=9) had 50% larger nonlinearity parameter than the background (B/A=6).

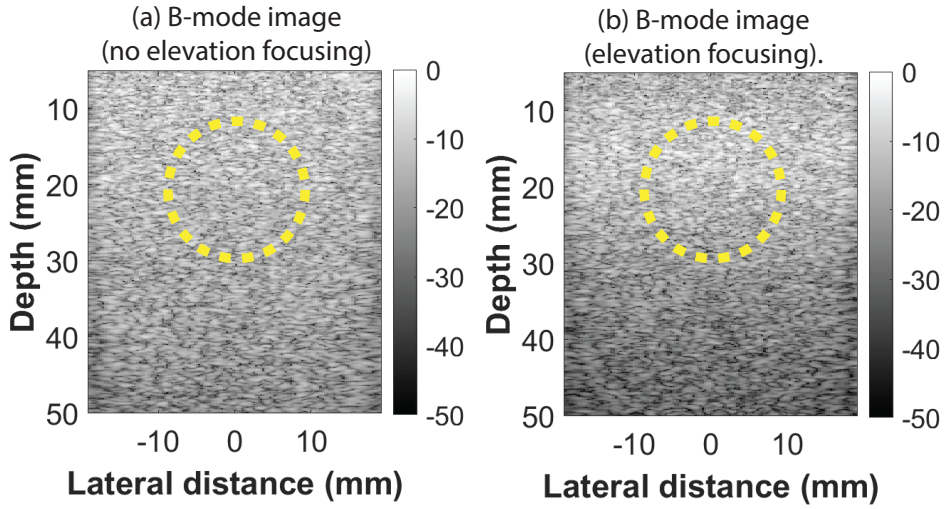

Figure 6.3: B-mode images from a numerical phantom with non-uniform B/A. The inclusion depicted in yellow had B/A=9, whereas the background had B/A=6. The B-mode images do not capture changes of higher nonlinearity parameter within the inclusion despite being 50% larger nonlinearity parameter. (a) No elevation focusing was assumed. (b) Including 19 mm elevation focusing.

On the other hand, Figure 6.4 shows the parametric image of B/A obtained with the proposed method. In the region before the inclusion (depth<13 mm), the map is relatively uniform with values close to the expected B/A=6. In the lateral region of the phantom outside the inclusion there were no meaningful changes and a uniform $B/A\approx$6 remained until the bottom of the image. However, in the inclusion region, we observed changes of the B/A map. Qualitatively, in both elevation focusing cases (with or without), the highly nonlinear region is followed by a shadowing effect even at depths past the inclusion location where estimated B/A values were larger than the expected B/A=6. From this finding, it should be noted that the obtained parametric images have a cumulative averaged B/A nature versus depth. Nevertheless, it was also found that including elevation focusing created just slightly larger estimates but is able to capture nonlinear regions reasonably well. Hence, we continue with the rest of this chapter using simulations that included

elevation focusing because it more closely mimics the realistic scanning configuration.

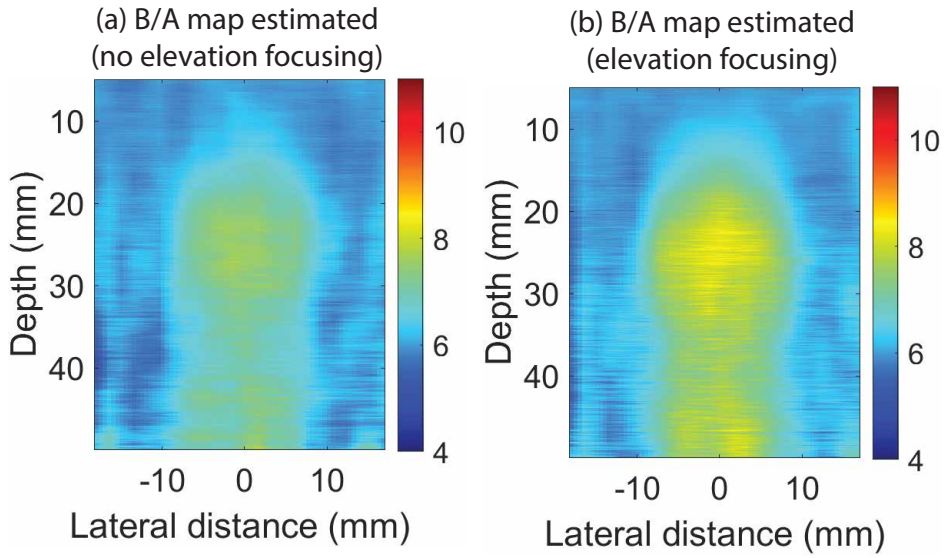

Figure 6.4: B/A parametric images constructed with our time-domain reference phantom approach (note: for actual reconstruction smoothing with a 30 wavelength moving average filter in the axial direction) was often used). The parametric image is able distinguish the inclusion with larger B/A. Notice that the obtained parametric images have a cumulative averaged B/A form. (a) Without elevation focusing. (b) Including elevation focusing.

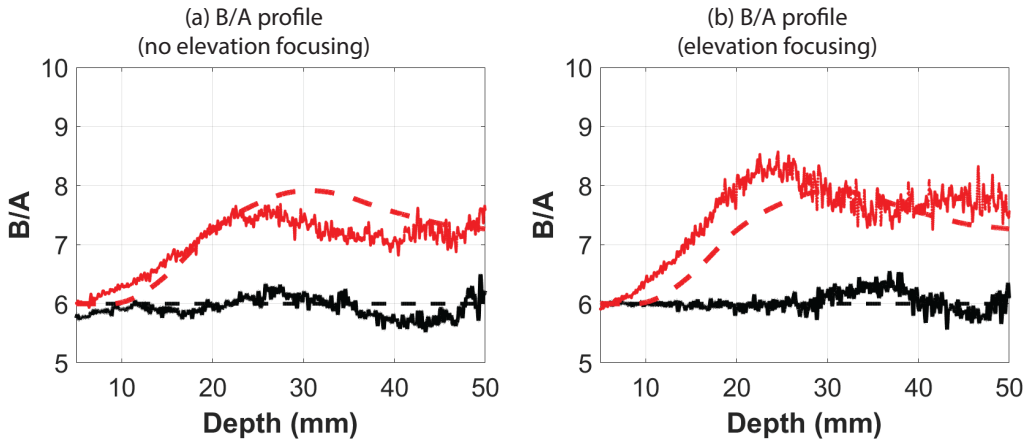

Figure 6.5: B/A vs depth at lateral positions 0 (red), and -12 mm (black) in Fig. 6.4. In dashed are the cumulative averaged B/A at each depth obtained after averaging the local values of the ground truth B/A map. (a) Without elevation focusing. (b) Including elevation focusing.

6.3.3 Uniform B/A sample

Next, we tested a sample that had uniform B/A much larger than the B/A of the reference phantom. In the simulations, the sample media was a homogeneous phantom with B/A=11 to represent a large fatty region across all of the field of view. In the reference, the B/A=6. Both sample and reference were set to have same attenuation coefficient 0.5 dB/cm/MHz. Figure 6.6 shows the parametric image obtained with the presented approach. It should be noted that the edge effects from a finite aperture source are perceived in the reconstructed B/A image. Figure 6.7 shows a profile of B/A versus depth. The B/A follows the ground truth value (B/A=11) with less than 10% error until 35 mm depth. At 40 mm and deeper depths, the values of B/A were slightly overestimated up to errors of about 20%.

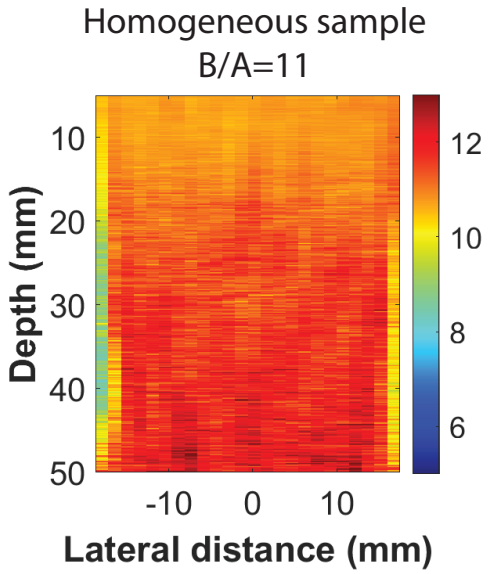

Figure 6.6: B/A parametric images of an homogeneous sample with large B/A=11. The parametric image obtained is fairly uniform except towards the lateral regions. The plane wave assumption is less in the lateral regions due to edge artifacts.

6.3.4 Incorrect assumptions of attenuation coefficients

In Eq. (6.11), we require values of α_1 (attenuation coefficient at the fundamental band) and α_2 (attenuation coefficient at the 2nd harmonic). In section 6.3.2, we used the actual values of attenuation coefficients set in k-

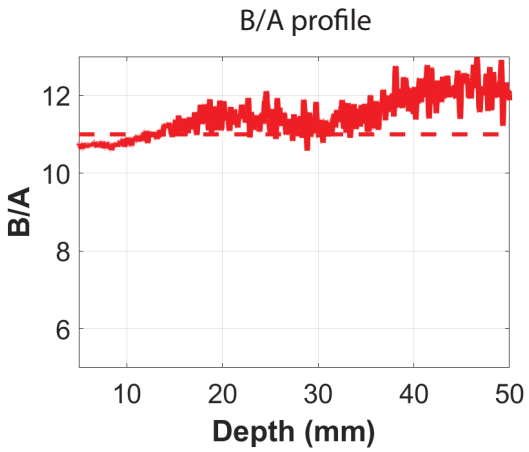

Figure 6.7: B/A vs depth at lateral positions 0 (middle of the image in Fig. 6.6). Notice that for a homogeneous sample, the cumulative averaged values and the local values should be constant and equal to B/A=11.

Wave with frequencies of 5 and 10 MHz for α_1 and α_2, respectively. However, in clinical setups the values of α_1 or α_2 estimated through spectral methods could be biased due to the stochastic nature of backscattering signals (see [45]) or biased due to nonlinear effects (as shown in Chapter 3). Therefore, we tested cases where the values of α_1 or α_2 used in Eq. (6.11) were inaccurate by $\pm 10\%$ or $\pm 20\%$, and assessed the impact of such incorrect values on the estimated B/A maps. For this section, we used the simulated data from section 6.3.2 that included elevation focusing. Figure 6.8 shows the estimated B/A maps using erroneous values of α_1 or α_2 in Eq. (6.11) either by underestimation (b-e) or overestimation (f-i). There is a positive correlation between B/A bias in the parametric maps and biases of α_1 or α_2. Also, it can be observed that bias of α_2 could bring more errors than bias of α_1 in the B/A maps reconstructed.

6.3.5 B/A local maps

In our derivation of B/A, the values apparently include a nonlinear effect accumulated and averaged versus depth in the propagation path to and certain depth. Assuming the effective B/A estimated is a cumulative average of the local B/A values, then a possible mapping of the the local ACS maps to an averaged cumulative B/A as the ones we obtained can be written as

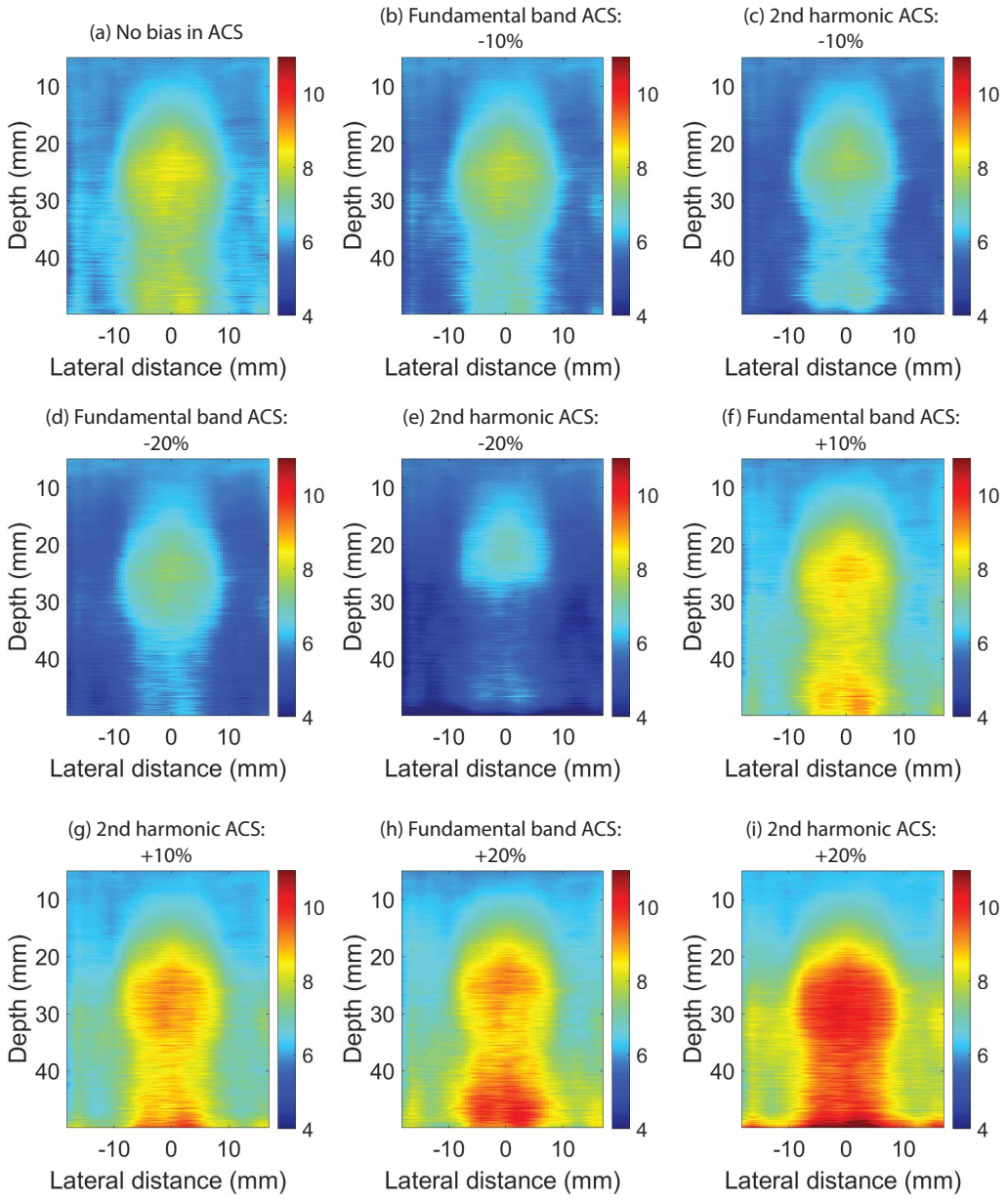

Figure 6.8: B/A estimated using erroneous values of α_1 or α_2 in Eq. (6.11) either by underestimation (b-e) or overestimation (f-i). The importance of accurate values of α_1 or α_2 is observed in the bias of the resultingB/A maps. There is a positive correlation between B/A bias in the parametric maps and biases of α_1 or α_2. The same percentage of bias in α_2 more error in the B/A estimates than bias in α_1.

$$\begin{bmatrix} 1 & 0 & 0 & \cdots & 0 & 0 \\ \frac{1}{2} & \frac{1}{2} & 0 & \cdots & 0 & 0 \\ \frac{1}{3} & \frac{1}{3} & \frac{1}{3} & \cdots & 0 & 0 \\ \cdots & \cdots & \cdot & \cdots & 0 & 0 \\ \frac{1}{H-1} & \frac{1}{H-1} & \frac{1}{H-1} & \cdots & \frac{1}{H-1} & 0 \\ \frac{1}{H} & \frac{1}{H} & \frac{1}{H} & \cdots & \frac{1}{H} & \frac{1}{H} \end{bmatrix}_{H\times H} \begin{bmatrix} \frac{B}{A}_{1,\text{local}} \\ \frac{B}{A}_{2,\text{local}} \\ \frac{B}{A}_{3,\text{local}} \\ \cdots \\ \frac{B}{A}_{H-1,\text{local}} \\ \frac{B}{A}_{H,\text{local}} \end{bmatrix}_{H\times 1} = \begin{bmatrix} \frac{B}{A}_{1,\text{average}} \\ \frac{B}{A}_{2,\text{average}} \\ \frac{B}{A}_{3,\text{average}} \\ \cdots \\ \frac{B}{A}_{H-1,\text{average}} \\ \frac{B}{A}_{H,\text{average}} \end{bmatrix}_{H\times 1}, \tag{6.15}$$

where H is the length of a B/A column vector (i.e., in the axial direction). The expression in (6.15) can be repeated sequentially to obtain all B/A columns and then a 2D map. To solve (6.15) we can use the linear least squares solution. For ill-conditioned inverse problems, a regularization approach such as Tikhonov regularization is a fast way to smooth the linear least squares solution if needed [66, Chapter 4].

Figure 6.9 shows the B/A parametric images estimated after solving the inverse problem in Eq. (6.15). The least squares solution and Tikhonov regularization results with regularization parameters 0.0002, 0.01, and 0.05 show parametric images without the shadowing effect observed before in Fig. 6.4. Therefore, including a degree of smoothing in the solution of the linear mappings is critical. Figure 6.10 show the B/A vs depth from two lateral positions (one of them crossing the large B/A inclusion). The Tikhonov regularization with regularization parameter 0.01 better balanced the trade-off between accuracy and precision. We added a moving average of about 30 wavelengths axially in the the ground truth local B/A values to match the smoothing performed in the envelopes utilized in Eq. (6.11).

6.4 Experiments *ex vivo* and *in vivo*

To complement the validation of the proposed B/A estimation method, two experimental data sets were used: first, data from a physical phantom with non-uniform distribution of B/A having an *ex vivo* highly nonlinear fatty tissue embedded in an agar and graphite matrix; and second, data acquired *in vivo* from a "uniform" region of an animal liver.

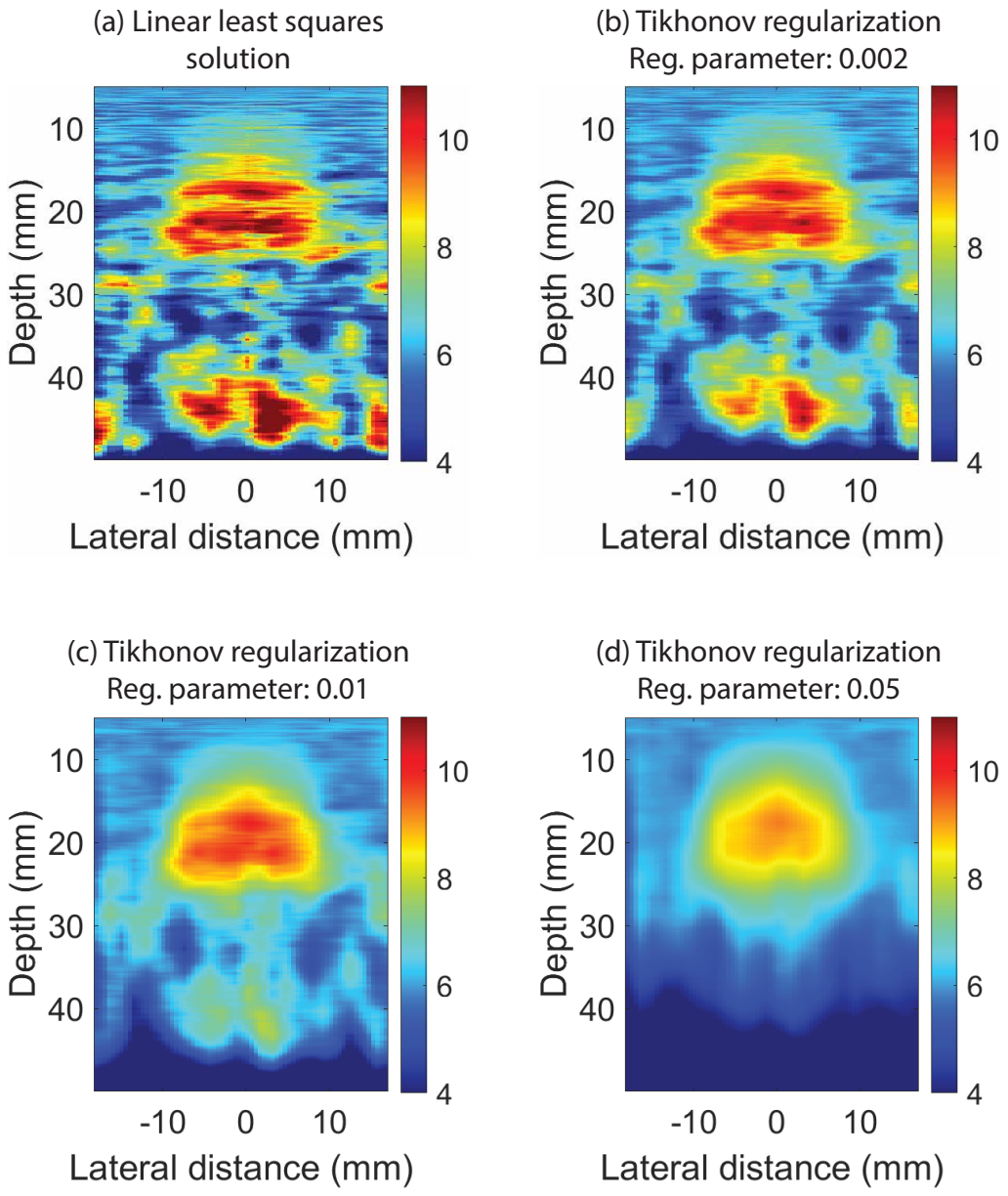

Figure 6.9: Local values of B/A estimated after further solving an inverse problem in Eq. (6.15). (a) The linear least squares solution. (b-d) Tikhonov regularization with regularization parameters 0.0002, 0.01 and 0.05. The local B/A maps does not present the shadowing effect observed in Fig. 6.4

6.4.1 Physical phantom with inclusion

A reference phantom was prepared using a mixture of 400 mL deionized/degassed water, 12 g of bacteriological agar (Sigma-Aldritch, St. Louis, MO), and 15 g of graphite powder (John Deere, Moline, IL). The speed of sound and attenuation coefficient were estimated to be 1490.2 m/s and $\alpha(f) =$

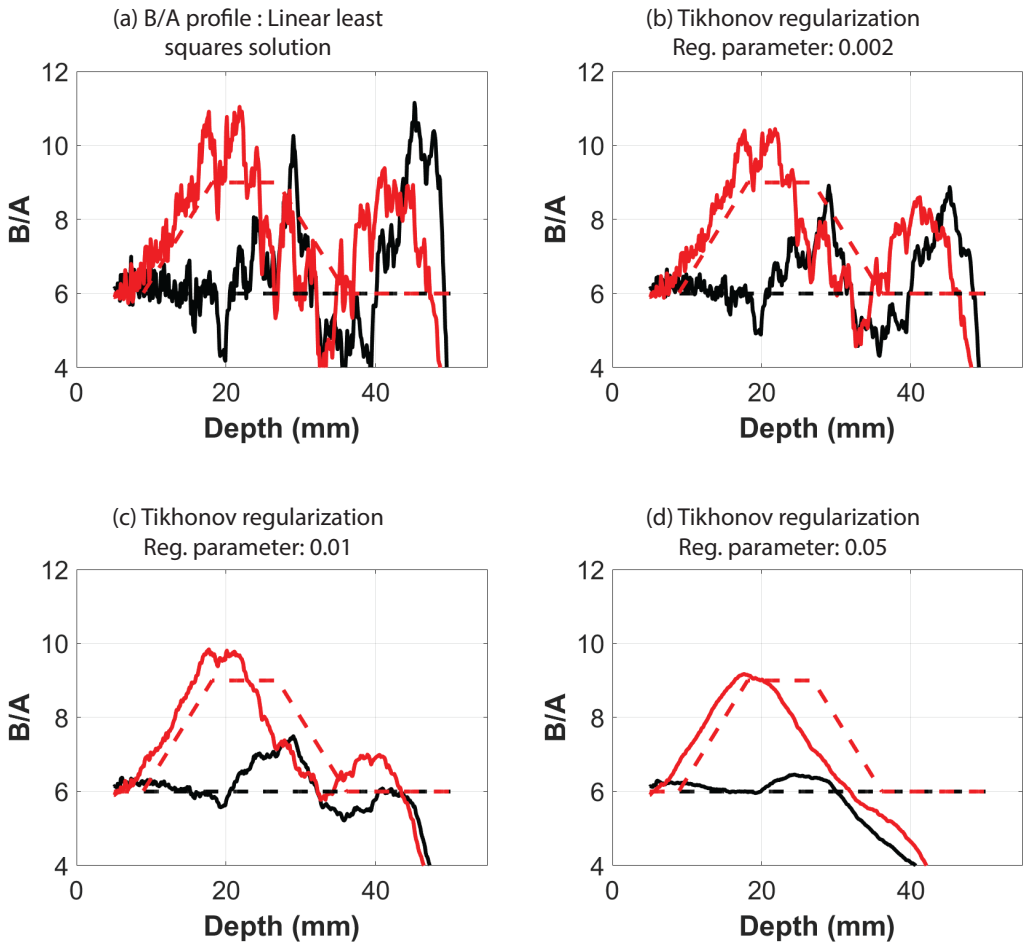

Figure 6.10: B/A vs depth at lateral positions 0 (red), and -12 mm (black) in Fig. 6.9. In dashed are the local B/A. (a) The least squares solution. (b-d) Tikhonov regularization with regularization parameters 0.0002, 0.01 and 0.05.

$0.28f^{1.34}$ dB/cm, respectively (estimated with insertion loss techniques in the range 4-11 MHz at room temperature). The B/A of similar graphite/agar mixture has been found in the literature to be 5.4±0.4 measured at 22 °C. These acoustic parameters were used in Eq. (6.11). In the sample phantom, a fatty porcine tissue (pork belly) was used as an inclusion with larger B/A than the background material (the same mixture used in the reference phantom preparation). The porcine tissue speed of sound and attenuation coefficient were estimated at 1532.7 m/s and $\alpha(f) = 1.95f^{1.16}$ dB/cm, respectively (estimated with insertion loss techniques in the range 1.5-6 MHz at room temperature). This speed of sound is in agreement with the value 1530 m/s reported for porcine back fat in Niñoles et al. [67] measured at room temperature. The attenuation values of porcine were larger than reported in

the literature in Koch et al. [68] for subcutaneous fat tissue. However, in [68] the temperature was 38 °C and an inverse correlation between attenuation coefficient and temperature in fatty tissues [69] can explain this mismatch. For porcine fat the B/A has been found in the literature to be 9.6 measured at 24 °C [70].

The RF acquisition procedure was performed with an L9-4/38 transducer (BK Ultrasound, Peabody, MA) driven by a Vantage 256 system (Verasonics Inc., Kirkland, WA). RF data frames were acquired using a plane wave approach without angular compounding [65]. Two power levels were transmitted with a broadband excitation signal to the transducer having an input voltage of amplitude 4 V (low energy level) followed by an input voltage of amplitude 40 V (high energy level). Although the nominal scaling factor (required in Eq. (6.11)) was ν=10, the actual scaling factor was measured using a needle hydrophone (Precision Acoustics Ltd., UK) very close to the surface of the center of the transducer and was found to be ν=10.98.

Figure 6.11(a) shows the B-mode image from a phantom embedded with an *ex vivo* fatty sample. Figure 6.11(b) shows a picture from the actual fatty chunk embedded in the agar/graphite background. Figure 6.12 shows the B/A map estimated from the phantom embedded with the *ex vivo* sample. Two cases were tested: unknown attenuation of the inclusion, therefore, assigning it the same attenuation coefficient as the background; or by using the calculated value from the fatty piece using an insertion-loss method. In the first case, an underestimation of B/A in the inclusion region was observed. For the second case an overestimation of the B/A in the fatty chunk was observed. We found in section 6.3.4 that large errors in the B/A maps could be observed when the values of attenuation coefficient used in the estimate of B/A deviated 10-20% from the actual values. Therefore, these results suggest that the values used for α_1 and α_2 in Eq. (6.11) might be too large. Additionally, the center frequency of the broadband pulse used in the experiments will downshift due to frequency-dependent attenuation. The attenuation values used in Eq. (6.11) are assumed to be the values at the center frequency of the pulse. Therefore, the change in instantaneous center frequency versus depth is not taken into account with Eq. (6.11) and could result in the overestimation of B/A of the fatty chunk in Fig. 6.12.

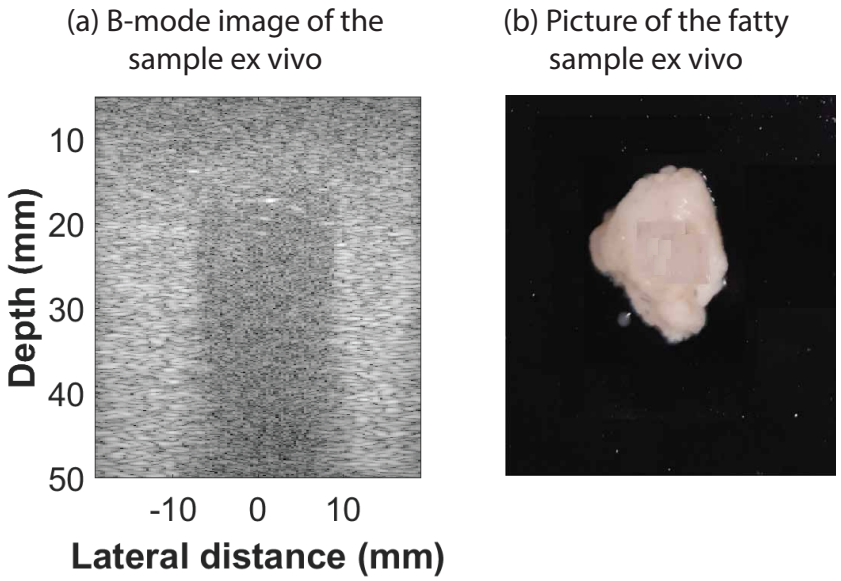

Figure 6.11: (a) B-mode image from a phantom embedded with a fatty pork belly sample. (b) A picture scaled to (a) of the actual fatty pork sample to be embedded in the phantom (made of graphite/agar mixture).

6.4.2 *In vivo* assessment

In vivo soft tissue data were acquired according to a protocol approved by the University of Illinois at Urbana-Champaign Institutional Animal Care and Use Committee (IACUC protocol 20087). Data were taken from a healthy liver in a New Zealand White rabbit (Charles River Laboratories, Wilmington, MA) while the rabbit was anesthetized with 2% isoflurane. The hair on top of the base of the rib cage was shaved and ultrasonic gel was applied to have better contact between skin and transducer to perform the ultrasonic data acquisition. Once the data acquisition was completed, the rabbit was euthanized with concentrated CO_2 while under anesthesia.

RF data acquisition was performed using the same setup as in section 6.4.1. The movement artifacts between acquisitions at the two different power levels was minimized by doing a sequential acquisition sequence in the Vantage system (time between acquisitions was on the order of milliseconds). We used a reference phantom with sound speed close to that of soft tissues. Specifically, the reference phantom used for the *in vivo* assessment were made from agarose, n-propanol, condensed milk, and water with glass bead scatterers uniformly placed in the phantom spatially at random. The speed of sound of this phantom was around 1540 m/s, which is close to the speed of sound

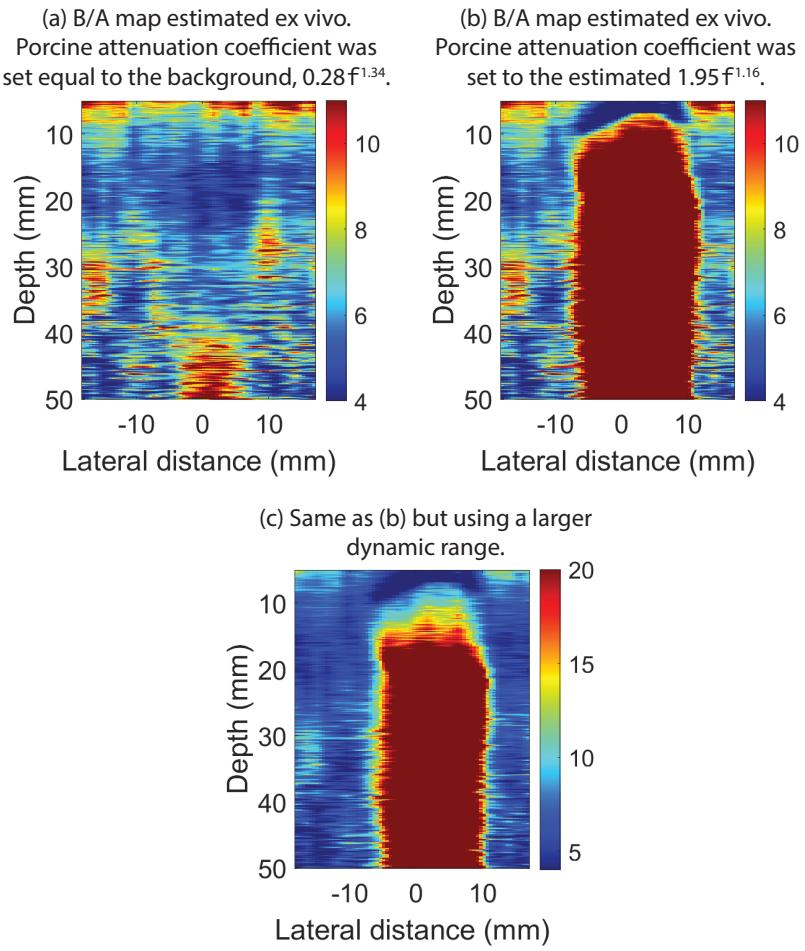

Figure 6.12: *B/A* map of the fatty sample *ex vivo*. (a) When the attenuation of the inclusion was "unknown" and set to the same attenuation coefficient as the background, $0.28f^{1.34}$. (b) When the attenuation coefficient of the inclusion was set to the value $1.95f^{1.16}$. (c) *B/A* map similar as (b) but using a larger dynamic range still show a strong overcompensation.

in soft tissues *in vivo* [3], whereas the speed of sound of rabbit liver is 1575 m/s at 26 °C according to literature values [71]. The attenuation of this phantom was $\alpha(f) = 0.79f^{1.05}$ (in the range of 4.8-8 MHz) and B/A=6.8, measured in the laboratory using the through-transmission method [40]. The attenuation coefficient of rabbit liver has been found in the literature to be 0.71 dB/cm/MHz [72] at 37 °C. This value was used to estimate α_1 and α_2 needed in Eq. (6.11).

Figure 6.13 shows the B-mode image of the rabbit liver *in vivo*. Figure 6.13(b) shows some anatomical parts of the liver like the diaphragm or the portal vein and the fairly uniform region selected to calculate *B/A*

statistics (mean and standard deviation). We tried to exclude the portal vein because of its small SNR.

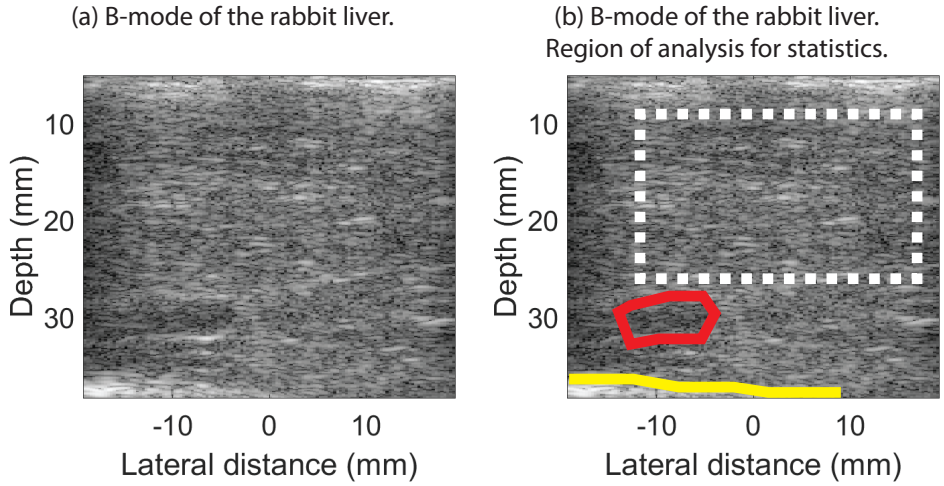

Figure 6.13: (a) B-mode image of the rabbit liver *in vivo* (50 dB dynamic range). (b) Same as (a) but depicting the portal vein (red), diaphragm (yellow), and the region of analysis used for statistics calculations of the B/A of the rabbit liver in white dashed.

Figure 6.14(a) shows the estimated B/A map with the cumulative averaged form. Figure 6.14(b) shows the local B/A values obtained after solving the inverse problem with a Tikhonov regularization parameter 0.01. The mean and standard deviation of the B/A inside the dashed box regions were B/A=7.1±1.6 and B/A=5.0±3.9 for Figs. 6.14(a) and (b), respectively. It should be noted that solving the inverse problem to calculate the local values of B/A might increase the noise of the cumulative averaged B/A map by the nature of the derivative operation. We did not find in the literature the B/A of rabbit liver, but the B/A of human liver is around 6.75 [26] measured at 37 °C, and for bovine liver the value is 7.25 [73] measured at 30 °C. In our case assuming the region in the liver is uniform, the local values of B/A can be approximated to our estimations of B/A cumulative averaged. So we could say the B/A of the liver was 7.1 which is in the range of the B/A of other mammalian species.

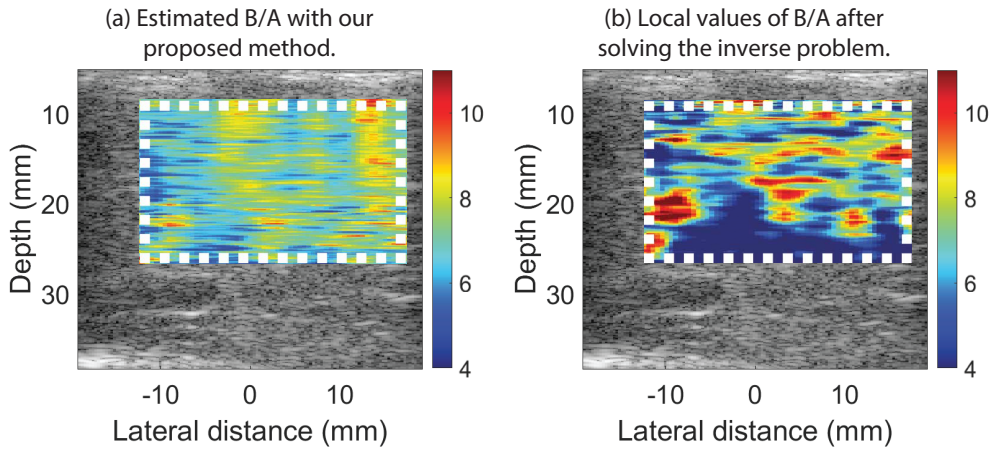

Figure 6.14: (a) B/A map of the cumulative averaged map overlaid in a B-mode image. (b) B/A map of local values after solving Eq. (6.15). The mean $\pm$ standard deviation of the regions within the dashed boxes were 7.1$\pm$1.6, and 5.0$\pm$3.9, for (a) and (b), respectively.

6.5 Discussion

In this chapter, we presented a time-domain method able to derive parametric images of the B/A in nonlinear, scattering, and lossy media using the conservation of energy principle as a means to obtain an implicit value of the 2nd harmonic. The approach also required a reference phantom. Our approach differs from state-of-the-art methods in that we use only the fundamental band acquisition signals (no dual transducers, pump wave setups or embedded wire targets). The technique provided a cumulative averaged B/A rather than being a local representation of the B/A. For regions with large B/A, a shadowing effect was observed similar to what attenuation causes in B-mode images. In a previous work of Fatemi and Greenleaf [34], a similar shadowing effect was observed. This was explained by the cumulative nature of nonlinearity. The results in simulations showed that some assumptions, like the plane-wave assumption, are flexible and including elevation focusing still produce reasonable accurate results.

Accurate values of attenuation coefficients should be known *a priori* to be used as input in Eq. (6.11). Errors of 10% in attenuation values utilized could be significant and reduce the accuracy of the estimated B/A maps. Accurate values of α_2 may not be available for many interrogated tissues. While literature values can be used as a starting point for attenuation estimates, they will often be inadequate. This is especially true when attempting to assess

a disease state of tissue where attenuation might be a marker for disease. Therefore, when possible, it would be useful to estimate the attenuation of a medium based on RF backscatter techniques like the spectral log difference (SLD) method.

The theoretical framework developed here required the use of attenuation coefficients at two frequencies: fundamental band (f_0) and second harmonic ($f_2 = 2f_0$) in Eq. (6.11). The frequencies used in the equations are assumed to be the center frequencies of the ultrasonic pulse being propagated. However, the pulses used in both simulation and experiment were broadband rather than narrow-band. In a lossy media, the center frequency of the pulse shifts to a lower value as the pulse propagates. Therefore, keeping an unadjusted value of the center frequency in Eq. (6.11) may lead to errors in the estimate of B/A. The fact that this center frequency would depend on depth needs to be further evaluated especially for highly attenuating medium like the porcine sample we used (α_{pork} around 2 dB/cm/MHz). Using frequency values that change with depth might explain why at deeper depths, it was common to find overestimated values of B/A.

The change in the center frequency of the pulse can be estimated versus depth, allowing a more correct estimate versus depth. For example, assuming a Gaussian pulse with 50% bandwidth the center frequency downshift versus depth (z) is $f_{0,z} = f_0 - 0.18 f_0^2 \alpha_0 z$ [74]. In Fig. 6.15 we reexamined the data from the ideal case where sample and reference share the same attenuation and uniform media. Performing the correction did not substantially change the estimated B/A map. However, the compensation of the downshift is dramatic for the case of having mismatches in attenuation of the sample and reference phantom. Without compensation, the B/A map is overcompensated at larger depths similar to what we observed in the B/A map of phantom with the fatty *ex vivo* tissue.

Next, we tried to do a similar compensation for the phantom containing the *ex vivo* sample. In this case, $f_{0,z} = f_0 - 0.26 f_0^2 \alpha_0 z$, which is slightly different than the correction from the simulation case because the bandwidth in the waveform in the experiments was 60% instead of 50%. Moreover, for a nonuniform attenuating medium (e.g., with an inclusion), it should be noted that in the frequency correction expression the term $\alpha_0 z$ works only when there is no change in attenuation axially; otherwise, an integral term of the form $\int \alpha(z) dz$ should be considered. The frequency compensation is

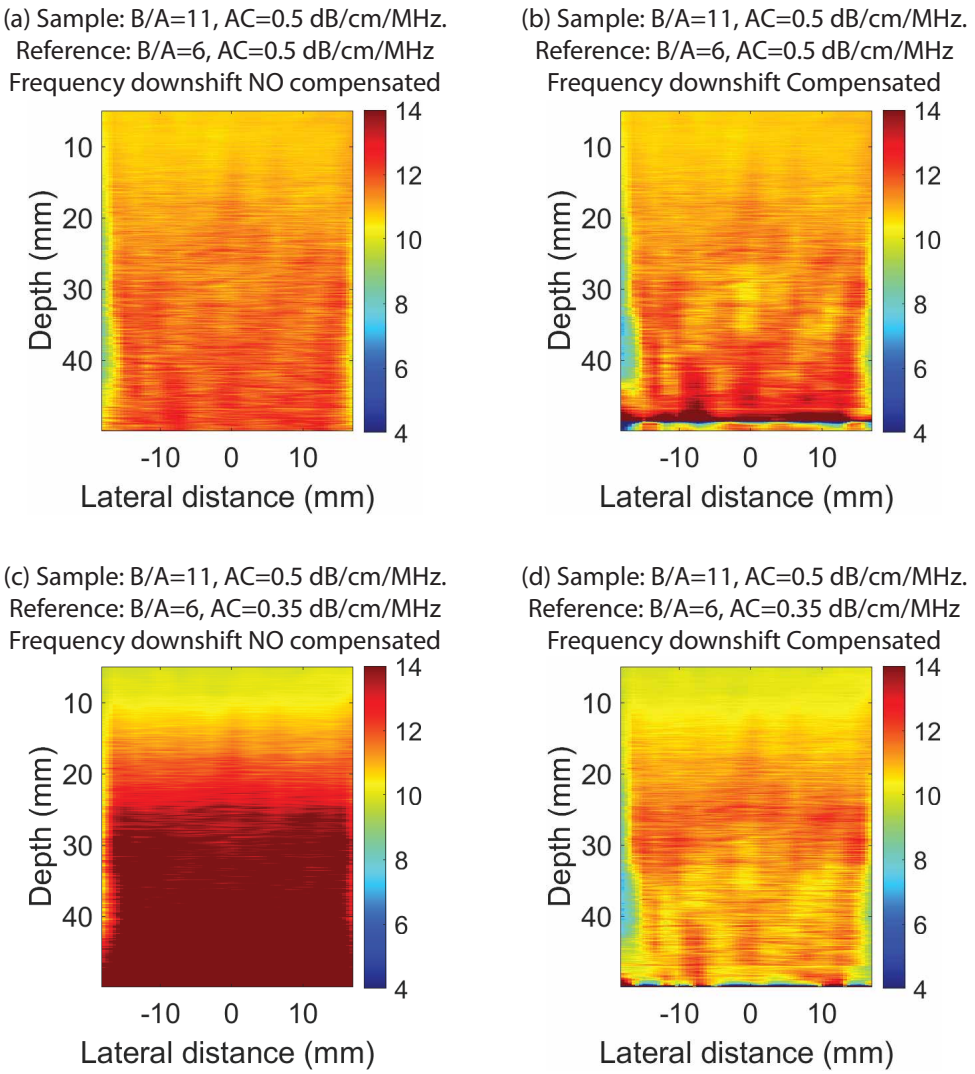

Figure 6.15: Analysis of downshift compensation in homogeneous media for B/A map reconstruction. The downshift is critical when phantoms do not share the attenuation coefficient (c-d) compared to when the sample and reference share the attenuation coefficient (a-b).

required to have linear frequency dependence; thus, for this sample all the attenuations were approximated with a linear frequency dependence resulting in 0.55 dB/cm/MHz for the background and 2.45 dB/cm/MHz for the *ex vivo* sample. Figure 6.16(a) shows the reconstruction without frequency compensation, which is basically the same as Fig. 6.12(b). Figure 6.16(b) shows the reconstruction including the frequency correction compensation. Figure 6.16(c) shows the B-mode image of the sample to note the location of the actual inclusion. The frequency correction reduces the overestimation noted in 6.16(a), until around 22 mm depth in the phantom. At much larger

depths the B/A map underestimates the values of B/A. In Fig. 6.16(d) we show the estimated downshift in the center frequency of the pulse corrected vs location in the sample for the 2nd harmonic (note that this should be around 10 MHz close to the surface). In the middle of the chunk of pork the frequency downshifted to negative values (black zones in 6.16(d)). For our purposes, that would mean that it is better not arrive at any conclusions regarding the B/A map for those black regions. It would be possible to truncate any negative frequency to zero, but still any conclusion regarding that region should be questioned. If possible, we recommend avoiding media with large attenuation coefficients. In the phantom with the *ex vivo* sample, the attenuation of the fatty pork was very large at room temperature, but *in vivo* fat tissue has a lower attenuation coefficient that would prevent the extreme downshifting observed.

The results from the *in vivo* scans provided good agreement of B/A with values of other mammalian species (human and bovine) if we use the cumulative averaged B/A map. On the other hand, the standard deviation of the local B/A map was almost 60% of the mean, making those statistics less useful for tissue characterization. Therefore, it is better to use cumulative values if *a priori* knowledge of uniformity of the B/A in fairly large tissues like the liver is available, as was shown in the simulations results in section 6.3.3.

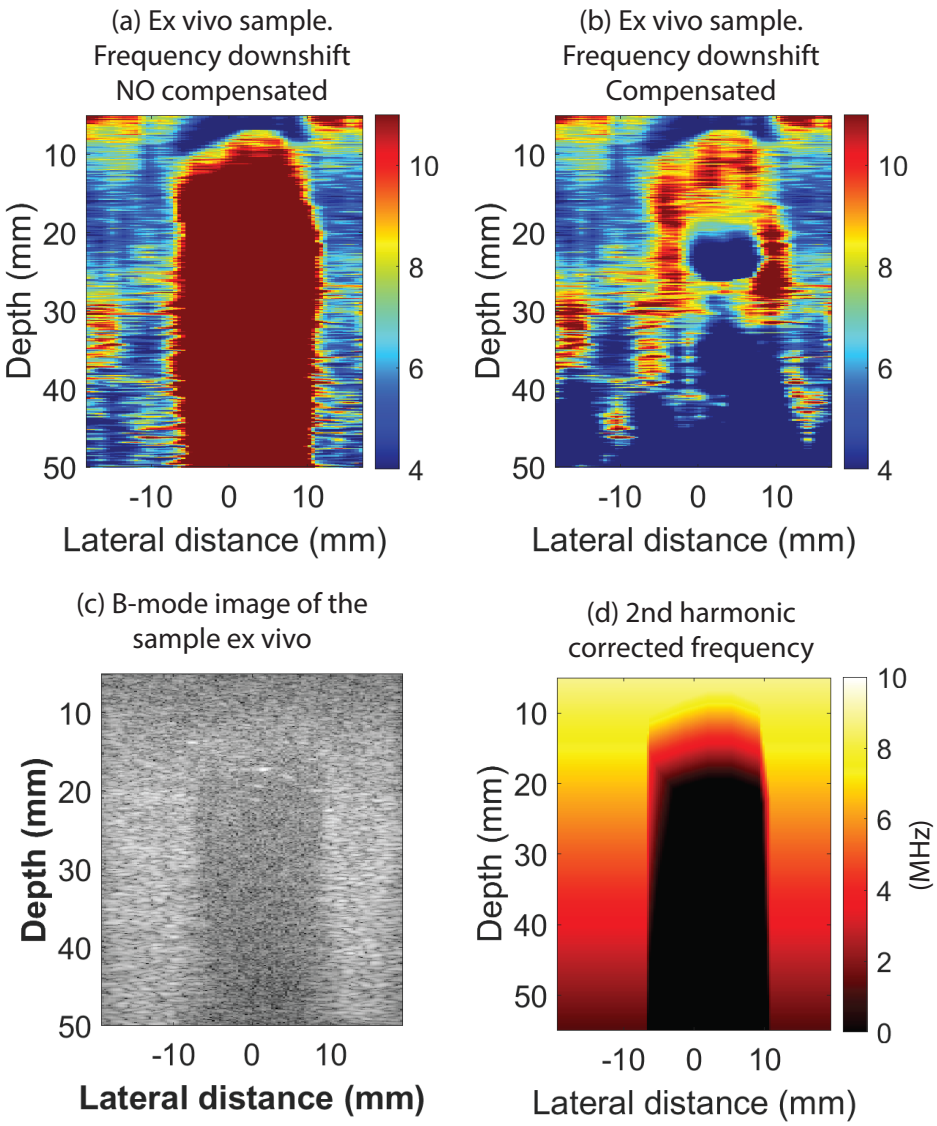

Figure 6.16: Frequency downshift compensation in the *ex vivo* sample for B/A map reconstruction. (a) Without compensation there is a clear overestimation of B/A values. (b) Including the compensation up to 22 mm depth works well. (c) The B-mode of the sample to have an idea of the location of the fatty region in the phantom. (d) Compensated frequency of the 2nd harmonic shows that midway through the fatty region, theoretically, the 2nd harmonic component downshift to negative frequencies. For our purposes, it would be convenient to exclude such area of any analysis or conclusion.

CHAPTER 7

CONCLUSIONS AND FUTURE WORK

7.1 Summary and contributions

In this dissertation, we explored connections between spectral-based quantitative ultrasound (QUS) parameters and the nonlinearity parameter, B/A. We began by quantifying adverse effects of acoustic nonlinearity on the accuracy of estimation of two prevalent spectral-based QUS parameters: the backscatter coefficient (BSC) and the attenuation coefficient (AC) in Chapters 2 and 3, respectively. From Chapter 2, we found that nonlinear distortion in the fundamental band can deteriorate the accuracy of the BSC estimates when using a calibration medium like water that has very low attenuation (planar reflector BSC method) compared to a more lossy calibration media (reference phantom method). The results also indicated that parameters derived from the BSC, e.g., the effective scatter diameter, could be inaccurate due to the effects of nonlinear distortion. These results provide important insight in that the assessed media and the media used for the calibration should have Gol'dberg ratios of close to unity to provide estimates with minimal distortion due to nonlinear propagation. For this reason, one could use the Gol'dberg number ratio between the sample and calibration medium as a potential metric to determine accuracy of the QUS estimates. This finding was also confirmed in Chapter 3 when estimating another QUS parameter, the attenuation coefficient. The use of an *in situ* calibration approach using a target embedded in the interrogated medium was presented in Chapter 4 with a theoretical Gol'dberg ratio equal to 1. The accuracy of the *in situ* calibration was expected to be less affected by nonlinear distortion and was observed to outperform even the reference phantom approach if the objective was to minimize the acoustic nonlinear distortion. However, an *in situ* calibration might not be possible in many clinical scenarios; therefore, a reference

phantom providing the Gol'dberg ratio between sample and reference close to unity would be a good alternative to obtain accurate spectral-based QUS parameters when considering the effects of acoustic nonlinear distortion.

Based on the findings in Chapters 2 and 3, an heuristic approach to estimating B/A was explored. The reasoning was the following: if mismatches in Gol'dberg numbers produced an excess attenuation when comparing QUS estimates obtained at low source pressures (quasi-linear regime) and high source pressures (nonlinear regime), measurements of excess attenuation could reveal relevant information about the quantification of the Gol'dberg ratio, and subsequently, the B/A of an unknown media could be estimated. This approach was explored in Chapter 5, where the B/A was estimated but still required calibration data from two additional reference phantoms. The accuracy of B/A estimation was reasonably good (%error<10%) for about half of the simulated sets of phantoms, when the phantoms had similar attenuation coefficient values. However, the requirement that this method use up to two reference phantoms is an obstacle to practical implementation and also the variance of spectral-based approaches for AC estimation might limit the construction of a parametric image. For these reasons, we developed an alternative B/A estimation method in the time-domain in Chapter 6.

Our time-domain approach used the conservation of energy principle to quantify implicitly the instantaneous energy of the 2nd harmonic in a nonlinear, attenuating, and scattering media. The fact that we used the envelopes of RF signals instead of deriving spectral-based parameters made it possible to map the B/A and create a parametric image of the B/A. Calibration with a reference phantom was still required but only one reference phantom instead of two reference phantoms (i.e., the method described in Chapter 5). The change in the energy of the RF signals versus depth was calculated to derive B/A estimates versus depth. The B/A parametric image was able to map uniform and nonuniform B/A media. The method provided a cumulative depth averaged value of B/A, which in simulations of realistic transducers (with elevation focusing) follow reasonably well the expected cumulative averaged B/A. A method to convert the accumulated averaged B/A and the local values of B/A was tested. However, it is important to point out that our B/A estimated maps were highly sensitive to correct values of attenuation at the fundamental and 2nd harmonic bands. *Ex vivo* experiments made this clear and also the inaccuracies that might occur if the

inclusion and background have a large mismatch of attenuation. Finally, *in vivo* results in fairly large region in healthy livers of rabbits were promising and resulted in small bias of the B/A (%error<10%).

7.2 Future work

QUS parameters have potential for tissue characterization and a rule of thumb found in this work is to choose a reference material with as close as possible Gol'dberg ratio as the unknown material. To do this, one could choose acoustic values found in literature to select a better calibration material. The *in situ* approach for calibration has the potential to compensate all the nonlinearity in the forward direction of the propagation. However, a better understanding of the *in situ* target is needed. In our case, the robustness of a 2-mm diameter spherical titanium bead was tested in terms of frequency dependence of the BSC versus increasing acoustic power levels, but the absolute values of BSCs were not computed because that required an absolute value of the bead BSC that can only be derived theoretically [44].

Regarding the heuristic approach, a unique pair of low power/high power settings were tested, but it could be helpful to try several pairs of low power/high power settings and confirm the strong correlation between Gol'dberg ratio and excess attenuation. In addition, an analysis of the minimum distances between data blocks used in AC calculation that generate enough excess attenuation would be needed because, unlike the BSC, the propagation path between proximal data block and distal data block is chosen arbitrarily in the signal processing stage.

The time-domain approach still requires additional experimental validation *in vivo*. A additional question generated by this research is to better understand how to select the instantaneous attenuation values versus depth when imaging with broadband pulses because the pulse will shift toward lower center frequencies versus depth for a broadband pulse. Considering a non-fixed AC versus depth might improve the accuracy of B/A map estimation and decrease the commonly observed overestimation of B/A toward deeper regions. The improvement observed in simulations results when adding a simple correction for center frequency of the pulse vs depth suggests that estimation of an actual center frequency is critical in the computation of at-

tenuation within our model. However, when the medium has heterogeneous attenuation, the estimation of the frequency could be too aggressive towards theoretically negative values of frequencies that make certain deeper regions of the B/A map useless. Alternative methods of instantaneous center frequency calculation might be evaluated in the future [75]. Looking towards future work in the time-domain approach, alternatives to simple moving average filters could be used to smooth the envelopes such as speckle reducing anisotropic diffusion [76]. Furthermore, the strong interaction of attenuation effects and nonlinearity effects suggests the joint estimation of attenuation coefficient and the B/A might be worth addressing in future studies. Finally, other avenues of research include the identification of a nonlinear biological systems (by Wiener Series [77]) or use of a trained neural networks that could predict nonlinear distortion of predefined signals and learn physics parameters. Both cases require an important amount of input/output training processes before fully be able to arrive to a full characterization of nonlinear acoustic media.

REFERENCES

[1] M. F. Hamilton, "Nonlinearity parameter estimation," in *Nonlinear Acoustics*, M. F. Hamilton and D. T. Blackstock, Eds. San Diego: Academic, 1998, ch. 2, pp. 163–177.

[2] A. D. Pierce, *Acoustics: An Introduction to Its Physical Principles and Applications*. Melville, NY: Acoustical Society of America, 1989.

[3] F. A. Duck, *Physical Properties of Tissues: A Comprehensive Reference Book*. London, UK: Academic Press, 1990.

[4] J. Mamou and M. L. Oelze, *Quantitative ultrasound in soft tissues*. Springer, 2013.

[5] S. K. Jeon, J. M. Lee, I. Joo, J. H. Yoon, D. H. Lee, J. Y. Lee, and J. K. Han, "Prospective evaluation of hepatic steatosis using ultrasound attenuation imaging in patients with chronic liver disease with magnetic resonance imaging proton density fat fraction as the reference standard," *Ultrasound Med. Biol.*, vol. 45, no. 6, pp. 1407–1416, 2019.

[6] H. G. Nasief, I. M. Rosado-Mendez, J. A. Zagzebski, and T. J. Hall, "A quantitative ultrasound-based multi-parameter classifier for breast masses," *Ultrasound Med. Biol.*, vol. 45, no. 7, pp. 1603–1616, 2019.

[7] F. Deeba, M. Ma, M. Pesteie, J. Terry, D. Pugash, J. A. Hutcheon, C. Mayer, S. Salcudean, and R. Rohling, "Attenuation coefficient estimation of normal placentas," *Ultrasound Med. Biol.*, vol. 45, no. 5, pp. 1081–1093, 2019.

[8] W. C. Weng, C. W. Lin, H. C. Shen, C. C. Chang, and P. H. Tsui, "Instantaneous frequency as a new approach for evaluating the clinical severity of duchenne muscular dystrophy through ultrasound imaging," *Ultrasonics*, vol. 94, pp. 235–241, 2019.

[9] R. S. C. Cobbold, *Foundations of Biomedical Ultrasound*. New York: Oxford University Press, 2007.

[10] T. L. Szabo, *Diagnostic Ultrasound Imaging: Inside Out*, 2nd ed. Boston: Academic Press, 2014.

[11] Y. Q. Jiang, C. C. Liu, R. Y. Li, W. Wang, H. Ding, Q. Qi, D. Ta, and J. D. W. Q. Wang, "Analysis of apparent integrated backscatter coefficient and backscattered spectral centroid shift in calcaneus in vivo for the ultrasonic evaluation of osteoporosis," *Ultrasound Med. Biol.*, vol. 40, no. 6, pp. 1307–1317, 2014.

[12] S. C. Lin, E. Heba, T. Wolfson, B. Ang, A. Gamst, A. Han, J. W. Erdman, W. D. O'Brien, M. P. Andre, C. B. Sirlin, and R. Loomba, "Noninvasive diagnosis of nonalcoholic fatty liver disease and quantification of liver fat using a new quantitative ultrasound technique," *Clin. Gastroenterol. Hepatol.*, vol. 13, no. 7, pp. 1337–1345, 2015.

[13] L. Sannachi, H. Tadayyon, A. Sadeghi-Naini, W. Tran, S. Gandhi, F. Wright, M. Oelze, and G. Czarnota, "Non-invasive evaluation of breast cancer response to chemotherapy using quantitative ultrasonic backscatter parameters," *Med. Image Anal.*, vol. 20, no. 1, pp. 224–236, 2015.

[14] R. J. Miller, A. Han, L. T. Gates-Tanzer, J. W. Erdman, J. L. Shisler, M. A. Wallig, and W. D. O'Brien, "Quantitative ultrasound and the pancreas: Demonstration of early detection capability," in *2017 IEEE International Ultrasonics Symposium (IUS)*, 2017, pp. 1–4.

[15] X. Chen, D. Phillips, K. Q. Schwarz, J. G. Mottley, and K. J. Parker, "The measurement of backscatter coefficient from a broadband pulse-echo system: a new formulation," *IEEE Trans. Ultrason. Ferroelectr. Freq. Control*, vol. 44, no. 2, pp. 515–525, 1997.

[16] R. Lavarello, G. Ghoshal, and M. L. Oelze, "On the estimation of backscatter coefficients using single-element focused transducers," *J. Acoust. Soc. Am.*, vol. 129, no. 5, pp. 2903–2911, 2011.

[17] L. X. Yao, J. A. Zagzebski, and E. L. Madsen, "Backscatter coefficient measurements using a reference phantom to extract depth-dependent instrumentation factors," *Ultrason. Imaging*, vol. 12, no. 1, pp. 58–70, 1990.

[18] R. T. Beyer, *Nonlinear Acoustics*. Woodbury, NY: Acoustical Society of America, 1997.

[19] E. L. Carstensen, N. D. McKay, D. Delecki, and T. G. Muir, "Absorption of finite amplitude ultrasound in tissues," *Acustica*, vol. 51, pp. 116–123, 1982.

[20] S. Goss and F. Fry, "Nonlinear acoustic behavior in focused ultrasonic fields: Observations of intensity dependent absorption in biological tissue," *IEEE Trans. on Sonics and Ultrasonics*, vol. 28, no. 1, pp. 21–25, 1981.

[21] B. Zeqiri, "Errors in attenuation measurements due to nonlinear propagation effects," *J. Acoust. Soc. Am.*, vol. 91, no. 5, pp. 2585–2593, May 1992.

[22] J. D'hooge, B. Bijnens, J. Nuyts, J.-M. Gorce, D. Friboulet, J. Thoen, F. Van de Werf, and P. Suetens, "Nonlinear propagation effects on broadband attenuation measurements and its implications for ultrasonic tissue characterization," *J. Acoust. Soc. Am.*, vol. 106, no. 2, pp. 1126–1133, July 1999.

[23] J. S. Paige, G. S. Bernstein, E. Heba, E. A. C. Costa, M. Fereirra, T. Wolfson, A. C. Gamst, M. A. Valasek, G. Y. Lin, A. Han, J. W. Erdman, W. D. O'Brien, M. P. Andre, R. Loomba, and C. B. Sirlin, "A Pilot Comparative Study of Quantitative Ultrasound, Conventional Ultrasound, and MRI for Predicting Histology-Determined Steatosis Grade in Adult Nonalcoholic Fatty Liver Disease," *Am. J. Roentgenology*, vol. 208, no. 5, pp. W168–W177, May 2017.

[24] L. R and S. A. J, "The global nafld epidemic," *Nat. Rev. Gastroenterol Hepatol.*, vol. 10, no. 11, pp. 686–690, 2013.

[25] R. L. Errabolu, C. M. Sehgal, R. C. Bahn, and J. F. Greenleaf, "Measurement of ultrasonic nonlinear parameter in excised fat tissues," *Ultrasound Med. Biol.*, vol. 14, no. 2, pp. 137–146, 1988.

[26] C. M. Sehgal, G. M. Brown, R. C. Bahn, and J. F. Greenleaf, "Measurement and use of acoustic nonlinearity and sound speed to estimate composition of excised livers," *Ultrasound Med. Biol.*, vol. 12, no. 11, pp. 865–874, Nov. 1986.

[27] M. Lokate, P. H. Peeters, L. M. Peelen, G. Haars, W. B. Veldhuis, and C. H. van Gils, "Mammographic density and breast cancer risk: the role of the fat surrounding the fibroglandular tissue," *Breast Cancer Res.*, vol. 13, no. 5, p. R103, 2011.

[28] M. F. Hamilton and D. T. Blackstock, *Nonlinear Acoustics*. San Diego: Academic Press, 1998.

[29] A. Panfilova, R. J. G. van Sloun, H. Wijkstra, O. A. Sapozhnikov, and M. Mischi, "A review on B/A measurement methods with a clinical perspective," *J. Acoust. Soc. Am.*, vol. 149, no. 4, pp. 2200–2237, Apr. 2021.

[30] X. Gong, D. Zhang, J. Liu, H. Wang, Y. Yan, and X. Xu, "Study of acoustic nonlinearity parameter imaging methods in reflection mode for biological tissues," *J. Acoust. Soc. Am.*, vol. 116, no. 3, pp. 1819–1825, 2004.

[31] R. V. Sloun, L. Demi, C. Shan, and M. Mischi, "Ultrasound coefficient of nonlinearity imaging," *IEEE Trans. Ultrason. Ferroelectr. Freq. Control*, vol. 62, no. 7, pp. 1331–1341, July 2015.

[32] C. A. Cain, "Ultrasonic reflection mode imaging of the nonlinear parameter B/A: I. A theoretical basis," *J. Acoust. Soc. Am.*, vol. 80, no. 1, pp. 28–32, 1986.

[33] J. Kvam, S. Solberg, O. F. Myhre, A. Rodriguez-Molares, and B. A. J. Angelsen, "Nonlinear bulk elasticity imaging using dual frequency ultrasound," *J. Acoust. Soc. Am.*, vol. 146, no. 4, pp. 2492–2500, 2019.

[34] M. Fatemi and J. F. Greenleaf, "Real-time assessment of the parameter of nonlinearity in tissue using 'nonlinear shadowing'," *Ultrasound Med. Biol.*, vol. 22, no. 9, pp. 1215–1228, 1996.

[35] D. Liu and M. Nikoonahad, "Pulse-echo B/A measurement using variable amplitude excitation," in *Proceedings., IEEE Ultrasonics Symposium,*, Oct. 1989, pp. 1047–1051 vol.2.

[36] L. E. Kinsler, A. R. Frey, A. B. Coppens, and J. V. Sanders, *Fundamentals of Acoustics*, 4th ed. Hoboken, NJ: John Wiley & Sons, 2000.

[37] T. D. Mast, "Empirical relationships between acoustic parameters in human soft tissues," *Acoust. Res. Lett. Online*, vol. 1, no. 2, pp. 37–42, 2000.

[38] K. A. Wear, T. A. Stiles, G. R. Frank, E. L. Madsen, F. Cheng, E. J. Feleppa, C. S. Hall, B. Kim, P. Lee, W. D. O. Jr., M. L. Oelze, B. I. Raju, K. K. Shung, T. A. Wilson, and J. R. Yuan, "Interlaboratory comparison of ultrasonic backscatter coefficient measurements from 2 to 9 MHz," *J. Ultrasound Med.*, vol. 24, no. 9, pp. 1235–1250, 2005.

[39] E. L. Madsen, G. R. Frank, and F. Dong, "Liquid or solid ultrasonically tissue-mimicking materials with very low scatter," *Ultrasound Med. Biol.*, vol. 24, no. 4, pp. 535–542, 1998.

[40] F. Dong, E. L. Madsen, M. C. MacDonald, and J. A. Zagzebski, "Nonlinearity parameter for tissue-mimicking materials," *Ultrasound Med. Biol.*, vol. 25, no. 5, pp. 831–838, 1999.

[41] Y.-S. Lee and M. F. Hamilton, "Time-domain modeling of pulsed finite-amplitude sound beams," *J. Acoust. Soc. Am.*, vol. 97, no. 2, pp. 906–917, 1995.

[42] R. O. Cleveland, M. F. Hamilton, and D. T. Blackstock, "Time-domain modeling of finite-amplitude sound in relaxing fluids," *J. Acoust. Soc. Am.*, vol. 99, no. 6, pp. 3312–3318, 1996.

[43] M. F. Insana, R. F. Wagner, D. G. Brown, and T. J. Hall, "Describing small-scale structure in random media using pulse-echo ultrasound," *J. Acoust. Soc. Am.*, vol. 87, no. 1, pp. 179–192, 1990.

[44] J. J. Faran, "Sound scattering by solid cylinders and spheres," *J. Acoust. Soc. Am.*, vol. 23, no. 4, pp. 405–418, 1951.

[45] Y. Labyed and T. A. Bigelow, "A theoretical comparison of attenuation measurement techniques from backscattered ultrasound echoes," *J. Acoust. Soc. Am.*, vol. 129, no. 4, pp. 2316–2324, 2011.

[46] A. Coila and M. L. Oelze, "Effects of acoustic nonlinearities on the ultrasonic backscatter coefficient estimation," *J. Acoust. Soc. Am.*, vol. 146, no. 1, pp. 85–94, 2019.

[47] B. E. Treeby, J. Jaros, A. P. Rendell, and B. T. Cox, "Modeling nonlinear ultrasound propagation in heterogeneous media with power law absorption using a k-space pseudospectral method," *J. Acoust. Soc. Am.*, vol. 131, no. 6, pp. 4324–4336, 2012.

[48] J. J. Anderson, M. T. Herd, M. R. King, A. Haak, Z. T. Hafez, J. Song, M. L. Oelze, E. L. Madsen, J. A. Zagzebski, J. W. D. O'Brien, and T. J. Hall, "Interlaboratory comparison of backscatter coefficient estimates for tissue-mimicking phantoms," *Ultrason. Imaging*, vol. 32, no. 1, pp. 48–64, 2010.

[49] R. Kuc and M. Schwartz, "Estimating the acoustic attenuation coefficient slope for liver from reflected ultrasound signals," *IEEE Trans. on Sonics and Ultrasonics*, vol. 26, no. 5, pp. 353–361, 1979.

[50] W. Xu and J. J. Kaufman, "Diffraction correction methods for insertion ultrasound attenuation estimation," *IEEE Trans. Biomed. Eng.*, vol. 40, no. 6, pp. 563–570, 1993.

[51] E. L. Madsen, J. A. Zagzebski, R. A. Banjavie, and R. E. Jutila, "Tissue mimicking materials for ultrasound phantoms," *Medical Physics*, vol. 5, no. 5, pp. 391–394, 1978.

[52] O. V. Bessonova, V. A. Khokhlova, M. R. Bailey, M. S. Canney, and L. A. Crum, "Focusing of high power ultrasound beams and limiting values of shock wave parameters," *Acoustical Physics*, vol. 55, no. 4, pp. 463–473, 2009.

[53] N. I. Nizam, S. R. Ara, and M. K. Hasan, "Classification of breast lesions using quantitative ultrasound biomarkers," *Biomedical Signal Processing and Control*, vol. 57, p. 101786, Mar. 2020.

[54] Y. Li, B. Li, F. Xu, C. Liu, D. Ta, and W. Wang, "Ultrasonic backscatter measurements at the calcaneus: An in vivo study," *Measurement*, vol. 122, pp. 128–134, July 2018.

[55] T. N. Nguyen, "Characterizing Fatty Liver in vivo in Rabbits, Using Quantitative Ultrasound," *Ultrasound in Medicine*, vol. 45, no. 8, p. 14, 2019.

[56] M. L. Oelze and J. Mamou, "Review of quantitative ultrasound: Envelope statistics and backscatter coefficient imaging and contributions to diagnostic ultrasound," *IEEE Trans. Ultrason. Ferroelectr. Freq. Control*, vol. 63, no. 2, pp. 336–351, 2016.

[57] A. Coila and M. L. Oelze, "Effects of acoustic nonlinearity on pulse-echo attenuation coefficient estimation from tissue-mimicking phantoms," *J. Acoust. Soc. Am.*, vol. 148, no. 2, pp. 805–814, Aug. 2020.

[58] E. L. Rosen and T. T. Vo, "Metallic Clip Deployment during Stereotactic Breast Biopsy: Retrospective Analysis," *Radiology*, Feb. 2001.

[59] M. Carmon, O. Olsha, D. Gekhtman, I. Nikitin, Y. Cohen, M. Messing, N. Lioubashevsky, R. Abu Dalo, T. Hadar, and E. Golomb, "Detectability of Hygroscopic Clips Used in Breast Cancer Surgery," *Journal of Ultrasound in Medicine*, vol. 36, no. 2, pp. 401–408, 2017.

[60] I. Thomassin-Naggara, L. Lalonde, J. David, E. Darai, S. Uzan, and I. Trop, "A plea for the biopsy marker: how, why and why not clipping after breast biopsy?" *Breast Cancer Res. Treat.*, vol. 132, no. 3, pp. 881–893, Apr. 2012.

[61] T. N. Nguyen, A. J. Tam, M. N. Do, and M. L. Oelze, "Estimation of Backscatter Coefficients Using an In Situ Calibration Source," *IEEE Trans. Ultrason. Ferroelectr. Freq. Control*, vol. 67, no. 2, pp. 308–317, Feb. 2020.

[62] A. L. Coila and R. J. Lavarello, "Regularized spectral log difference technique for ultrasonic attenuation imaging," *IEEE Trans. Ultrason. Ferroelectr. Freq. Control*, vol. 65, no. 3, pp. 378–389, 2018.

[63] I. Youn, S. H. Choi, S. H. Kook, Y. J. Choi, C. H. Park, Y. L. Park, and D. H. Kim, "Ultrasonography-Guided Surgical Clip Placement for Tumor Localization in Patients Undergoing Neoadjuvant Chemotherapy for Breast Cancer," *Journal of Breast Cancer*, vol. 18, no. 1, pp. 44–49, Mar. 2015.

[64] A. Coila, J. Rouyer, O. Zenteno, A. Luchies, M. L. Oelze, and R. Lavarello, "Total attenuation compensation for backscatter coefficient estimation using full angular spatial compounding," *Ultrasonics*, vol. 114, p. 106376, July 2021.

[65] G. Montaldo, M. Tanter, J. Bercoff, N. Benech, and M. Fink, "Coherent plane-wave compounding for very high frame rate ultrasonography and transient elastography," *IEEE Trans. Ultrason. Ferroelectr. Freq. Control*, vol. 56, no. 3, pp. 489–506, 2009.

[66] M. Bertero, P. Boccacci, and C. De Mol, *Introduction to Inverse Problems in Imaging*, 2nd ed. CRC Press, 2021.

[67] L. Niñoles, G. Clemente, S. Ventanas, and J. Benedito, "Quality assessment of Iberian pigs through backfat ultrasound characterization and fatty acid composition," *Meat Science*, vol. 76, no. 1, pp. 102–111, 2007.

[68] T. Koch, S. Lakshmanan, S. Brand, M. Wicke, K. Raum, and D. Mörlein, "Ultrasound velocity and attenuation of porcine soft tissues with respect to structure and composition: II. Skin and backfat," *Meat Science*, vol. 88, no. 1, pp. 67–74, 2011.

[69] J. C. Bamber and C. R. Hill, "Ultrasonic attenuation and propagation speed in mammalian tissues as a function of temperature," *Ultrasound Med. Biol.*, vol. 5, no. 2, pp. 149–157, 1979.

[70] S. Yongchen, D. Yanwu, and Z. Hengyuan, "Study of the Acoustic Nonlinearity Parameter in High Attenuation Biological Media," in *IEEE 1985 Ultrasonics Symposium*, Oct. 1985, pp. 891–894.

[71] D. E. Goldman and J. R. Richards, "Measurement of High-Frequency Sound Velocity in Mammalian Soft Tissues," *J. Acoust. Soc. Am.*, vol. 26, no. 6, pp. 981–983, 1954.

[72] G. Ghoshal, R. J. Lavarello, J. P. Kemmerer, R. J. Miller, and M. L. Oelze, "Ex vivo study of quantitative ultrasound parameters in fatty rabbit livers," *Ultrasound Med. Biol.*, vol. 38, no. 12, pp. 2238–2248, 2012.

[73] W. K. Law, L. A. Frizzell, and F. Dunn, "Determination of the nonlinearity parameter B/A of biological media," *Ultrasound Med. Biol.*, vol. 11, no. 2, pp. 307–318, 1985.

[74] R. Kuc, "Estimating acoustic attenuation from reflected ultrasound signals: Comparison of spectral-shift and spectral-difference approaches," *IEEE Transactions on Acoustics, Speech, and Signal Processing*, vol. 32, no. 1, pp. 1–6, Feb. 1984.

[75] A. Bovik, P. Maragos, and T. Quatieri, "AM-FM energy detection and separation in noise using multiband energy operators," *IEEE Transactions on Signal Processing*, vol. 41, no. 12, pp. 3245–3265, Dec. 1993.

[76] Y. Yu and S. Acton, "Speckle reducing anisotropic diffusion," *IEEE Transactions on Image Processing*, vol. 11, no. 11, pp. 1260–1270, 2002.

[77] M. Korenberg and I. Hunter, "The identification of nonlinear biological systems: Wiener kernel approaches," *Ann Biomed Eng*, vol. 18, p. 629–654, Dec. 1990.